UNIVERSITY OF OKLAHOMA

GRADUATE COLLEGE

Forecasting Quasi-Linear Convective Systems and Mesovortex Tornado Potential Using the Warn-on-Forecast System (WoFS)

A DISSERTATION

SUBMITTED TO THE GRADUATE FACULTY

in partial fulfillment of the requirements for the

Degree of

DOCTOR OF PHILOSOPHY

By

Kelsey Christine Britt
Norman, Oklahoma
2024

Forecasting Quasi-Linear Convective Systems and Mesovortex Tornado Potential Using the Warn-on-Forecast System (WoFS)

A DISSERTATION APPROVED FOR THE
SCHOOL OF METEOROLOGY

BY THE COMMITTEE CONSISTING OF

Dr. Cameron Homeyer, Chair
Dr. Pamela Heinselman, Co-Chair
Dr. Patrick Skinner
Dr. Marcela Loría-Salazar
Dr. Steven Cavallo
Dr. Caleb Fulton

Acknowledgments

A famous proverb states: “It takes a village to raise a child,” but I believe this sentiment is equally true for the pursuit of a Ph.D, or any advanced academic degree. Graduate school is often described as a journey that is marked by rigorous challenges, mental fatigue, and sleepless nights – all of which I have experienced first hand. However, I have been incredibly fortunate to not have to walk this path alone. Throughout this very demanding, but transformative period, I have been surrounded by a supportive community that has played an integral role in my academic and personal growth. Therefore, I would like to acknowledge some members of my village, as without them, I would not be writing this dissertation in the first place.

First and foremost, I would like to express my deepest gratitude to my advisors, Dr. Pam Heinselman and Dr. Pat Skinner. Your unwavering support and invaluable guidance have been instrumental in shaping my research and academic growth. Thank you for being patient as I fumbled my way through questions and for teaching me new ways to improve as a scientist. I thoroughly enjoyed my time working with you and learned a great deal from each of you. Grad school may be difficult, but having you two as mentors made it significantly better.

I’d also like to thank the Cooperative Institute for Severe and High-Impact Weather Research and Operations (CIWRO) and NOAA’s National Severe Storm’s Laboratory for funding my research. Funding was provided by NOAA/Office of Oceanic and Atmospheric Research under NOAA–University of Oklahoma Cooperative Agreement NA11OAR4320072, U.S. Department of Commerce, and the Warn-on-Forecast project.

I also want to acknowledge all the collaborators, mentors, and role models that I’ve met throughout this journey. First of all, thank you to each of my committee members, Dr. Cameron Homeyer, Dr. Steven Cavallo, Dr. Marcela Loría-Salazar, and Dr. Caleb Fulton for contributing your time and expertise. I appreciate your feedback and constructive criticism that have enriched my work and helped me view my research from different perspectives. Thank you to Dr. Harold Brooks for the fun and insightful conversations over the years. Not only did you make me laugh, but you also helped me become more confident in my work. Thank you to Brian Matilla, Kent Knopfmeier, Dr. Anthony Reinhart, Dr. Corey Potvin, and Dr. Monte Flora, for your collaborations, coding help, and for all the work you've done with WoFS and MRMS. I'd also like to thank Dr. Matthew Brown for his QLCS mesovortex work that heavily inspired the second part of this research. Your unwavering support and encouragement have helped my confidence grow. I look forward to working with you in the future and I cannot wait to see what we can accomplish. I also want to thank the wonderful staff at the School of Meteorology (SoM) for not only helping me with university paperwork, but also providing a safe space to express the roller coaster of emotions that come with grad school. Finally, thank you to Dr. Ryan Fogt and Dr. Jana Houser at Ohio University, where I first discovered my passion for meteorology and severe convective storms. You've both provided me with a great education and many wonderful opportunities that helped me grow as a scientist and as an individual. Thank you for always believing in me.

Next, I'd like to thank all the amazing friends I've met along this journey that have become my family. First, thank you to my 2016 SoM graduate cohort (Amanda, Andrew, Ben, Brian, Elisa, Matt, Ryann, Sarah, and Tyler) for sticking together and helping each other when it came to classes and learning how to code. Thank you to my 4650 office mates (Brian, Bobby, Claire, Francesca, and Michelle) for the fun conversations, coding help, and for being a sounding board when I needed to talk through research challenges. You all made coming into work every day fun. Also, thank you to Melanie, Bryony, Hrag, Lauren, Briana, Joel, and Ben for all the laughs through the years and for always cheering me on. This is by no means an exhaustive list, as there are so many great people that I've met since starting college. So to all my friends, thank you for being with me on this journey, offering support, empowering me, and stabilizing me when I spiral.

Lastly, I am immensely grateful to my family for their unwavering support and unconditional love. To my parents, Chris and Kathy Britt, and my brother, Connor Britt, thank you for always believing in me and encouraging me to pursue my dreams, even when those dreams resulted in me moving over 14 hours away to Oklahoma. Your sacrifices and faith in my abilities have always been my greatest source of strength and motivation. A very special thank you to my best friend and fur-baby, Beau. I adopted Beau at the end of my first semester of graduate school, so he's been by my side throughout this whole journey. I love him more than anything else in the world, and I can't imagine going on this journey without him.

The ultimate goal of the Ph.D is to become an independent scientist and researcher, but I couldn't have done it without the help of all those mentioned above. It really does take a village to get a Ph.D.

Table of Contents

List of Tables

List of Figures

Abstract

Quasi-linear convective systems (QLCSs) can produce multiple hazards (e.g., straight-line winds, flash flooding, and mesovortex tornadoes) that pose a significant threat to life and property, and are often difficult to accurately forecast. The NSSL Warn-on-Forecast System (WoFS) is a convection-allowing ensemble system developed to provide short-term, probabilistic forecasting guidance for severe convective events. Examination of WoFS's capability to predict QLCSs has yet to be systematically assessed across a large number of cases for 0–6-hr forecast times. In Part I of this study, the quality of WoFS QLCS forecasts for 50 QLCS days occurring between 2017–2020 is evaluated using object-based verification techniques. First, a storm mode identification and classification algorithm is tuned to identify high-reflectivity, linear convective structures. The algorithm is used to identify convective line objects in WoFS forecasts and Multi-Radar Multi-Sensor system (MRMS) gridded observations. WoFS QLCS objects are matched with MRMS observed objects to generate bulk verification statistics. Results suggest WoFS's QLCS forecasts are skillful with the 3- and 6-hr forecasts having similar probability of detection and false alarm ratio values near 0.59 and 0.34, respectively. The WoFS objects are larger, more intense, and less eccentric than those in MRMS. A novel centerline analysis is performed to evaluate orientation, length, and tortuosity (i.e., curvature) differences, and spatial displacements between observed and predicted convective lines. While no systematic propagation biases are found, WoFS typically has centerlines that are more tortuous and displaced to the northwest of MRMS centerlines, suggesting WoFS may be overforecasting the intensity of the QLCS's rear-inflow jet and northern bookend vortex.

One of the most challenging aspects of QLCS prediction is the ability to accurately forecast mesovortex tornado potential. The current paradigm employed by the National Weather Service for forecasting the likelihood that a QLCS will produce a mesovortex and, potentially, a tornado is known as the Three Ingredients Method (3IM). This technique's first two ingredients are grounded in RKW (Rotunno-Klemp-Weisman) Theory, which states there should be a balance between the strength of the QLCS's cold pool and the magnitude of line-normal shear to produce an optimal balanced state that favors strong, upright updrafts and enhanced low-level rotation. However, mesovortices have been observed despite sub-optimal line-normal shear within the framework of the 3IM. Additionally, observational studies examining prolific mesovortex- and tornado-producing QLCSs found a component of the low-level environmental shear field that was oriented line-parallel, which is not included in the 3IM. Recent observational and modeling work suggest line-parallel shear fosters the development of strong, cyclonic mesovortices, thus increasing the overall likelihood of QLCS tornadoes.

Motivated by these recent results, Part II of this study examines three tornadic QLCS case studies from 12 May 2022, 30 March 2022, and 15 December 2021 to investigate the potential of using the upstream kinematic environment to predict QLCS mesovortices in WoFS. Using object-based identification methods and a new technique to isolate the leading line of the WoFS QLCS objects, we are able to calculate the shear components upstream of the QLCS. Results suggest that near-storm shear components can be combined with information about the local line geometry to provide a system-relative forecast of mesovortex tornado potential in WoFS. A new composite parameter, called QTor, characterizes how favorable the environment is for the development of mesovortex tornadoes based on the magnitudes of 0–1-km line-parallel shear, 0–3-km line-normal shear, and the local tortuosity/curvature of the leading line. For each case study, the QTor forecasts are able to predict areas favorable for the development of mesovortex tornadoes that also coincide with the documented tornado reports for each case. However, small orientation differences between the WoFS and MRMS leading lines results in QTor false alarms, which will need to be accounted for and mitigated in the future. The long-term goal of this project is to revise the 3IM and bring it into a more objective framework that can then be implemented into any convection-allowing model.

Chapter 1

Introduction and Background

1.1 Quasi-Linear Convective Systems (QLCSs)

Most of the past convective storm research has focused on understanding and forecasting supercells, renowned for being prolific tornado-producing storms (Trapp et al. 2005; Markowski and Richardson 2010; Smith et al. 2012; Brotzge et al. 2013). Extensive supercell research has resulted in a refined understanding of supercell and tornado dynamics (Markowski and Richardson 2010; Davies-Jones 2015; and references therein), increased tornado warning lead time (Brotzge et al. 2013; Brooks and Correia 2018; Krocak et al. 2021), and the creation of supercell-centric composite forecasting parameters (Thompson et al. 2003, 2007, 2012). However, supercells are not the exclusive producers of tornadoes and other damaging hazards.

The quasi-linear convective system (QLCS; Trapp et al. 2005) is a sub-classification of mesoscale convective system (MCS; Houze 2018) that is linearly-oriented and has a length of at least 100 km. QLCSs are commonly referred to as squall lines, or bow echoes (Weisman 1993, 2001) when they contain bowing segments. Derechos are also classified as QLCSs (Johns and Hirt 1987). These systems are capable of producing a variety of dangerous and destructive hazards such as straight-line winds, hail, flash flooding, and tornadoes produced from shallow, embedded mesovortices (Atkins et al. 2004; Trapp et al. 2005; Smith et al. 2012; Thompson et al. 2012; Brotzge et al. 2013; Ashley et al. 2019). In fact, a QLCS climatology study analyzing composite reflectivity data, spanning from 1996–2017 in the continental United States, found QLCSs account for around 21% and 28% of tornado and severe wind reports, respectively (Ashley et al. 2019). Since these reports are fewer than those associated with supercells, QLCSs tend to not get as much attention. Consequently, our current understanding of QLCS dynamics, mesovortexgenesis processes, and the predictability of mesovortex tornado potential is limited. QLCS hazards can occur year-round, even in the cold season (October–February), when severe weather may be unexpected by the public (Trapp et al. 2005; Smith et al. 2012; Ashley et al. 2019). Furthermore, QLCSs are prone to occurring during the late-night and early-morning hours (Trapp et al. 2005; Ashley et al. 2019), posing a particular danger to the sleeping public and leading to higher fatality rates (Ashley et al. 2008). Additionally, QLCS hazards (especially severe wind and tornadoes) tend to be more difficult to warn and have shorter warning lead times compared to supercells, which presents substantial forecasting and operational challenges (Brotzge et al. 2013).

1.1.1 QLCS Structure

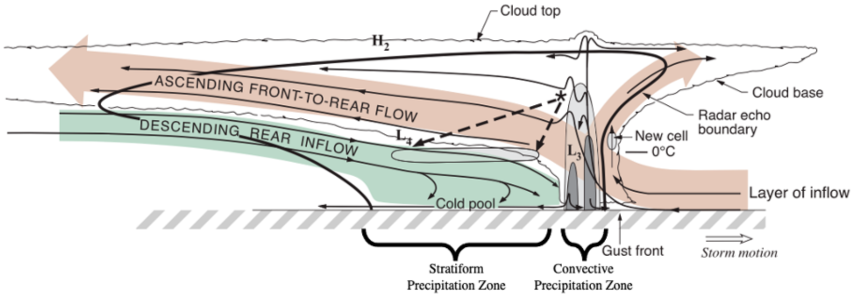

Figure 1.1: The conceptual model of the kinematic, microphysical, and radar structure for a leading-line, trailing-stratiform QLCS viewed as a vertical cross section perpendicular to the convective line (adapted from Houze (2018), their Fig. 17-12). The medium and dark gray shading represents intermediate and strong radar reflectivities. Areas of low and high pressure are denoted as L and H, respectively.

The typical structure of a leading-line, trailing-stratiform QLCS is shown in the conceptual model (Fig. 1.1) from Houze (2018). The most intense reflectivity echoes and convective towers are located along the QLCS's leading edge, with a secondary maximum in reflectivity behind the leading line known as the trailing stratiform precipitation region. The convective and trailing stratiform zones are separated by a band of less intense radar reflectivities that is often referred to as the transition zone (Biggerstaff and Houze 1993).

There are also two main flow patterns in a QLCS: the ascending front-to-rear flow and the descending rear inflow (Fig. 1.1). As the low-level inflow approaches the gust front of the QLCS, it is lifted to its level of free convection (LFC), ascends through the convective updrafts, dips slightly in the transition zone, and then gradually lifts again once it reaches the trailing stratiform zone. This flow is known as the ascending front-to-rear flow in the conceptual model (Fig. 1.1). The ascending front-to-rear flow transports rain, snow, and ice particles rearward, which then evaporate or melt as they descend behind the main line (Biggerstaff and Houze 1991; Braun and Houze 1995), resulting in the formation of the cold pool (Bryan and Parker 2010). As the QLCS matures, the cold pool will often become so strong that it overcomes the low-level shear (Rotunno et al. 1988; Weisman 1993) and results in the development of the descending rear inflow, also known as the rear-inflow jet (RIJ; Smull and Houze 1987a; Weisman 1992). The RIJ forms when the front-to-rear ascending flow transports buoyant air parcels upward and behind the leading edge of the QLCS and on top of the cold pool. This creates a horizontal buoyancy gradient that generates horizontal vorticity, resulting in the formation of opposing circulations between the unstable air aloft and the cold pool (Weisman 1992). These circulations help to accelerate midlevel air from the trailing stratiform region towards the QLCS's leading line (Weisman 1992). When the RIJ combines with the convective downdrafts near the front of the QLCS, it causes the leading line to surge forward, forming a bow echo. As the RIJ traverses through the trailing stratiform region and when it encounters convective downdrafts along the leading line, it can be pushed downward closer to the surface due to the latent cooling from melting ice or evaporating rain. This can cause strong and damaging winds at the surface (Weisman 1993; Przybylinski 1995; Evans and Doswell 2001; Wakimoto et al. 2006; Squitieri et al. 2023b).

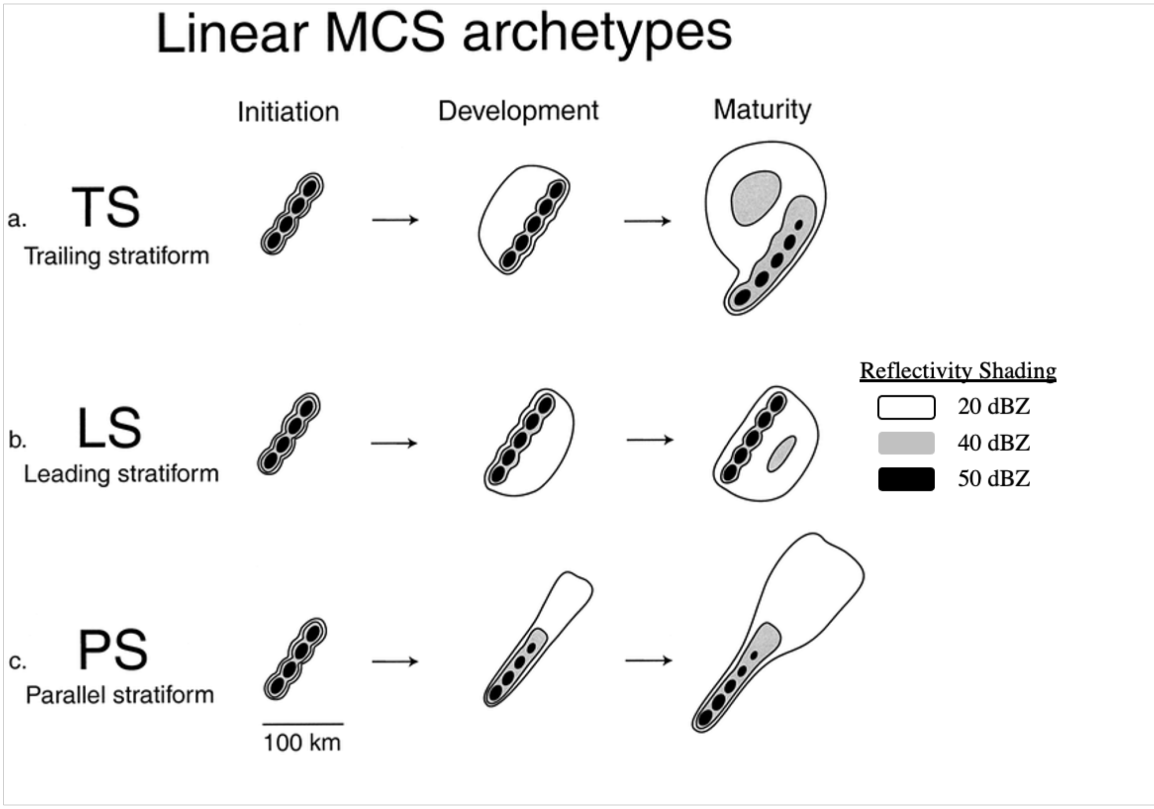

Figure 1.2: Reflectivity schematic of idealized life cycles for the three QLCS (linear MCS) archetypes: a) trailing stratiform (TS), b) leading stratiform (LS), and c) parallel stratiform (PS). The approximate time intervals between the phases for TS is 3–4 hr and 2–3 hr for LS and PS. Adapted from Parker and Johnson (2000), their Fig. 4.

While the majority (60–80%; Parker and Johnson 2000) of QLCSs are often classified as trailing stratiform archetypes (Fig. 1.2a) as described above, there are two other QLCS archetypes that can develop. The first is known as a leading stratiform (Fig. 1.2b) QLCS where the stratiform precipitation zone is in front of the convective line. This type of QLCS often forms in environments that have a deep layer of shear that has a strong rear-to-front component, which advects hydrometeors ahead of the convective line. The other archetype is known as a parallel-stratiform QLCS (Fig. 1.2c). These often occur in environments where there is a deep layer of shear with a strong line-parallel component. In this case, hydrometeors are deposited parallel to the orientation of the convective updrafts. It's estimated that only 10–20% of QLCSs are of the leading stratiform or parallel stratiform variety (Parker and Johnson 2000).

1.1.2 QLCS Maintenance and RKW Theory

One of the most debated theories related to QLCS maintenance is from a study by Richard Rotunno, Joseph Klemp, and Morris Weisman that is referred to as RKW theory (Rotunno et al. 1988). RKW theory suggests that to maintain a long-lived QLCS, there needs to be a balance between the environmental 0–3-km vertical wind shear perpendicular to the line (also known as the line-normal shear component) and the horizontal vorticity that is generated by the buoyancy gradient across the cold pool and gust front (Fig. 1.3). This balance is known as the "optimal condition" for QLCS longevity, as it produces deeper lifting and the largest potential for triggering new cell growth along the gust front. If the cold pool is weak or nonexistent, the environmental shear will dominate and cause the updraft to tilt downshear (Fig. 1.3c). On the other hand, when the strength of the cold pool exceeds the environmental shear, the updrafts tilt upshear or over the cold pool (Fig. 1.3b). When the environmental wind shear and the strength of the cold pool are balanced, updrafts tend to be upright (Fig. 1.3d). RKW theory assumes that QLCSs with upright updrafts will

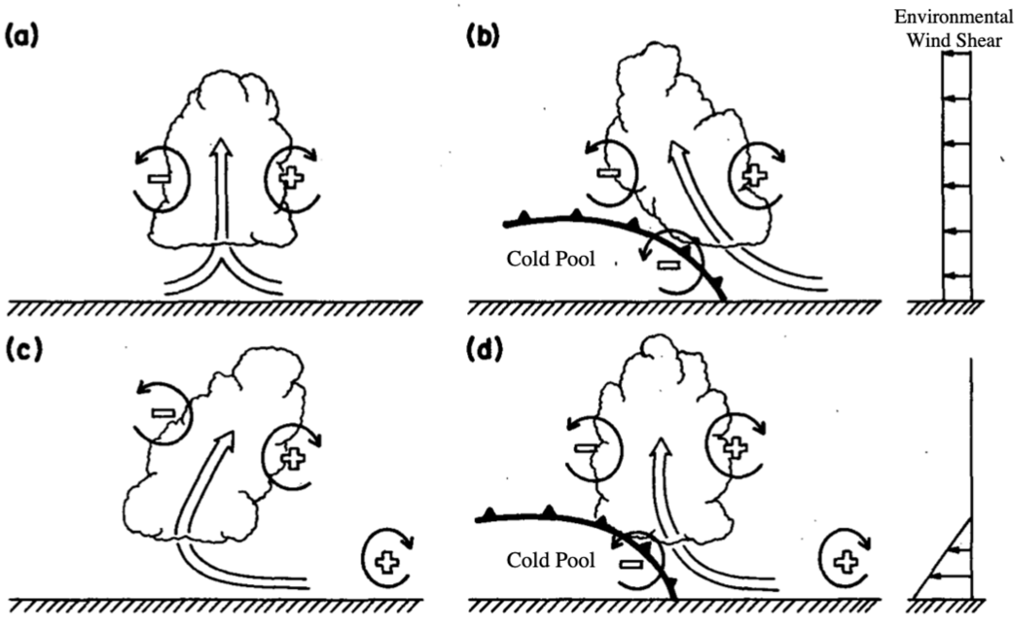

Figure 1.3: Schematic showing how an updraft may be influenced by a cold pool and/or environmental wind shear. a) Without environmental shear or a cold pool, the axis of the updraft produced by the thermally created, symmetric vorticity distribution is vertical. b) With only a cold pool, the negative vorticity underlying the cold pool causes the updraft to lean upshear or over the cold pool. c) With only environmental shear, the updraft is tilted downshear. d) With a cold pool and environmental shear, the two vorticity sources balance each other resulting in an upright updraft. Cyclonic and anticyclonic vorticity are denoted as positive and negative, respectively. Adapted from Rotunno et al. (1988), their Fig. 18.

be longer-lived than those with tilted updrafts, as upright updrafts are stronger than those that are tilted.

While RKW theory did improve our understanding of cold-pool–shear interactions at the time, it is a highly idealized model of QLCS evolution that tends to break down in the real world (Evans and Doswell 2001; Coniglio and Stensrud 2001; Weisman and Rotunno 2004; Coniglio et al. 2012). First of all, a climatology study (Evans and Doswell 2001) analyzing derecho environments found these events could occur even when the magnitude of low-level vertical shear was below the suggested RKW theory threshold of 20 ms^{-1} (Rotunno et al. 1988). Additionally, many severe QLCSs have been observed with upshear tilt, and the development of this tilt is often important for the development of bow echoes. The intensification and deepening of the cold pool is part of the natural evolution of a QLCS. Therefore, a mature QLCS may be classified as "sub-optimal" as the cold pool dominates the environmental shear and the updrafts tilt upshear over the cold pool. This rearward-tilting updraft can induce a midlevel pressure minimum over the cold pool, which accelerates air into the QLCS from the rear and that air impinges on the convective line from behind (Coniglio et al. 2012). These systems are still considered strong and dangerous as they often produce severe winds at the surface.

Some uncertainty also exists as to the appropriate depth to calculate wind shear and how to apply RKW theory to cold pools that are deeper than those studied in Rotunno et al. (1988). RKW theory only evaluates the wind shear over the depth of the cold pool (2–3 km above ground level; Rotunno et al. 1988). However, Weisman and Rotunno (2004) applied RKW theory in three dimensions and found it was important to consider vertical shear over a deeper layer (over the lowest 5 km) than the cold pool itself. Coniglio et al. (2012) also suggests that deeper shear should be given more weight than the 0–3-km shear when applying RKW theory, as they found the interaction between the cold pool and the shear in the lowest 3 km was not a primary factor in the structure, strength, and longevity of the system they analyzed. Overall, QLCSs are often more complicated than the idealized

RKW theory suggests. Therefore, it is important to consider other factors (e.g., depth of cold pool, kinematic and thermodynamic conditions, forcing mechanisms, etc.) when attempting to forecast these systems (Coniglio et al. 2012).

1.1.3 QLCS Mesovortices

Possibly one of the most challenging aspects of QLCS prediction is the ability to accurately forecast mesovortex tornado potential. Mesovortices are meso-γ-scale (2–40 km; Weisman and Trapp 2003a) circulations that typically form near the surface (1–2 km above ground) along the leading edge of a QLCS. They are typically the most intense near the surface, but can extend up to 3 km above ground level (AGL; Flournoy and Coniglio 2019). High-resolution radar studies have observed the rapid formation of mesovortices within minutes (Mahale et al. 2012; Newman and Heinselman 2012). These rapidly-developing mesovortices have long been associated with severe straight-line wind events (Atkins et al. 2004, 2005; Wakimoto et al. 2006; Wheatley et al. 2006; Mahale et al. 2012; Newman and Heinselman 2012) and tornadoes (Atkins et al. 2004, 2005; Flournoy and Coniglio 2019; McDonald and Weiss 2021; Marion and Trapp 2021; Brown et al. 2024). While some mesovortices are short-lived, stronger vortices may persist up to an hour. Mesovortices are typically difficult to observe with operational WSR-88D radars because of radar sampling limitations, the speed at which mesovortices develop, their shallow depth, and the range from the radar. For example, mesovortices can form in a matter of minutes, and depending on the temporal resolution of the radar they could be missed. Also, the greater the distance between the QLCS and the radar, the higher in the storm the radar beam will be scanning and may miss shallow mesovortices. Therefore, QLCS tornadoes often have lower probability of detection (POD) and a higher tendency to be warned at negative lead times compared to supercell tornadoes (Brotzge et al. 2013). Consequently, forecasting mesovortices and their tornado potential presents substantial challenges in operational meteorology.

Other than tornadoes, mesovortices may also be associated with severe straight-line winds at the surface. The initial hypothesis for damaging straight-line winds at the surface was that they were caused by a descending RIJ when it combined with QLCS's outflow (Smull and Houze 1987a; Weisman 1993; Przybylinski 1995). However, Forbes and Wakimoto (1983) noticed small-scale swaths of extreme and concentrated destruction embedded within the large-scale regions of damage that were too small-scale to be attributed to a descending RIJ, further supported by damage surveys presented by Fujita (1981), Fujita and Wakimoto (1981), and Funk et al. (1999). Idealized simulations performed by Weisman and Trapp (2003b) and Trapp and Weisman (2003) hypothesized that severe straight-line winds were generated when the RIJ and storm motion were superimposed and aligned with the cyclonic rotation associated with embedded mesovortices along the QLCS's convective line. Afterwards, many studies sought to explore the mechanisms for mesovortexgenesis in QLCSs to better understand mesovortices and the damage they produce.

1.1.3.1 Mechanisms for Mesovortexgenesis

Idealized simulations from Weisman and Trapp (2003b) and Trapp and Weisman (2003) found QLCS mesovortices readily develop when the environment contains vertical wind shear of 20 ms^{-1} or greater in the lowest 5 km AGL. This result is consistent with RKW theory (Rotunno et al. 1988), which describes how the strongest updrafts in QLCSs tend to develop when there is sufficient low-level environmental vertical wind shear that balances the strength of the QLCS's cold pool. In this balanced state, updrafts that are deeper, stronger, and more upright tend to develop. These stronger updrafts are associated with increased vertical vorticity stretching leading to the intensification of mesovortices.

The strongest mesovortices typically form when the developing QLCS acquires bowing segments in its convective line. These segments typically form when the RIJ descends towards the convective line, where it combines with the storm's outflow and causes the gust front to accelerate outwards. Horizontal baroclinic vorticity (i.e., vorticity generated

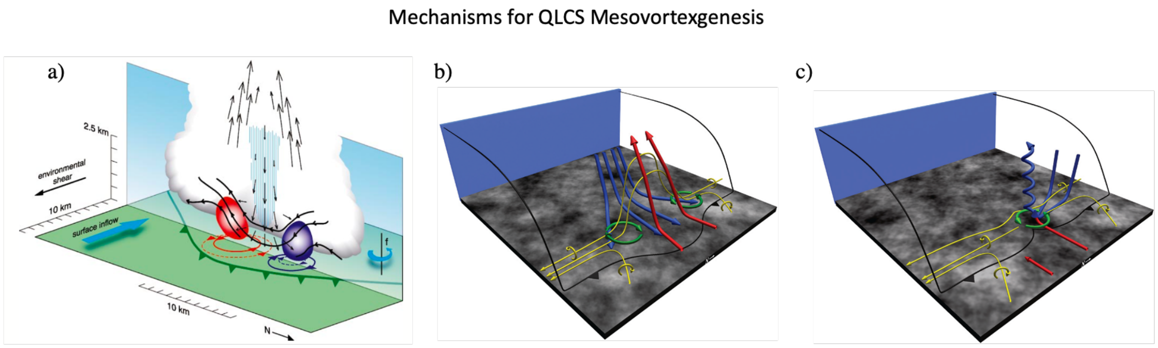

Figure 1.4: Three of the potential mechanisms for mesovortexgenesis. a) Schematic shows the formation of a vorticity couplet (red for cyclonic and purple for anticyclonic) resulting from the tilting of baroclinic horizontal vorticity by a downdraft. Green line represents the gust front, vectors are for vertical air motion, blue hatching represents the rain core, and the bold black lines are vertical vortex lines. The future state of the vorticity couplet, resulting from the stretching of planetary vorticity, is represented by the dashed red and purple lines (Trapp and Weisman 2003, their Fig 23). b) Formation of cyclonic and anticyclonic mesovortices (green arrows) from the tilting of an updraft (red; also depicts inflow). Vortex lines are indicated in gold, downdraft in blue, and the gust front location in black (Atkins and Laurent 2009b, their Fig. 16). c) Same as in b), but for cyclonic-only mesovortexgenesis (Atkins and Laurent 2009b, their Fig. 15.)

from density or temperature gradients) is generated along the gust front interface and then tilted by one (or more) of the mesovortexgensis mechanisms, resulting in mesovortex formation. Collectively, there are four proposed mechanisms seeking to explain the genesis of mesovortices. The first three types (Fig.1.4) are related to how the generation of horizontal baroclinic vorticity enhances near-surface vertical vorticity (Trapp and Weisman 2003; Atkins and Laurent 2009b; Flournoy and Coniglio 2019). In contrast, the last method hypothesizes horizontal shearing instability (HSI) is responsible for the formation of mesovortices (Wheatley and Trapp 2008; Conrad and Knupp 2019). For simplicity, these methods will be referred to as the Downdraft, Updraft, Supercell, and HSI mechanisms, respectively.

Downdraft Mechanism: The Trapp and Weisman (2003) study explains the first proposed mechanism for QLCS mesovortexgenesis (Fig. 1.4a). Their results show mesovortexgenesis is initiated in the low levels by the downward tilting of crosswise baroclinic horizontal vorticity, which is generated along the outflow boundary by precipitating downdrafts. The downdraft tilts vortex lines downward into a "U" shape that results in the formation of a low-level vorticity couplet centered around the downdraft (Fig. 1.4a). As ambient planetary vorticity is stretched vertically, the cyclonic part of the vorticity couplet is favored over the anticyclonic portion, leading to the intensification of the cyclonic vortex. This proposed mesovortexgenesis mechanism was also confirmed in later studies (Wheatley et al. 2006; Wakimoto et al. 2006; Wheatley and Trapp 2008; Parker et al. 2020; McDonald and Weiss 2021). However, one observational study (Wakimoto et al. 2006) saw a similar process, except they noted the downdraft was driven mechanically by nearby updrafts and not by precipitation loading as in Trapp and Weisman (2003).

Updraft Mechanism: In contrast to the first method, the second mechanism states an updraft is responsible for tilting horizontal baroclinic vorticity into the vertical (Fig. 1.4b; Atkins and Laurent 2009b). The updraft is produced when a convective-scale downdraft accelerates the QLCS's gust front outward, thereby, enhancing convergence along the boundary's interface. Vortex lines are tilted upwards by an updraft forming an arch of vortex lines shaped like an upside-down "U", resulting in the formation of a vorticity couplet around the updraft (Fig. 1.4b; Atkins and Laurent 2009b; Schenkman et al. 2012).

Supercell Mechanism: The third mesovortexgenesis process was proposed by Atkins and Laurent (2009b) and resembles the formation of low-level mesocyclones within supercells (Fig. 1.4c; Markowski and Richardson 2009). In this case, parcels first acquire horizontal vorticity by descending in a downdraft, then they are tilted and stretched by an updraft located along the QLCS's gust front. In this mechanism, environmental horizontal vorticity is predominately streamwise, or parallel to the storm-relative flow. This mechanism is also observed in a few other studies (e.g., Atkins et al. 2004, 2005; Flournoy and Coniglio 2019). However, in the Flournoy and Coniglio (2019) study, they noted the environmental parcels gained cyclonic vertical vorticity through the upward tilting of predominately crosswise horizontal vorticity. While the previous mechanisms produce a vorticity couplet, this method (Flournoy and Coniglio 2019) has the updraft collocated with the vertical vorticity maximum, thus producing a single cyclonically-rotating updraft.

HSI Mechanism: Lastly, mesovortexgenesis can occur through the release of horizontal shear instability (HSI; Conrad and Knupp 2019), which is similar to the mechanism for nonsupercell tornadoes (Lee and Wilhelmson 1997a,b). By analyzing dual-Doppler radar observations of two QLCS events, Conrad and Knupp (2019) found the lack of any vorticity couplet, density current, surging segment, or a strong RIJ. This led them to believe that the previous mechanisms for mesovortexgenesis, as mentioned above, were not applicable. The lack of a strong density current also implied that the generation of baroclinic horizontal vorticity along the QLCS's leading edge was not necessary for the formation of the mesovortices they observed. Instead, Conrad and Knupp (2019) hypothesized that HSI may be responsible for mesovortexgenesis, especially in QLCSs that develop in high-shear, low-CAPE (convective available potential energy) environments because the horizontal shear in these cases is typically parallel to the leading edge of the QLCS. Another study, Wheatley and Trapp (2008), found similar results with their cold-season QLCS case where the vertical vorticity needed for the HSI mechanism originated from the upward tilting of environmental horizontal vorticity.

Knowing which of the mechanisms will contribute to mesovortexgenesis in any given QLCS case is still not fully understood. This uncertainty makes forecasting QLCS mesovortices and their corresponding hazards even more difficult. Additionally, the studies mentioned above have also observed secondary sources of vorticity that could contribute to mesovortexgenesis. These sources include low-level surface drag or friction (Schenkman et al. 2012; Xu et al. 2015; Parker et al. 2020; Tochimoto and Niino 2022), kinematic effects related to a descending RIJ (Trapp and Weisman 2003; Atkins and Laurent 2009b; Xu et al. 2015; Flournoy and Coniglio 2019), cold pool characteristics (McDonald and Weiss 2021; Marion and Trapp 2021), and ambient horizontal vorticity (Wheatley and Trapp 2008; Flournoy and Coniglio 2019). To complicate things further, some simulations (Atkins and Laurent 2009b; Parker et al. 2020) found the existence of more than one mesovortexgenesis mechanism in the same QLCS. Therefore, multiple mechanisms may be responsible for generating mesovortices in the same storm, but they could also counteract each other. Therefore, more high-resolution observations and numerical simulations are required to understand why some genesis mechanisms are favored over others, the environmental conditions that lead to each mechanism, influence of genesis mechanism on mesovortex characteristics (e.g., intensity, depth, longevity, etc.), and how this new information may affect our ability to forecast mesovortices and the hazards they produce.

1.1.3.2 The 3-Ingredients Method

Supercell-centric composite forecast parameters, such as the Supercell Composite Parameter (SCP; Thompson et al. 2003, 2007) and the Significant Tornado Parameter (STP; Thompson et al. 2003, 2012), are used extensively by the National Weather Service (NWS) and Storm Prediction Center (SPC) to assess tornado potential associated with supercells. An equivalent forecasting parameter for QLCSs, however, is yet to be developed. The current paradigm employed by the NWS for forecasting the likelihood that a QLCS will produce a mesovortex and tornado is known as the Three Ingredients Method (3IM; Schaumann and Przybylinksi 2012; Gibbs 2021). The ingredients are as follows:

1. Ambient low-level ($\leq$ 1 km AGL) shear and system cold pool that are nearly balanced or slightly shear-dominant, which is indicative of upright updrafts.
2. 0–3-km line-normal shear magnitude $\geq$ 15 m s^{-1}.
3. The presence of a RIJ or enhanced outflow that causes a surge or bow in the QLCS.

The first and second ingredients of this framework are grounded in RKW theory (Rotunno et al. 1988). When the horizontal vorticity from environmental shear is balanced with the vorticity generated by the cold pool, the updrafts remain upright and strong, which maximizes the lifting of environmental air along the outflow boundary. Upright updrafts also facilitate the stretching of near-surface vertical vorticity that is important to mesovortexgenesis (Atkins and Laurent 2009a,b). The final ingredient is the presence of a bowing segment along the leading line of the QLCS that is often associated with surging outflow or the development and intensification of the RIJ.

While the 3IM assumes that factors favoring a balanced system should also promote mesovortexgenesis, this is not always the case, leading to inherent problems with this technique. First, mesovortices have been observed despite the line-normal shear magnitude being below the 3IM threshold (Ungar and Coniglio 2023). Additionally, observational studies examining prolific mesovortex- and tornado-producing QLCSs typically had a component of the low-level environmental shear field that was oriented line-parallel (Funk et al. 1999; Lyza et al. 2017; Flournoy and Coniglio 2019). A recent study by Brown et al. (2024) found that having more line-parallel shear favors larger, stronger, and more persistent mesovortices than environments with less line-parallel shear. They also identified a

Table 1.1: The 10 confidence builders and 4 nudgers included in the 3IM. The confidence builders carry more weight than the nudgers (Schaumann and Przybylinksi 2012; Gibbs 2021).

10 Confidence Builders
Descending RIJ or reflectivity drop
Enhancing bow/surge
Line break
Paired front/rear inflow notch
Updraft-Downdraft Convergence Zone (UDCZ) entry point
Front reflectivity nub
Boundary ingestion
Contracting bookend vortex with $V_r \geq 25$ kt
Tight/strong Mesovortex with $V_r \geq 25$ kt
Confirmed tornado or tornado debris signature (TDS)
4 Nudgers
Reflectivity tag intersecting a surge
0–3-km MLCAPE ≥ 40 J/kg
Cell merger or reflectivity spike near surge
History of tornadoes (includes any prior TDSs)

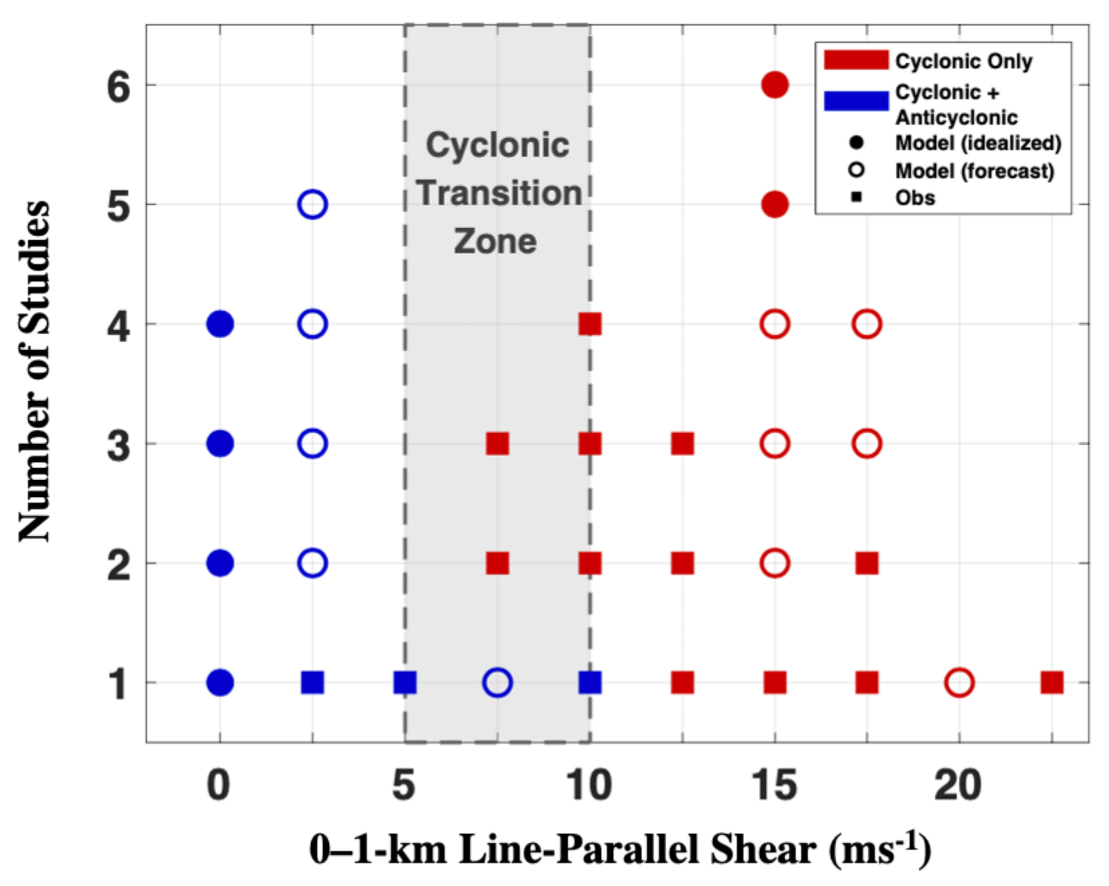

Figure 1.5: Results from the mesovortex meta-analysis study performed by Brown et al. (2024). Red markers denote studies with strong, predominately cyclonic mesovortices and blue markers denote studies with a combination of strong cyclonic and anti-cyclonic mesovortices. The marker shape represents the study type of idealized simulations/models (filled circles), forecast models (unfilled circles), or observations (filled squares). The gray shaded area represents the line-parallel shear transition zone, in which mesovortices become predominately cyclonic.

critical threshold of 0–1-km line-parallel shear between 7–10 ms^{-1} where QLCSs produce a higher proportion of cyclonic mesovortices (Fig. 1.5; Brown et al. 2024). Atkins et al. (2004) found that tornadic mesovortices tended to be stronger, larger, and more persistent than nontornadic mesovortices. Thus, an environment with more line-parallel shear may also increase the likelihood for mesovortex tornadoes. Therefore, the 3IM's exclusive focus on line-normal shear is problematic.

Another weakness of the 3IM is that it is a subjective and manual process that cannot be implemented into NWP model guidance, limiting its ability to provide timely predictions for mesovortex likelihood. Assessing the 3IM is also a time-consuming process due to the inclusion of ten additional confidence builders and four nudgers aimed at bolstering a forecaster's confidence in issuing a tornado warning for a QLCS (Table 1.1). Since mesovortices can develop quickly, time is valuable. Additionally, repeatedly augmenting the 3IM with more confidence builders and nudgers to account for contradicting observations leads to unnecessary complexity. Furthermore, another limitation of the 3IM is that it relies heavily on the availability of radar data and radar coverage. Almost all of the ingredients and confidence builders are meant to be assessed using radar reflectivities and radial velocities. Therefore, sparse radar coverage, erroneous data, and the distance between the storm and the radar can all impact the 3IM's usability. Nevertheless, development of high-resolution, convection-allowing NWP models provides an opportunity to transform the subjective nature of the 3IM into an objective framework, creating a simpler and potentially more effective approach for predicting QLCS tornado likelihood.

1.2 The Warn-on-Forecast Project

In 2009, Stensrud et al. (2009) envisioned a future in which NWS warnings transitioned from a warn-on-detection to a warn-on-forecast paradigm. To work towards this goal, Stensrud et al. (2009) suggested the need for a rapidly-updating, probabilistic convective-scale ensemble prediction system that can assimilate real-time observations. Consequently, the

National Oceanic and Atmospheric Administration's (NOAA) National Severe Storms Laboratory (NSSL) and their partners began working on the warn-on-forecast project (WoF; Stensrud et al. 2009, 2013; Heinselman et al. 2024). Since NWP capabilities were very limited in 2009, Stensrud et al. (2009) outlined some of the technical, scientific, and sociological challenges that would need research and development to bring their vision into reality. Some of the challenges included researching and developing a high-resolution convection-allowing ensemble, variational- and ensemble-based data assimilation techniques, multi-moment microphysics parameterizations, post-processing and verification techniques, and optimizing visualization for probabilistic forecast products (Heinselman et al. 2024). The research and development to address these challenges culminated into the Warn-on-Forecast System (Heinselman et al. 2024), and an experimental WoFS has been run for severe weather events in real-time since 2017.

1.2.1 The Warn-on-Forecast System

WoFS was created to provide probabilistic guidance for severe convective events between the space and time scales of typical convective watches and warnings. WoFS is a 36-member ensemble data assimilation and prediction system. From 2017–2019, WoFS was initialized using the High-Resolution Rapid Refresh Ensemble (HRRRE; Dowell et al. 2016) run by NOAA/Earth System Research Laboratory (ESRL). After 2019, the High-Resolution Rapid Refresh Data Assimilation System (HRRRDAS; Dowell et al. 2022) was used to initialize WoFS. Until 2021, the lateral boundary conditions for the 750 km x 750 km (2017–2018) or the 900 km x 900 km (2019–present) WoFS domain were generated from the experimental HRRR ensemble. After 2021, the lateral boundary conditions were provided by the 12 UTC operational HRRR forecast, which were perturbed using the first 18 members of the Global Ensemble Prediction System (GEFS; Zhou and Coauthors 2022). The location of the domain varies from day to day, but is often based on the SPC's Day 1

Convective Outlook. The domain is then placed over the region that is expected to be the most favorable for the development of severe convection.

WoFS uses 3-km horizontal grid spacing and has 51 vertical levels that extend from the surface to 10 hPa. WoFS is cycled every 15 min and uses an Ensemble Kalman filter (EnKF; Houtekamer and Zhang 2016) to assimilate MRMS reflectivity (Smith et al. 2016), Weather Surveillance Radar-1988 Doppler (WSR-88D) radial velocity, Geostationary Operational Environmental Satellite (GOES) cloud water path retrievals (Jones et al. 2015, 2016, 2020), GOES clear sky radiances (Jones et al. 2018), and any available conventional observations from a variety of observing systems (e.g., Automated Surface Observing Systems, mesonets). For the 2017–2018 configuration, WoFS used a DART-based (Data Assimilation Research Testbed; Anderson and Collins 2007; Anderson et al. 2009) EnKF, but switched to the Community Gridpoint Statistical Interpolation (GSI; Kleist et al. 2009; Hu et al. 2016) EnKF starting in 2019.

Each WoFS ensemble member utilizes the NSSL two-moment microphysics scheme (Mansell et al. 2010) and the Rapid Update Cycle (RUC) land surface model (Smirnova et al. 2016). However, the planetary boundary layer (PBL) and radiation physics parameterizations are varied among forecast members to account for uncertainties in the model physics (see Table 1 in Skinner et al. 2018). WoFS issues 18-member forecasts that are initialized at the top-of-the-hour and the bottom-of-the-hour that extend to 6- and 3-hr lead times. However, for this study, only the forecasts initialized at the top of the hour are used. For the full history and evolution of WoFS, please refer to Heinselman et al. (2024).

1.2.2 WoFS QLCS Prediction

WoFS has demonstrated an ability to provide skillful forecasts for a variety of hazardous weather events such as tornadic thunderstorms (Yussouf et al. 2013; Wheatley et al. 2015; Yussouf et al. 2015; Jones et al. 2016; Skinner et al. 2018; Flora et al. 2019; Britt et al. 2020), flash flooding events (Yussouf et al. 2016; Lawson et al. 2018; Yussouf and Knopfmeier

2019; Yussouf et al. 2020b), and tropical cyclones (Jones et al. 2019; Yussouf et al. 2020a). However, WoFS studies analyzing QLCSs are limited. Wheatley et al. (2015) included a QLCS case as part of their storm-scale radar, data assimilation experiments using WoFS. More recently, Kerr and Alsheimer (2022) analyzed WoFS's storm-scale predictability of a QLCS event responsible for a tornado outbreak on 13 April 2020. They found WoFS's retrospective overnight forecasts for this event would have been beneficial for increasing the lead time of warnings (Kerr and Alsheimer 2022). However, the capability of WoFS to accurately forecast QLCSs has not been systematically analyzed.

1.3 Motivation and Research Questions

QLCSs are complex convective systems that can take on many shapes (Parker and Johnson 2000), and can form in a variety of different environments (cold-season and warm-season; Trapp et al. 2005; Ashley et al. 2019). They can also produce mesovortices, which can, in turn, produce tornadoes and/or severe straight-line winds that cause extensive damage to the surrounding areas and communities. Mesovortices pose a complex forecasting challenge as they can develop by multiple mechanisms (reviewed in Section 1.1.3.1), and in different environments. Additionally, they are small-scale circulations that cannot be fully resolved by most forecasting models, so forecasters have to rely heavily on radar data to assess the 3IM used to forecast the potential that a mesovortex may produce a tornado.

However, the creation and development of WoFS provides an opportunity to explore the forecasting capabilities and performance for QLCSs and the mesovortices they produce. The system can even be used to analyze the environments surrounding the mesovortices to further understand the conditions under which they form and how that might inform the ways we forecast them. WoFS has already demonstrated skill in forecasting severe convective events, but no studies have assessed the performance of WoFS's QLCS forecasts. Therefore, the purpose and main objective of Part I of this study is to evaluate WoFS's capability to predict QLCS spatial extent, timing, and location at 0–6-hr lead times. For the first objective, we examine the WoFS forecasts from 50 QLCS days spanning from 2017–2020 to determine WoFS's QLCS forecast performance using object-based verification techniques to answer the following research questions:

1. How well do the 0–6-hr WoFS QLCS forecasts perform?
2. What are some of the differences in characteristics (e.g., size, shape, intensity) between forecasted and observed QLCSs?
3. Since typical object-based methods measure more large-scale differences, how can we measure more specific differences between forecasted and observed QLCS convective lines (e.g., line curvature, orientation, and location/displacement)?

To assess WoFS's skill in the prediction of QLCS events, object-based verification techniques are applied (e.g., Davis et al. 2006a,b). These verification methods have been used extensively within the WoFS framework (e.g., Skinner et al. 2018; Flora et al. 2019; Britt et al. 2020; Potvin et al. 2020; Laser et al. 2022; Miller et al. 2022; Guerra et al. 2022) to match thunderstorm objects forecasted by WoFS with observed objects in the gridded NEXRAD data from the Multi-Radar Multi-Sensor system (MRMS; Smith et al. 2016). For Part I of this study, QLCS objects are identified using an object identification and classification algorithm (Potvin et al. 2022), and then are matched and verified using methods adapted from Skinner et al. (2018). Object-based verification metrics are then used to evaluate the overall performance of WoFS's 6-hr QLCS forecasts. Furthermore, a novel centerline analysis is used to explore more specific errors between forecasted and observed QLCS objects (i.e., orientation, spatial displacement, and tortuosity/curvature), that are not considered in simple object matching. Those errors can then be connected to physical processes occurring within the QLCSs, which may help determine how WoFS may be representing these processes. Moreover, the centerline analysis may provide insight into the advantages and disadvantages of using WoFS to forecast QLCSs, and determine components of the forecast system that may need to be changed or improved in the future.

The objective and associated research questions for Part I of this study will be addressed in Chapter 2 of this dissertation, which has been published as an article in *Weather and Forecasting* (Britt et al. 2024).

Part I of this study will act as the foundation for Part II, which will explore the potential for creating a more effective method for predicting QLCS tornado likelihood that can be implemented into NWP models. Part II of this study will act as a proof-of-concept study, in which the main objective is to investigate the potential of using the upstream shear environment to predict QLCS mesovortex tornado potential using WoFS. To address this objective, we seek to answer the following research questions:

1. Can line-parallel and line-normal shear upstream of a QLCS's leading line be used to provide forecast guidance for mesovortex tornado potential?

2. What other leading line characteristics can be used to forecast mesovortex tornado potential?

3. How can the subjective framework of the 3IM be transformed into an objective framework that can be integrated into convection-allowing modeling systems?

To answer these research questions, a new analysis technique is created that isolates the QLCS's leading line and calculates the line-parallel and line-normal shear relative to the orientation of the leading line. We also introduce a new composite parameter that uses the product of 0–1-km line-parallel shear (recommended from the recent work by Brown et al. 2024), 0–3-km line-normal shear (from the 3IM), and the local curvature of the leading line to highlight areas favorable for mesovortex tornadoes to develop. This parameter is tested on three QLCS case studies that differ in seasonality, time of day, location, and environment to gauge the performance of the parameter and the changes that will need to be made in the future.

The second main objective and associated research questions will be explored in Chapter 3. Finally, Chapter 4 will provide the main conclusions, as well as a discussion about future work.

Chapter 2

Verification of QLCS Events in WoFS

2.1 Data and Methods

2.1.1 WoFS and MRMS Datasets

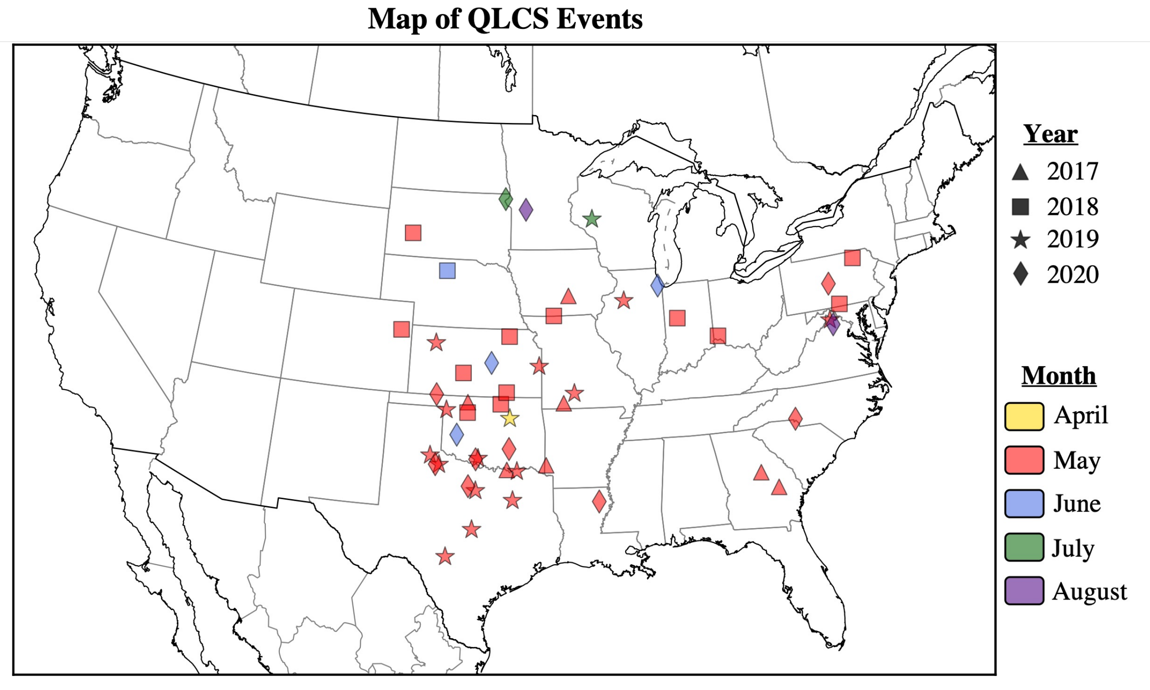

Figure 2.1: Geographic and monthly distribution of the selected QLCS events. The symbols and colors represent the year and month of QLCS occurrence, respectively. Each point represents the center of the WoFS domain for each event.

The WoFS forecast dataset for this study consists of 50 days with QLCS events from 2017–2020 (Table 2.1). Since WoFS undergoes yearly testing and evaluation during the Hazardous Weather Testbed Spring Forecasting Experiment (e.g., Clark et al. 2020, 2021), most of the archived events are from the spring or early summer months. In this study, the majority of events occur in May and are concentrated in the southern Great Plains

2017	**2018**	**2019**	**2020**
05/04*	05/01*	04/30*	05/05
05/11*	05/02*	05/01	05/07
05/17	05/03	05/02	05/08
05/18*	05/07	05/03	05/13
05/19	05/09	05/06	05/15
05/24	05/12	05/07	05/21
05/27	05/14	05/08	05/22
	05/15	05/16	05/29
	05/19	05/17	06/19
	05/21	05/18	06/21
	05/28	05/20	06/26
	05/29*	05/21	07/17
	06/01	05/24	08/14
		05/28*	08/25
		05/29*	
		07/19	

Table 2.1: List of 2017–2020 QLCS events. *Subset of events used for initial tuning of QLCS identification algorithm (see Section 2.1.2.1).

(Fig. 2.1). This study analyzes hourly 18-member forecasts issued between 2000–0200 UTC for each of the 50 days. The 15[1]-, 60-, 120-, 180-, 240-, 300-, and 360-min forecast times of each hourly-initialized forecast are analyzed to examine forecast progression and fluctuations in verification statistics. Only the 15–180-min forecast times will be analyzed for the 2017–2018 events, as WoFS forecast duration was only 3 hrs during those years.

Gridded composite reflectivity observations from the MRMS system serve as the verification dataset for the WoFS QLCS forecasts. MRMS provides real-time composite reflectivity from WSR-88D observations sampled across the continental United States. The MRMS data are interpolated to the 3-km WoFS grid using a Cressman filter with a 3-km radius of influence (Skinner et al. 2018).

2.1.2 Storm Object Identification and Classification Algorithm

2.1.2.1 Tuning the Storm ID Algorithm

An early version of the storm mode identification and classification algorithm from Potvin et al. (2022) underwent two tuning sessions (hereafter referred to as T1 and T2) to increase the algorithm's efficiency in identifying intense, linear QLCS convective line objects in WoFS and MRMS. T1 is broken into three stages (T1a, T1b, and T1c) and uses subjective methods to verify how well the algorithm is identifying QLCS objects. The purpose of T1 was to provide a starting point for finding the best threshold values that correctly identify and classify WoFS and MRMS objects as QLCSs, which would then be applied during T2 for the entire 2017–2020 dataset (see Table 2.1 for the full list of case days). T2 uses object matching and verification techniques to provide an objective verification for the algorithm.

T1: Subjective Tuning T1 consisted of subjectively analyzing and verifying a subset of nine QLCS case days. Three cases from each year from 2017–2019 were randomly

---

[1] WoFS analyses are not used because they are generated through assimilation of MRMS reflectivity observations and closely resemble the observations (Section 2.1.2.1).

chosen (see the cases with a * in Table 2.1) to examine the impacts of changing specific algorithm parameters on the identification of QLCS objects. At this time, the 2020 cases were unavailable, but because the WoFS configuration was the same as that used in 2019 those tuned parameters should still hold for the 2020 days. During the initial tuning phase, only the WoFS analyses were considered (forecasts are considered later).

T1 began by identifying QLCS objects in WoFS and MRMS using the algorithm's default thresholds (Table 2.2). The resulting objects were then examined to gauge how well the algorithm was identifying all possible QLCS objects in either the WoFS or MRMS output. The objects were categorized as hits, misses, or false alarms relative to subjective identification by the first author so verification statistics could be calculated to quantify the skill of the algorithm's QLCS identification. In this case, a hit was defined as an object identification that matched the subjective analysis, a miss was an object identified subjectively but not by the algorithm, and a false alarm was an object identified by the algorithm but not subjectively. Misses typically occurred when the object's reflectivity was just outside the set threshold, was too small to meet the minimum area threshold, or had a lower eccentricity. False alarms tended to be QLCS stratiform regions or a cluster of cells that were merged together to have the appearance of a QLCS, but were of a different storm mode type (e.g., a line of discrete supercells). The verification statistics for WoFS and MRMS using the default algorithm parameters are shown in Table 2.3.

Table 2.2: Algorithm parameter thresholds for all tuning sessions.

Parameter	**Default**	**T1a**	**T1b**	**T1c**	**T2 Final**
WoFS Minimum Reflectivity (dBZ)	43	39	40	40	45
MRMS Minimum Reflectivity (dBZ)	36.73	38	40	40	40
WoFS Maximum Reflectivity (dBZ)	44.93	41	45	45	50
MRMS Maximum Reflectivity (dBZ)	40.73	40	45	45	45
Minimum Area	135 km^2	135 km^2	135 km^2	225 km^2	54 km^2
Merge Distance	9 km	12 km	12 km	12 km	12 km
Length (L) and Eccentricity (E)	L >150 km, E >0.97	L >126 km, E >0.74	L >100 km, E >0.85 L >150 km, E >0.74	L >100 km, E >0.85 L >150 km, E >0.74	L >100 km, E >0.85 L >150 km, E >0.74

Table 2.3: Verification statistics for the subjective tuning sessions.

Name	**Number of Objects**	**Hits**	**Misses**	**False Alarms**	**POD (%)**	**FAR (%)**	**CSI (%)**
Default WoFS	62	62	124	0	33.3	0	33.3
WoFS T1a	294	232	5	62	97.9	21.1	77.6
WoFS T1b	371	364	7	7	98.1	1.9	96.3
WoFS T1c	267	256	14	11	95.9	3.3	91.1
Default MRMS	130	111	83	19	57.2	14.6	52.1
MRMS T1a	337	247	19	90	92.9	26.7	69.4
MRMS T1b	357	345	6	12	98.3	3.4	95.0
MRMS T1c	249	245	11	4	95.7	1.6	94.2

The default thresholds still missed many QLCS objects in WoFS and MRMS, evident from the high number of misses in Table 2.3. To mitigate some of the problems that occurred while using the default parameters, T1 began by taking a close look at all the identified and unidentified QLCS objects to assess what parameters needed to be changed. This first stage of T1 is referred to as T1a. First, the default reflectivity threshold for MRMS was too low causing the algorithm to classify parts of the stratiform region of the QLCS. That threshold was then increased, as the main goal was to capture the QLCS's convective line. The reflectivity thresholds used for WoFS were too strict, which inflated the number of misses, so those were lowered. Lastly, the eccentricity and length thresholds were too high and had to be lowered as they were causing the algorithm to miss pieces of the QLCS's convective line. The final tuned parameters for T1a are given in Table 2.2 and their verification scores in Table 2.3.

During T1b, or the second stage of T1, the parameters were tuned separately to find the best value that maximized the POD and minimized the FAR scores. The main change between T1a and T1b was in the object length and eccentricity thresholds (Table 2.2). Originally, the default algorithm contained two threshold statements for length and eccentricity. However, only one statement was used in the default and T1a because the other statement was erroneously omitted (Table 2.2). This mistake was found during T1b resulting in the second statement being added back in (Table 2.2). Both length and eccentricity statements were tuned to maximize the amount of QLCS objects being identified but also minimizing the amount of more circular objects (e.g., a supercell) that may be erroneously identified (Table 2.2).

The final stage of T1 (referred to as T1c) addressed an issue where identified QLCS objects included too many smaller reflectivity objects as part of the larger object. To mitigate this, different minimum object area thresholds were tested and the resulting minimum area threshold was changed from 15 to 25 grid cells (Table 2.2). Comparing the verification statistics between T1b and T1c shows a slight decrease in POD and CSI in both WoFS and MRMS, and a small increase in FAR for WoFS. Since the values did not change drastically with the switch in minimum area thresholds, being able to accurately identify the area/extent of QLCS objects without the smaller cells attached to them took precedence. Therefore, the T1c thresholds were used as the final parameter thresholds.

T2: Objective Tuning The majority of the algorithm was tuned during T1, where the parameter thresholds were finalized subjectively using a subset of QLCS cases to expedite the tuning process by not having to run the algorithm over all cases. Instead, the full dataset of cases were only run through the identification algorithm during the objective tuning session (T2) using the finalized thresholds from T1c (Table 2.2). Once the objects were identified in WoFS and MRMS, they were then matched using a total interest score method (Skinner et al. 2018) so that the verification statistics could be calculated using an objective framework. However, once all the cases were run through the algorithm some new issues arose. One such problem was a time discontinuity where the algorithm would correctly identify a QLCS object at one timestep but not at the subsequent timestep, even though the QLCS object was still subjectively present in the forecast.

In an attempt to fix the time discontinuity problem, it was decided to add Gaussian smoothing to the QLCS objects. The smoothing was found to improve the identification of QLCS objects by making the objects more continuous and mitigating gaps between them. Additionally, the time discontinuities more often occurred with smaller QLCS objects. If the area threshold was lowered for unsmoothed objects, the issue from T1b where too many smaller objects were erroneously being included as part of the QLCS's convective line would return. However, by adding smoothing and rearranging the steps in the algorithm's quality control (QC) process, the area threshold was able to be lowered without adding in the smaller objects. Essentially, the QC was rearranged so that it would check the object area before merging all nearby objects together. Thus, small objects that didn't meet the minimum area threshold were thrown out and excluded from the merging process.

Subjective and objective sensitivity tests were conducted to find the best radius of influence for the Gaussian smoothing and a new minimum area threshold. Using only the 9 May 2018 case, various smoothing radii and minimum area thresholds were subjectively analyzed. Smoothing radii of 3, 4, and 5 grid cells, and a minimum area threshold of 4, 5, 6, 7, and 8 grid cells were tested. The goal was to find the optimal radius and area that would result in objects that were more continuous, reduced any time discontinuities, and identified the majority of the object without the inclusion of smaller spurious cells. It was discovered that using a smoothing radius of 4 grid cells and a minimum area of 6 grid cells (54 km^2) accomplished this goal.

Table 2.4: Sensitivity Experiments

Experiment Name	**Description**
Control	Thresholds from T1c (see Table 2.2)
Control_Smooth	Same as Control but with Gaussian smoothing with a radius of 4 grid cells
Smooth_Area6	Same as Control_Smooth but with the minimum area threshold lowered from 25 to 6 grid cells

The optimal values for Gaussian smoothing and minimum area were then used in the objective sensitivity tests to understand how adding/changing each component would affect the verification statistics. These sensitivity experiments are outlined in Table 2.4. The experiments were conducted over a subset of four QLCS case days, which included the best case (17 July 2020), worst case (9 May 2018), and two randomly chosen days from the remaining years (18 May 2017 and 1 May 2019). Each hourly forecast from 2000–0200 UTC at the 0- (analysis), 30-, and 60-min lead times were examined. The resulting POD, FAR, and CSI values for the sensitivity experiments were evaluated (not shown). In all cases, the Smooth_Area6 experiment performed the best, maximizing the POD and CSI values but also minimizing the FAR. Therefore, the neighborhood was applied to all cases and the minimum area threshold was changed to 6 grid cells (54 km^2).

The final change made during the T2 stage was the decision to not include the WoFS analyses in the verification process. Fortunately, only the WoFS reflectivity thresholds would need to be changed when no longer considering the analyses. Since WoFS analyses are generated through assimilation of MRMS reflectivity observations, analysis reflectivity values will more closely resemble observations. Following the analysis, higher composite reflectivity values will be reestablished by WoFS's microphysics scheme (the NSSL two-moment scheme). Therefore, the baseline and maximum WoFS reflectivity thresholds were changed to 45 dBZ and 50 dBZ, respectively, to account for the increase in reflectivity values from the analysis to any forecast time. The final tuned parameters can be seen for T2 in Table 2.2 and their resulting verification statistics are evaluated throughout Section 2.2 .

2.1.3 QLCS Object Identification

To identify QLCS objects across all events, a unique storm mode identification and classification algorithm is used (Potvin et al. 2022). The automated algorithm uses composite reflectivity to identify and classify storms according to a 7-class scheme (Potvin et al. 2022),

Table 2.5: Tuned parameter thresholds for the storm ID and classification algorithm.

Parameter	**Threshold Value**
Minimum Reflectivity	40 dBZ (MRMS); 45 dBZ (WoFS)
Maximum Reflectivity	45 dBZ (MRMS); 50 dBZ (WoFS)
Minimum Area	54 km^2 (6 grid cells)
Merge Distance	12 km (4 grid cells)
Length and Eccentricity	If length $>$100 km then eccentricity $>$0.85 If length $>$150 km then eccentricity $>$0.74

but for this study only the QLCS objects are of interest. The algorithm was adapted in two stages of tuning to improve its skill in identifying intense linear structures characteristic of QLCS convective lines. The complete tuning process and how the defining thresholds for QLCS objects (Table 2.5) were created is outlined in Section 2.1.2.1.

The algorithm's identification process is two-pass. The first pass identifies regions of intense composite reflectivity using a double threshold method (Table 2.5). Initial storm objects in MRMS are identified as regions where composite and maximum reflectivity exceeds 40 and 45 dBZ, respectively, whereas the thresholds for composite and maximum reflectivity for WoFS storm objects must exceed 45 and 50 dBZ, respectively. Storm objects that have areas greater than 6 grid cells and exist within 12 km of each other will be merged into a single object. If the final object meets the criteria in Table 2.5 for minimum area, length, and eccentricity then it will be categorized as a QLCS. A second pass is applied to merge QLCS objects that are likely part of the same system. These QLCS objects have to be within 40 km of each other and have similar orientations (within 30°).

2.1.4 QLCS Object Matching and Verification

The forecasted and observed QLCS objects, and their diagnostic properties (e.g., intensity, area, eccentricity, etc.), are extracted using the Scikit-image python library and the regionprops function (Van der Walt et al. 2014). The forecasted and observed objects are then matched according to a total interest score (TIS; Davis et al. 2006a,b), adapted from Skinner et al. (2018). The TIS is given as:

$$TIS = \frac{(md_{max} - md)}{md_{max}} \tag{2.1}$$

where md is the minimum distance between the object pair and md_{max} is the maximum threshold for object matching, which is set to 40 km (as in Skinner et al. 2018). The TIS is calculated for each of the object pairs and must be greater than 0.2 to be considered a possible match (Skinner et al. 2018; Guerra et al. 2022). Unlike Skinner et al. (2018), the centroid distance is not included in the TIS calculation as the QLCS objects are often large and irregular in size and shape, which causes large variation in centroid placement. One limitation of solely using a minimum distance threshold for matching is that sometimes MRMS objects can be matched to multiple WoFS objects, and vice-versa. To mitigate this occurrence, only the object pair with the highest TIS is retained, and that object pair is known as the best match. If there is a tie between pairs with the highest TIS, then the object pair with the smallest area difference is retained. The tie-breaker ensures the best possible match is made between two objects of similar size.

Object matching allows for the classification of object pairs according to 2x2 contingency table metrics (Brooks 2004). In this study, hits are defined as the best match (if one exists) for each MRMS object, unmatched MRMS objects are classified as misses, and false alarms are unmatched WoFS objects (Fig. 2.2). Extra matches may also occur, which is when a MRMS or WoFS object is matched to multiple WoFS or MRMS objects, respectively (Fig. 2.2). In this case, only the best match is retained and considered a hit, whereas the extra matches are ignored so as to not unfairly reward or punish WoFS (Fig. 2.2).

Correct negatives are not produced through object matching, so verification statistics are limited to those that only use hits, misses, and false alarms in their calculations. Therefore, the verification metrics (Brooks 2004) used herein are probability of detection (POD; Eq. 2.2), false alarm ratio (FAR; Eq. 2.3), critical success index (CSI; Eq. 2.4), and frequency bias (Eq. 2.5). They are given by the following equations:

$$\mathrm{POD} = \frac{\mathrm{H}}{\mathrm{H + M}} \tag{2.2}$$

$$\mathrm{FAR} = \frac{\mathrm{F}}{\mathrm{H + F}} \tag{2.3}$$

$$\mathrm{CSI} = \frac{\mathrm{H}}{\mathrm{H + M + F}} \tag{2.4}$$

$$\mathrm{Bias} = \frac{\mathrm{H + F}}{\mathrm{H + M}} \tag{2.5}$$

where H, M, and F represent hits, misses, and false alarms, respectively. Additionally, matching the MRMS and WoFS QLCS objects enables the comparisons of their diagnostic properties, such as the area, eccentricity, aspect ratio, and the maximum intensity. One limitation of this study is that QLCS cases were selected based on the presence of a QLCS in MRMS. This selection process neglects cases where WoFS members predict a QLCS but one is not observed; therefore, the FAR values presented herein are best thought of as a lower bound of the true FAR.

2.1.5 QLCS Centerlines

A centerline analysis is a technique that enables the examination of specific spatial errors between predicted and observed QLCS objects that are not available through comparison of whole QLCS objects. A centerline is defined as the line that runs lengthwise down the center of the QLCS object and is a proxy for the QLCS's leading convective line. Centerlines are generated for each of the MRMS-WoFS best-matched pairs using a customized python algorithm (Ungar 2022). First, the object is smoothed using a Gaussian filter with a radius of 5 grid points and converted to a binary object (Fig. 2.3b). The binary object is created by giving all points contained within the object the label 1, while all points outside the object are assigned the label 0. The binary object is then converted to a polygon using the Shapely python package (Gillies et al. 2023; Fig. 2.3c). The object polygon is loaded into the centerline algorithm, which identifies the polygon's perimeter and uses a Voronoi diagram technique (Aurenhammer 1991) to extract the polygon's skeleton (Fig. 2.3c). The object's centerline is isolated from the larger skeleton by trimming the shorter branches to find the longest shortest path between any pair of perimeter nodes (Fig. 2.3d). In other words, the shortest paths between all perimeter nodes are calculated and the longest of those paths is then smoothed to become the object's centerline (Fig. 2.4). A limitation of the centerline analysis function is that it typically has higher variability in line placement at either end of the object. To lessen this variability, only the centerline points between the 10th–90th percentiles[2] of its length are analyzed (Fig. 2.4). However, there remains some uncertainty at the centerline endpoints that are, unfortunately, co-located with particularly interesting portions of the QLCS, such as bookend vortices.

Centerline characteristics examined are spatial displacements and differences in length, orientation, and tortuosity. The orientation of the centerline is defined as the angle between east (0°) and the endpoint line. For example, if the centerline orientation is 90° then the line would be purely north-south oriented, with the maximum allowable angle being 179°. Tortuosity is a dimensionless parameter commonly used in health (Ciuricä et al. 2019) and material sciences (Fu et al. 2021) to characterize the porosity of a substance, such as arteries

---

[2] The centerline's coordinates are ordered so that they start at the QLCS's southern tip and end in the north. The percentiles are calculated over the length of the coordinate array so that there is one coordinate pair corresponding to every 5th percentile. Percentiles are used to ensure we are sampling similar parts of the centerline, regardless of its shape or length (e.g., the 50th percentile will always be at the center of the line).

or nerves. In this study, tortousity is used to measure centerline curvature and is calculated using the following equation:

$$\text{Tortuosity} = \frac{L_c}{L_e} \tag{2.6}$$

where L_c is the centerline length and L_e is the length of the centerline's endpoint line (Fig. 2.4). Thus, tortuosity increases as the centerline's curvature increases.

2.2 Results

2.2.1 WoFS Overall Performance

The overall forecast performance of WoFS is assessed by calculating POD, FAR, CSI, and frequency bias for all QLCS events (Fig. 2.5). The statistics are calculated over all events by aggregating the total number of hits, misses, and false alarms for all composite reflectivity ensemble forecasts initialized between 2000–0200 UTC (i.e., 36540 total forecasts). The total number of QLCS objects identified across all events in MRMS is 3207, and the total across all events, initialization times, lead times, and ensemble members in WoFS is 50810 (an average of approximately 2823 objects per member).

WoFS QLCS forecasts have a POD near 0.64 during the first hour of the forecast period (Fig. 2.5a). After 60 min, POD decreases to approximately 0.59 at the end of the 3-hr and 6-hr forecasts (Fig. 2.5a). FAR values for the entire 6-hr forecast period stay below 0.4, with a sharp increase in values evident within the first 60 min (Fig. 2.5b). This sharp increase in FAR also coincides with the increase in POD (Fig. 2.5a) and frequency bias (Fig. 2.5c), and may be attributable to WoFS's convective spin-up process. During this spin-up process, more spurious reflectivity echoes are present in the forecast, which increases POD, FAR, and bias. Skinner et al. (2018) found a similar trend in frequency bias when examining all WoFS reflectivity objects, in which the bias was the highest in the first 60-min of the forecast. After 60 min, the bias[3] begins to decrease with time indicating these weak,

---

[3] Frequency bias was also calculated using the total number of MRMS and WoFS objects, including the objects from the extra matches. The bias still remained between 0.8–0.9 as in Fig. 2.5c. This small change in

spurious storms are short-lived and dissipate by the end of the forecast (Fig. 2.5c). CSI for QLCS forecasts is maximized at the beginning of the forecast with values around 0.52, then subsequently decreases with time with values near 0.46 and 0.44 at the end of the 3- and 6-hr forecast, respectively (Fig. 2.5d). Examining the individual members by PBL scheme shows no substantial differences (Fig. 2.5), consistent with results from previous research by Potvin et al. (2020).

Verification statistics were also generated for all Spring Forecasting Experiment cases that occurred in April and May from 2017–2020 (total of 85 cases; Fig. 2.6). This dataset contains storms of all types, not just QLCSs. Therefore, comparing the two sets of verification statistics (Figs. 2.5 and 2.6) will highlight differences between forecasts for just QLCSs and for all storm types[4]. POD for all storms is maximized within the first 30 min of the forecast, but decreases consistently afterwards (Fig. 2.6a), whereas QLCS forecasts maintain POD values around 0.6 for most of the 6-hr forecast (Fig. 2.5a). QLCS forecasts stay below 0.4 for FAR throughout the 6-hr forecast (Fig. 2.5b), but FAR for all storms passes 0.4 in the first 15 min of the forecast and increases to approximately 0.65 at the end of the period (Fig. 2.6b). Frequency bias for QLCS forecasts lingers just below 1 for the entire forecast (Fig. 2.5c) and is mostly above 1 for forecasts for all storms (Fig. 2.6c). Finally, CSI for QLCS forecasts lingers around 0.5 (Fig. 2.5d), while the CSI for all storms reaches 0.5 at the beginning of the forecast but decreases consistently throughout the rest of the forecast (Fig. 2.6d). Therefore, WoFS is exhibiting higher forecast skill for QLCS objects compared to all storm objects, and that skill is retained throughout the 6-hr forecast. This finding suggests WoFS may be better at forecasting QLCSs over other storm modes

---

bias when including the extra objects indicates the extra objects are nearly evenly distributed between WoFS and MRMS.

[4] Results from the full set of reflectivity objects do not use an identical methodology to the one used herein. Object identification and matching follow the methodology outlined in Guerra et al. 2022, except no object merging is performed (the extra objects are not included in the calculation of contingency table statistics). While this is not a direct comparison, it does provide a general comparison of the accuracy between QLCS and all convective storm forecasts

because QLCSs can be strongly forced (e.g., by a cold front; Wheatley and Trapp 2008) and fairly large, which would make them more easily resolved on the 3-km WoFS grid, and have a longer intrinsic predictability limit (Weyn and Durran 2017, 2019).

WoFS forecast performance can also be assessed by aggregating all events on performance diagrams to examine POD and Success Ratio (SR) differences between events, and how performance changes with forecast time. However, instead of traditional performance diagrams, Figs. 2.7 and 2.8 are formatted like heat maps so one can easily ascertain where the highest concentration of events exist. Each point on the performance heat diagrams represents a single event's ensemble mean POD and SR for each of the hourly-initialized forecasts at that specific forecast time (Fig. 2.7). Therefore, each event may have up to seven points on each diagram in Fig 2.7, one for each of the 2000–0200 UTC forecasts. The points are then sorted into 0.1 POD x 0.1 SR bins. Finally, all points from each panel in Fig. 2.7 are aggregated onto a single performance heat diagram covering the 6-hr forecast period (Fig. 2.8).

The heat diagrams are separated by forecast time to understand how WoFS performance changes with forecast progression (Fig. 2.7). Inspection of the performance heat maps by forecast time reveals three main areas where the majority of events are concentrated: the upper-right corner, the right side where POD = 0.5, and the lower-left corner (Figs. 2.7 and 2.8). The key reason why these locations are favored is because QLCSs are often sparse (i.e., only one or two objects) within the WoFS domain for any given forecast. For example, if there are only 2 observed QLCS objects then WoFS will either correctly identify all objects, identify one but miss the other, or miss both objects. This results in the three favored locations seen on the performance heat diagrams (Figs. 2.7 and 2.8). The upper-right corner is where POD and SR equal 1, indicating a perfect forecast. Having events clustered in this location suggests WoFS is able to forecast many QLCS events very well, without missing any objects. The second location is along the right-side of the diagram where POD = 0.5 and SR = 0.8–1.0. Having events in this area means WoFS is predicting half of the objects correctly, but missing the other half. Finally, the last favored location is in the lower-left corner near zero, indicating WoFS missed all objects in the forecast.

While the favored locations do not change with forecast time, the percentage of events in those locations does (Fig. 2.7). In the upper-right corner, the percentage of perfect forecasts decreases with forecast time, whereas the percentage of missed forecasts (i.e., those with POD = 0 and SR = 0) increases with time. Note the decrease in sample size from 180 min (Fig. 2.7d) to 240 min (Fig. 2.7e) because the 2017–2018 events have a maximum forecast period of 3 hrs.

There are 260 missed (i.e., no hits in WoFS) QLCS events across all forecasts, accounting for 14% of all events (Fig. 2.8). Approximately 50% of these missed forecasts occur during the 2000–2200 UTC initializations (not shown). Past studies have found the accuracy of WoFS forecasts is primarily dependent on the maturity of the storm within WoFS's initial conditions (Flora et al. 2019; Guerra et al. 2022). The higher proportion of missed events in early forecast initializations is consistent with the fact that QLCSs often haven't matured or even initialized by 2000–2200 UTC, in which case they are not accurately represented in the WoFS initial conditions.

The performance diagrams show a consistent low-bias in WoFS (Figs. 2.7 and 2.8) that was also evident in Fig. 2.5c where the bias was less than one for the whole 6-hr forecast. There is a high concentration of events that exist below the bias = 1 line, meaning WoFS is underforecasting the number of QLCS objects in the majority of events (Figs. 2.7 and 2.8). This low-bias may be attributable to a few factors. Subjective analysis of QLCSs within MRMS and WoFS found that it is common for MRMS QLCSs to be broken into multiple objects, whereas the full convective line may be only one object in WoFS. MRMS also contains more stratiform region objects that often go unmatched. Both situations generate more objects in MRMS than WoFS, which would lead to the overall low bias. The bias may also be manipulated by changing the thresholds in the object identification algorithm[5].

---

[5] Changing the thresholds may change the numerical values, but the overall trends remain the same.

The algorithm for this study was tuned to match subjective interpretation and to optimize performance (Section 2.1.2.1).

2.2.2 QLCS Object Characteristics

Comparing WoFS and MRMS QLCS object characteristics from each best match identified differences in area (Fig. 2.9a), maximum intensity (i.e., reflectivity; Fig. 2.9b), aspect ratio (Fig. 2.9c), and eccentricity (Fig. 2.9d). All differences are calculated by subtracting the MRMS value from the WoFS value. Therefore, positive values indicate the WoFS object value is larger than the MRMS value, and vice-versa.

Analysis of object area differences shows WoFS objects are on average larger than MRMS objects at later forecast times (Fig. 2.9a). The positive area bias may be connected to the substantial positive bias observed in object maximum intensity (Fig. 2.9b), indicating WoFS objects are more intense than MRMS objects. Part of this positive intensity bias is attributable to the Cressman filter that was applied to MRMS reflectivity, which typically reduces the maximum intensity by about 5 dBZ. Additionally, WoFS uses the NSSL two-moment microphysics scheme, which was found to overpredict reflectivity values (Skinner et al. 2018). Closer visual examination of the WoFS QLCS events found the WoFS QLCS objects typically include more of the stratiform region than do the MRMS objects (Fig. 2.10). While WoFS QLCS objects are larger than those in MRMS, the spatial coverage of the full storm in WoFS is generally much smaller (Fig. 2.10). The storms in WoFS also appear to have little to no transition zone (Biggerstaff and Houze 1993), which is an area of low reflectivity that exists between the leading convective line and the trailing stratiform region (Fig. 2.10). The lack of a transition zone removes the boundary separating the stratiform precipitation from the convective line, making it easier for more of the stratiform region to be included as part of the convective line object. This pattern is consistent with more of the stratiform region being identified with the convective line objects in WoFS and the size difference between WoFS and MRMS objects (Fig. 2.9a).

Differences in object aspect ratio and eccentricity also suggest WoFS is retaining too much of the stratiform region compared to MRMS (Fig. 2.9c,d). Aspect ratio differences show a consistent positive bias across forecast time (Fig. 2.9c). Recall, aspect ratio is the ratio of minor axis length to major axis length. Hence, positive aspect ratio differences indicate MRMS objects have shorter minor axes compared to WoFS objects (Fig. 2.9c). Additionally, if MRMS objects have shorter minor axes then the objects will also appear slimmer and more eccentric, which is evident from the negative eccentricity bias (Fig. 2.9d). Conversely, these biases indicate WoFS objects have wider minor axes and lower eccentricities (Fig. 2.9c,d), which is consistent with the WoFS objects retaining more of the stratiform region (Fig. 2.10).

2.2.3 QLCS Centerline Analysis

Centerline analyses allow for the quantification of specific errors in QLCS convective line characteristics that are not available in typical object-based diagnostics. Differences in centerline tortuosity (Fig. 2.11a), length (Fig. 2.11b), and orientation (Fig. 2.11c) between best-matched pairs are evaluated to understand how the simulated WoFS QLCSs differ from those in MRMS.

The 60–180-min forecasts show a slight negative bias in tortuosity indicating MRMS centerlines are typically more curved within this time period (Fig. 2.11a). Following the 180-min forecast, the bias becomes positive meaning the WoFS centerlines have slightly more curvature than MRMS at longer forecast times (Fig. 2.11a). The large separation between the mean and median tortuosity values (Fig. 2.11a) may be attributable to the high-end bow echo events. Since not all QLCSs contain bowing segments, or even transition to a bow echo, those that do will skew the mean tortuosity because they have more curvature than standard QLCSs. Centerline length differences show a small negative bias throughout the entire 6-hr forecast, indicating MRMS centerlines are typically longer than those in WoFS (Fig. 2.11b). Finally, differences in orientation angle show a positive bias that increases with forecast time (Fig. 2.11c). On average, MRMS centerlines are oriented between 60–70° (not shown), while WoFS centerlines start off oriented between 60–80° then rotate cyclonically with increasing forecast time (not shown). Therefore, WoFS centerlines tend to be oriented in the same direction as MRMS centerlines (southwest-northeast direction) at the beginning of the forecast, but become more aligned in the south-north direction at the end of the forecast (see the centerline panels in Fig. 2.12; further discussion later).

The cyclonic rotation of WoFS centerlines and the spatial displacement between MRMS and WoFS centerlines is further explored in Figs. 2.13 and 2.14. Spatial displacement calculations between WoFS and MRMS centerlines are simplified by comparing every 5th-percentile in the centerlines. The result is one coordinate pair for WoFS and MRMS corresponding to each percentile that can then be easily used to find the displacement between lines. Displacement calculations use the WoFS centerline position as the reference point and subtract the MRMS position. For example, a northern bias indicates WoFS centerlines are located to the north of MRMS centerlines. Kernel density estimation (KDE) is used to highlight areas where the majority of the full distribution's displacement occurs (Fig. 2.13).

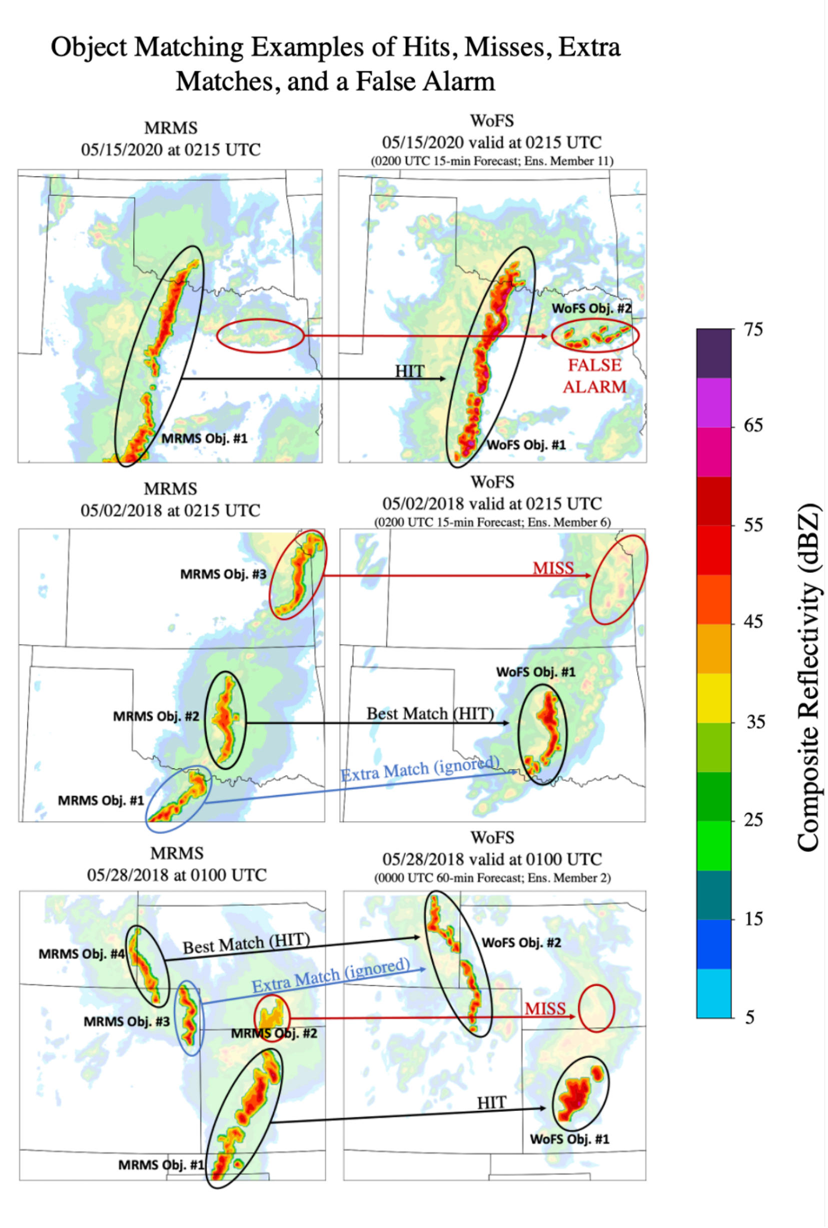

Figure 2.2: MRMS composite reflectivity (left panels) and WoFS composite reflectivity forecasts (right panels) displaying examples of hits, misses, extra matches, and a false alarm in the object matching process. Best matches in MRMS are considered hits, unmatched MRMS objects are classified as misses, and false alarms are unmatched WoFS objects. Extra matches occur when a single MRMS or WoFS object is matched to multiple WoFS or MRMS objects, respectively. Only the best match is retained and the extra matches are ignored.

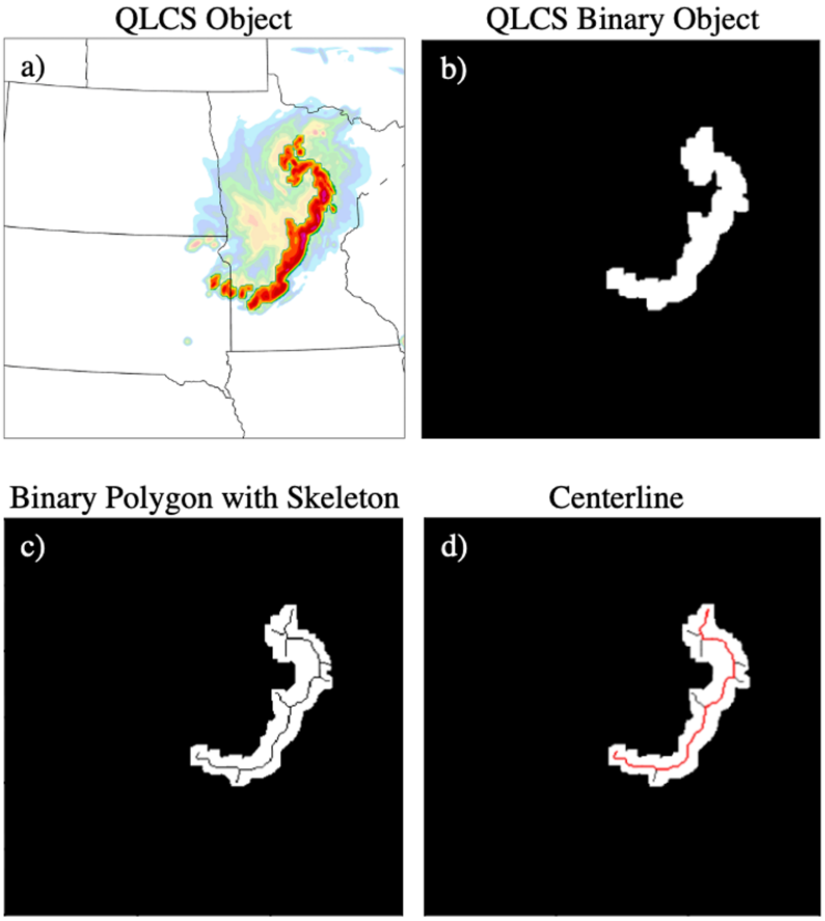

Figure 2.3: Illustration of the centerline creation process. Starting with a) the QLCS object of interest, b) QLCS object converted to a binary object, c) binary object converted to a polygon with object skeleton overlaid (black line), and d) the resulting centerline (red) from the full skeleton. The centerline is then smoothed to create the final centerline product as shown in Fig. 2.4.

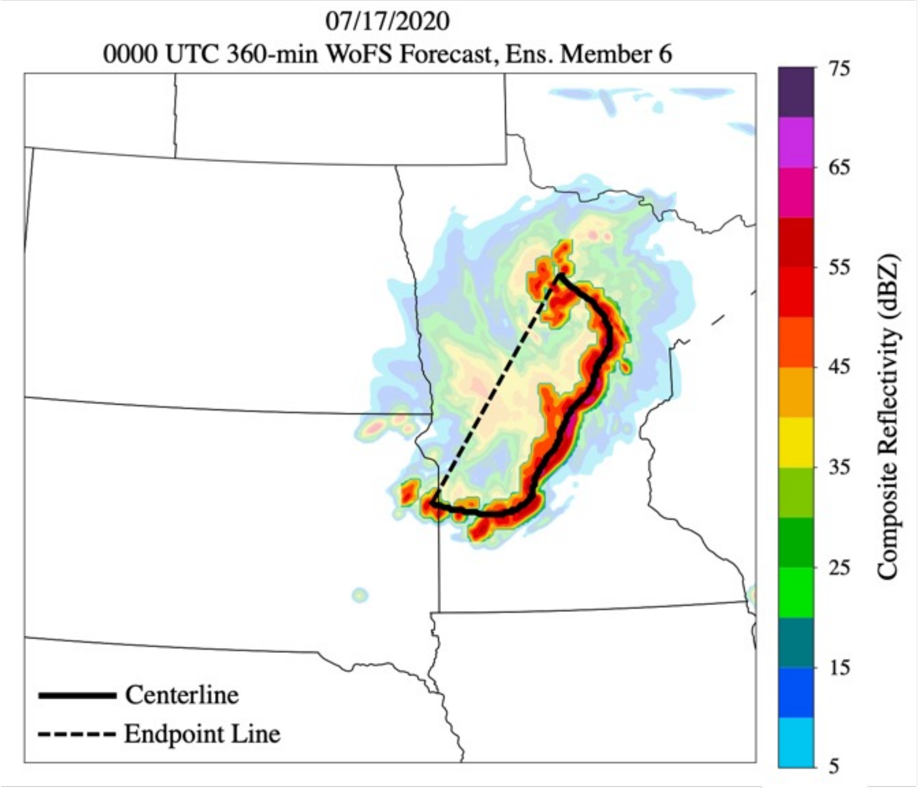

Figure 2.4: Example of a centerline overlaid on the WoFS output for the 17 July 2020 QLCS during the 0000 UTC forecast for ensemble member 6 at the end of the 6-hr forecast. The centerline (solid black line) extends from the 10th–90th percentiles of the total QLCS object's length. The endpoint line (dotted black line) is the straight path connecting the centerline's endpoints. The QLCS object is represented as the outlined area of reflectivities, with the faded area of reflectivities being the full WoFS output at this time.

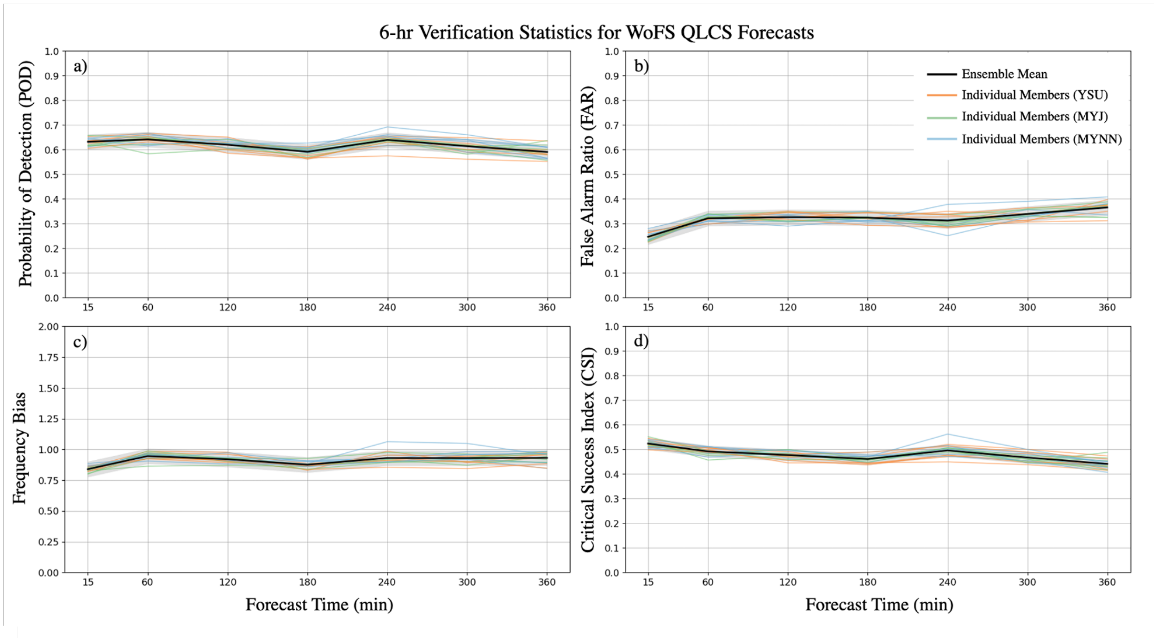

Figure 2.5: Time series of verification statistics for WoFS QLCS forecasts: a) POD, b) FAR, c) frequency bias, and d) CSI. The ensemble mean is in black and the individual ensemble members (1–18) are represented by thin orange, green, and blue lines that represent the ensemble members with YSU, MYJ, and MYNN PBL schemes, respectively. Gray shading denotes the 95% confidence interval using a bootstrapping technique with replacement (N = 10000). The ensemble mean is found by aggregating all hits, misses, and false alarms over all composite reflectivity forecasts initialized between 2000–0200 UTC for all years and ensemble members.

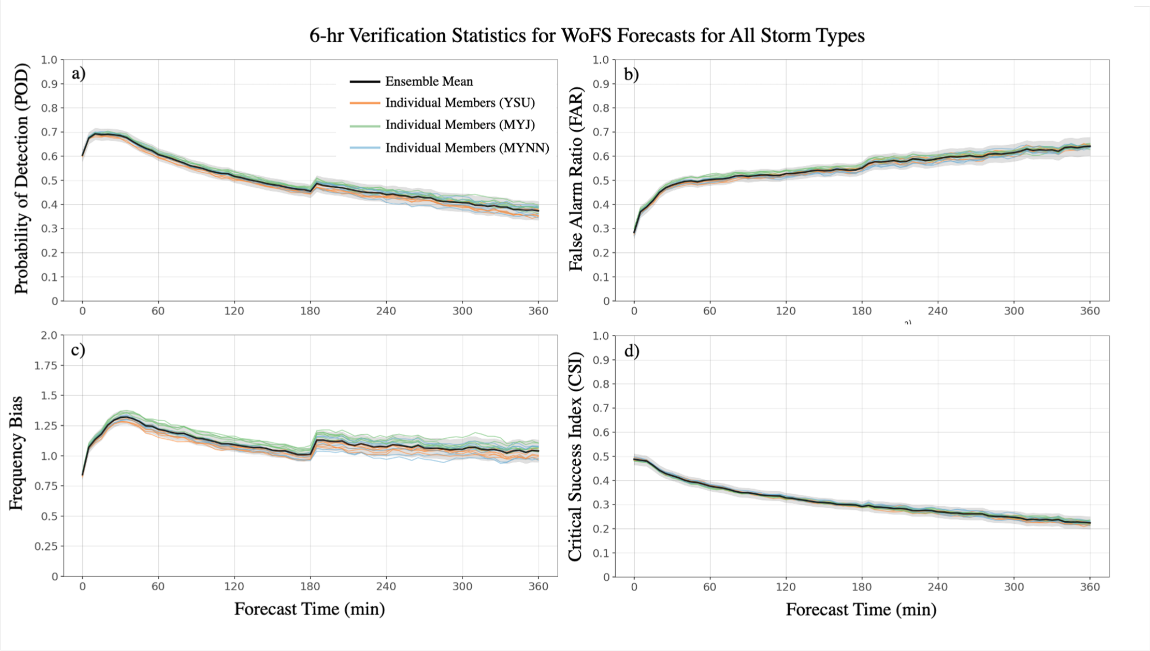

Figure 2.6: Same as in Fig. 2.5, but for all Spring Forecasting Experiment (SFE) cases in April and May from 2017–2020 (85 total events), and data is output every 5 min. The slight increase in POD, FAR, and bias at the 180-min forecast time occurs because of the shift from DART to GSI DA software. Figure courtesy of Patrick Skinner.

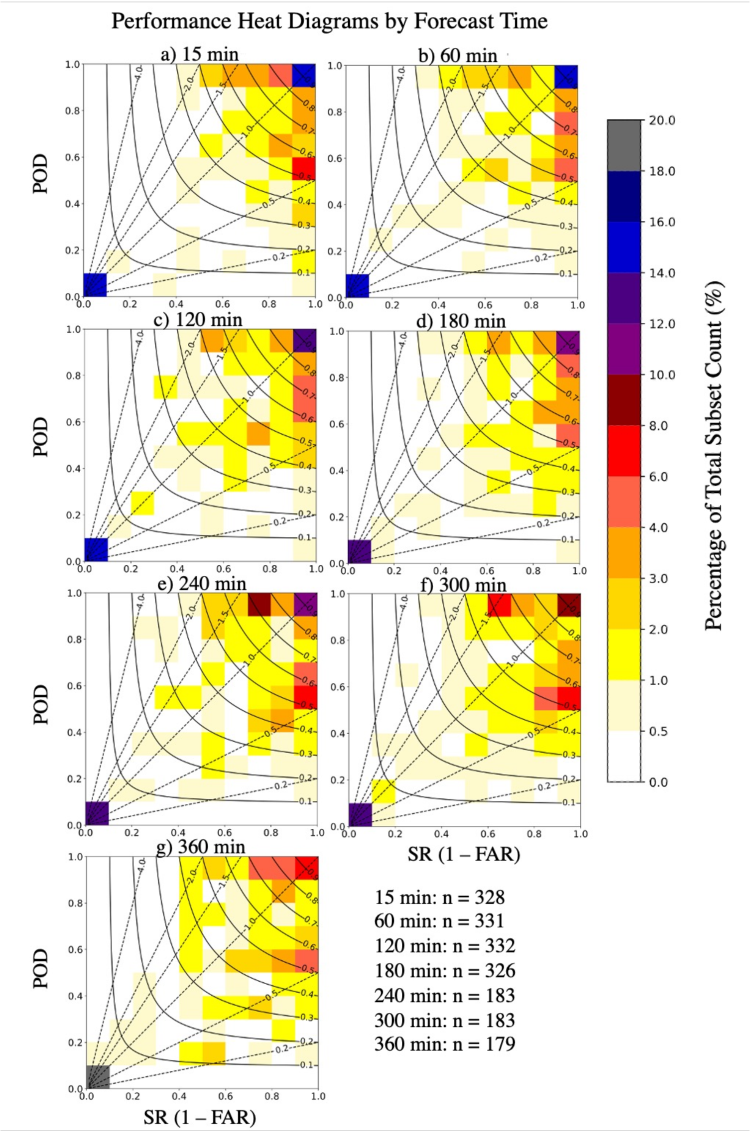

Figure 2.7: Performance diagrams displayed as heat maps to easily show the locations that contain the highest percentage of points. Each point represents the event's ensemble mean POD and SR for a single forecast at that specific forecast time (up to seven points total from the 2000–0200 UTC forecasts for each event). Each panel represents one forecast time: a) 15 min, b) 60 min, c) 120 min, d) 180 min, e) 240 min, f) 300 min, and g) 360 min. The black dotted lines and curved lines represent bias and CSI, respectively. The total number of forecasts (n) used in each panel is shown in the bottom right corner.

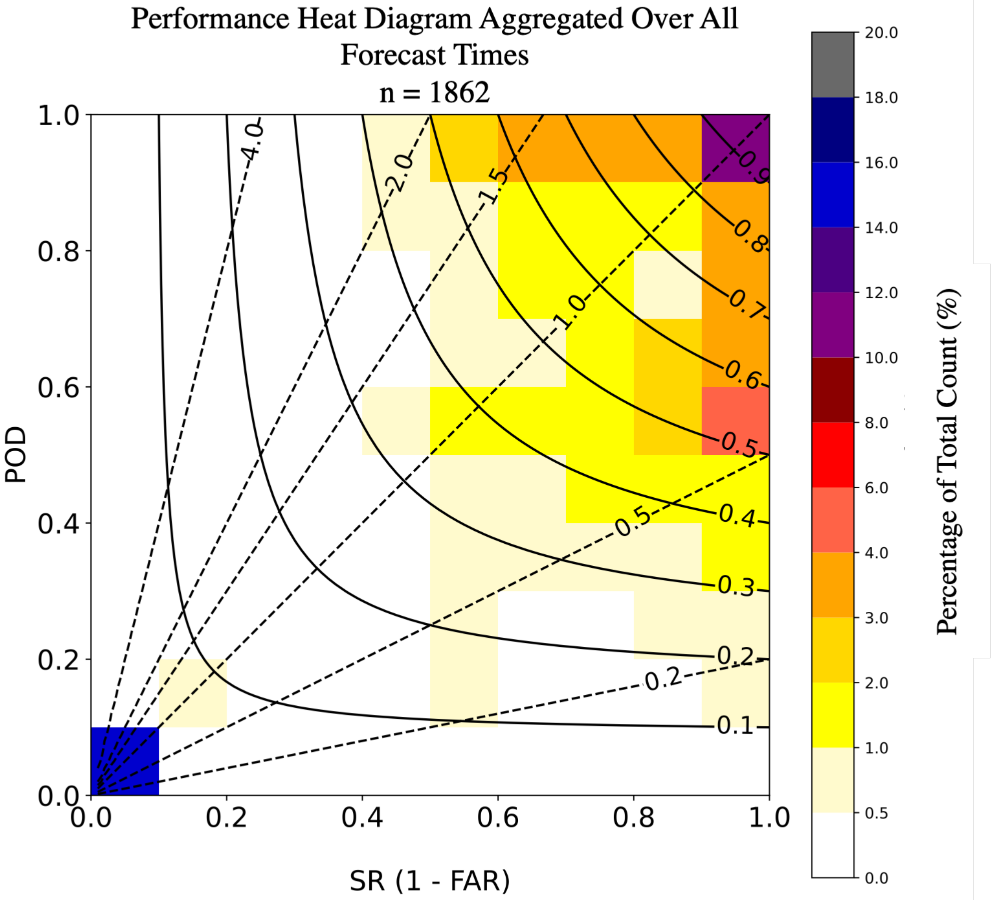

Figure 2.8: All panels in Fig. 2.7 aggregated onto one plot for all forecast times. The total number of forecasts used is given by n.

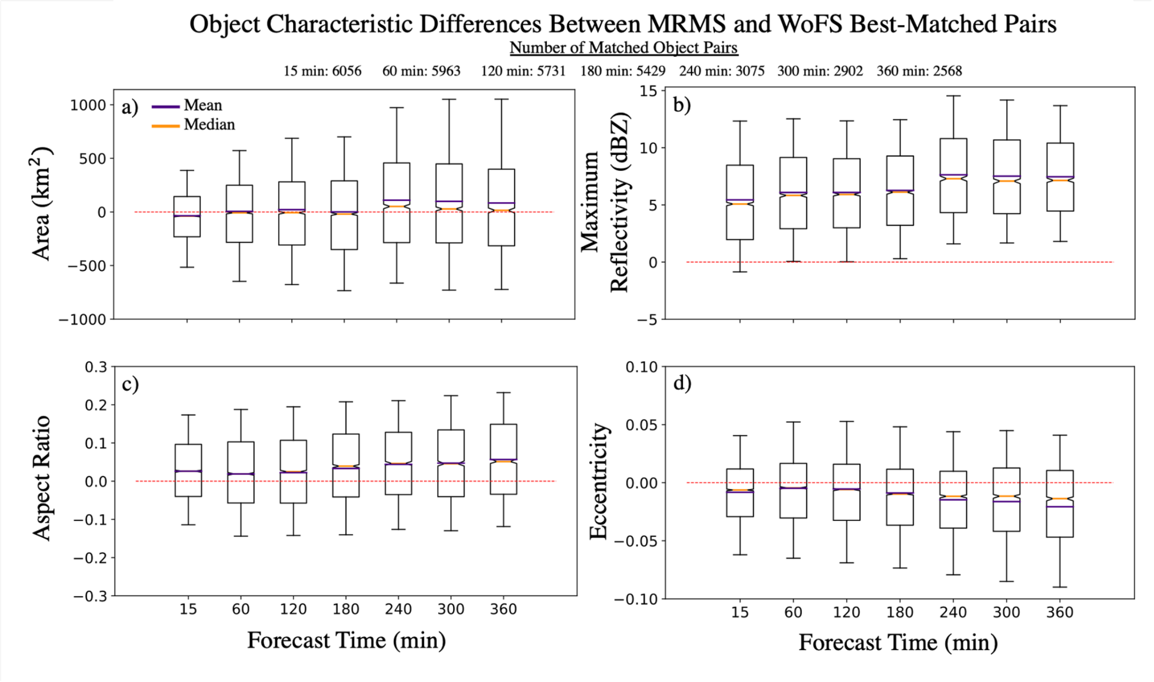

Figure 2.9: Notched boxplots illustrating the differences in object a) area, b) maximum intensity, c) aspect ratio, and d) eccentricity between WoFS and MRMS best-matched pairs with increasing forecast time. Differences are calculated by subtracting the MRMS value from the WoFS value. The dotted red, solid purple, and solid orange lines represent the zero line, mean, and median, respectively. Whiskers extend to the 10th and 90th percentiles. Notches represent the 95% confidence interval of the median using a bootstrap method with replacement (N = 10000).

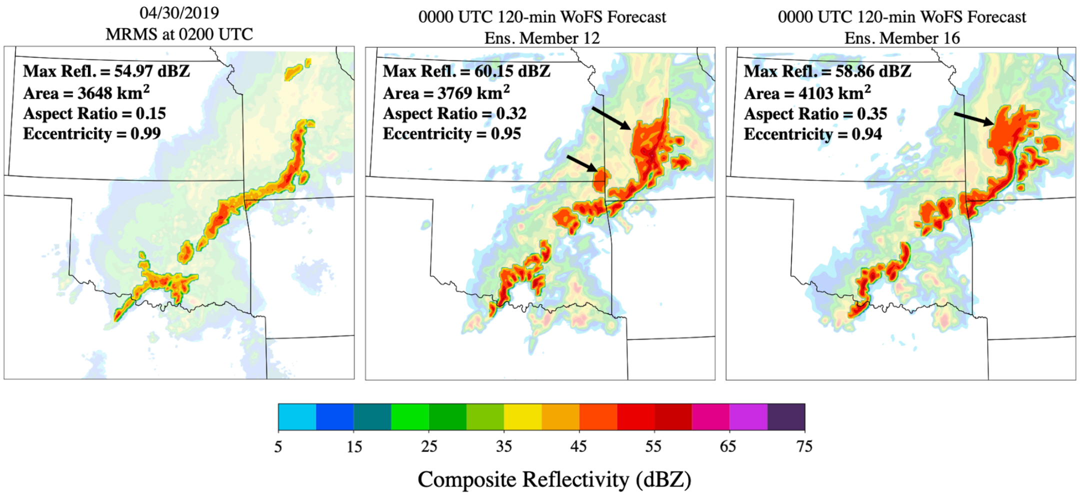

Figure 2.10: Illustration of object characteristic differences in MRMS (left panel), and in the 0000 UTC 120-min WoFS forecasts for ensemble member 12 (center panel) and 16 (right panel). Object properties (maximum reflectivity, area, aspect ratio, and eccentricity) are annotated in the upper left corner of each panel. Black arrows denote the areas of stratiform being included as part of the convective line object. WoFS objects tend to be more intense and include more of the stratiform region, which leads to the objects having higher aspect ratios and lower eccentricities compared to MRMS objects.

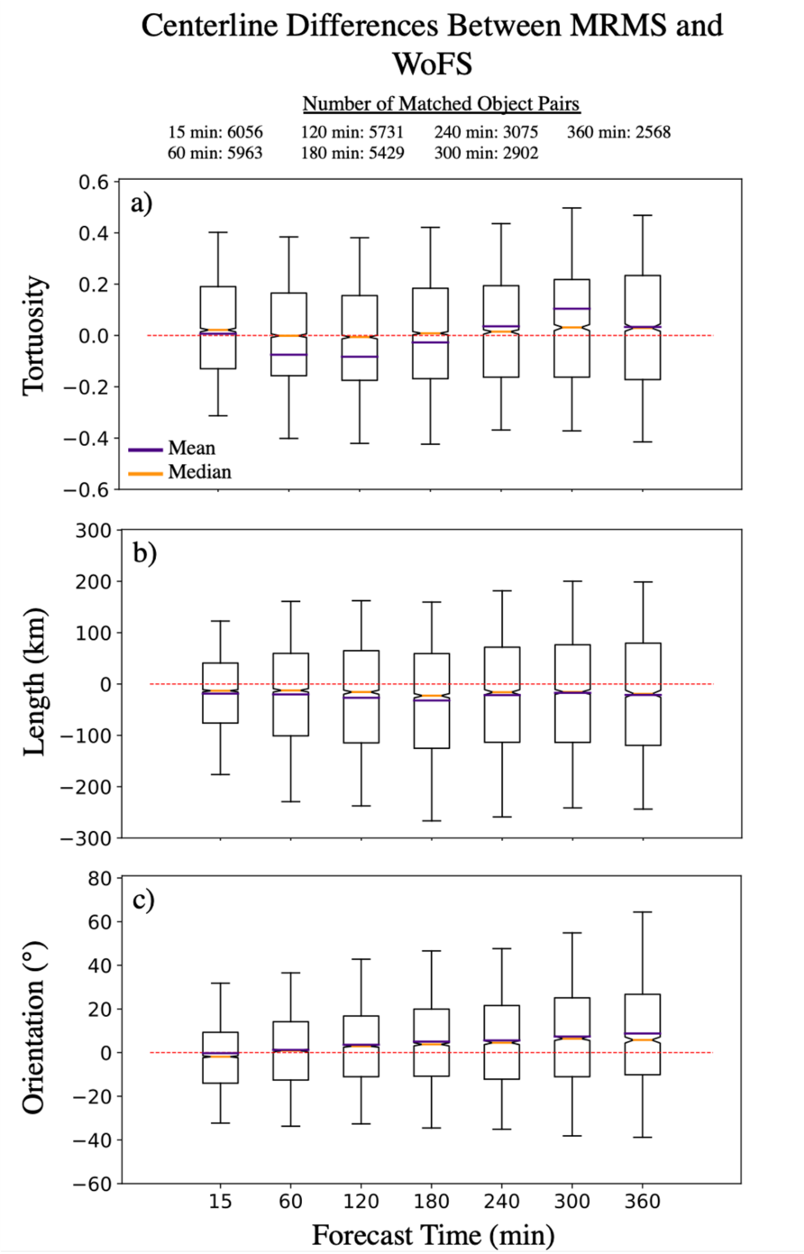

Figure 2.11: Similar to Fig. 2.9, but showing the differences in a) tortuosity, b) length, and c) orientation between the WoFS and MRMS best-matched centerline pairs. Differences are calculated by subtracting the MRMS value from the WoFS value.

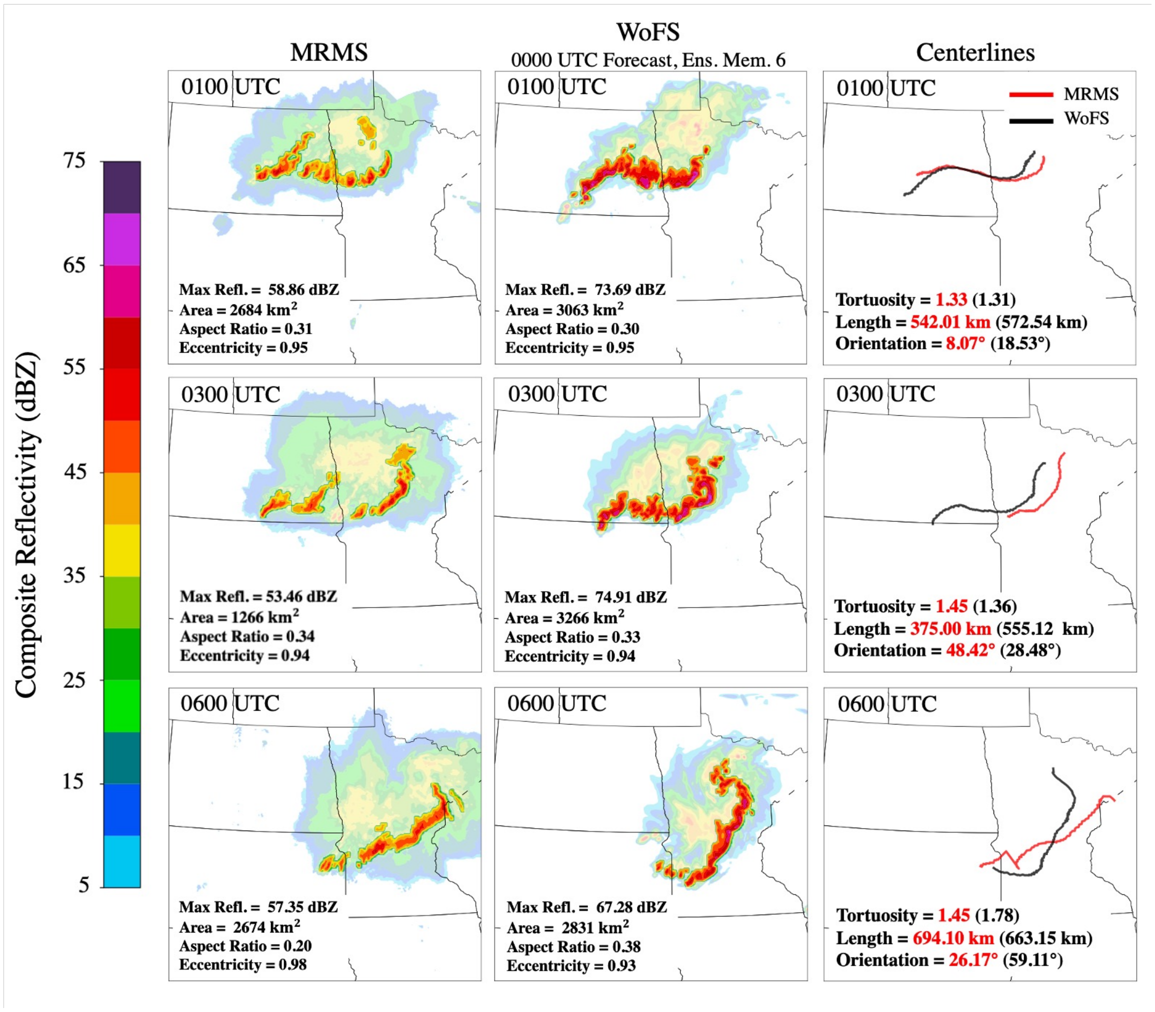

Figure 2.12: MRMS composite reflectivity (left column), WoFS composite reflectivity (middle column), and the object centerlines (right column) from the 17 July 2020 QLCS event. The time that each panel is valid for is given in the top left of each panel. The WoFS 60-,180-, and 360-min forecasts are from the 0000 UTC initialization for ensemble member 6. MRMS and WoFS centerlines are red and black, respectively, with their associated tortuosity, length, and orientation properties annotated in their respective color. Note: There are two QLCS objects present in MRMS at 0300 UTC but the right-most object is the best match and, therefore, used for comparison to the WoFS object.

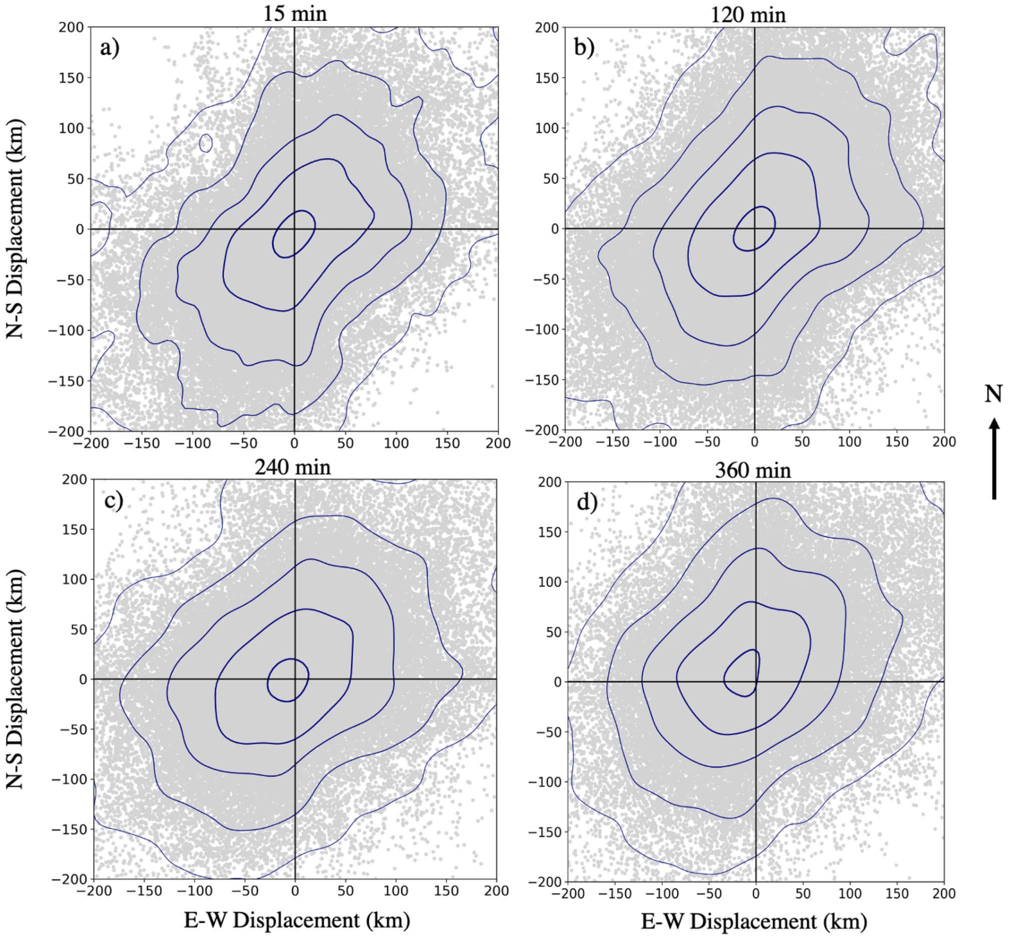

Figure 2.13: North-South (N-S) and East-West (E-W) displacement between every 5th percentile along the MRMS and WoFS centerlines for the a) 15-min, b) 120-min, c) 240-min, d) 360-min forecasts. Blue contours represent the KDE contours for the 90th, 95th, 97.5th, 99th, and 99.9th percentiles. Displacement is calculated by subtracting the MRMS position from WoFS.

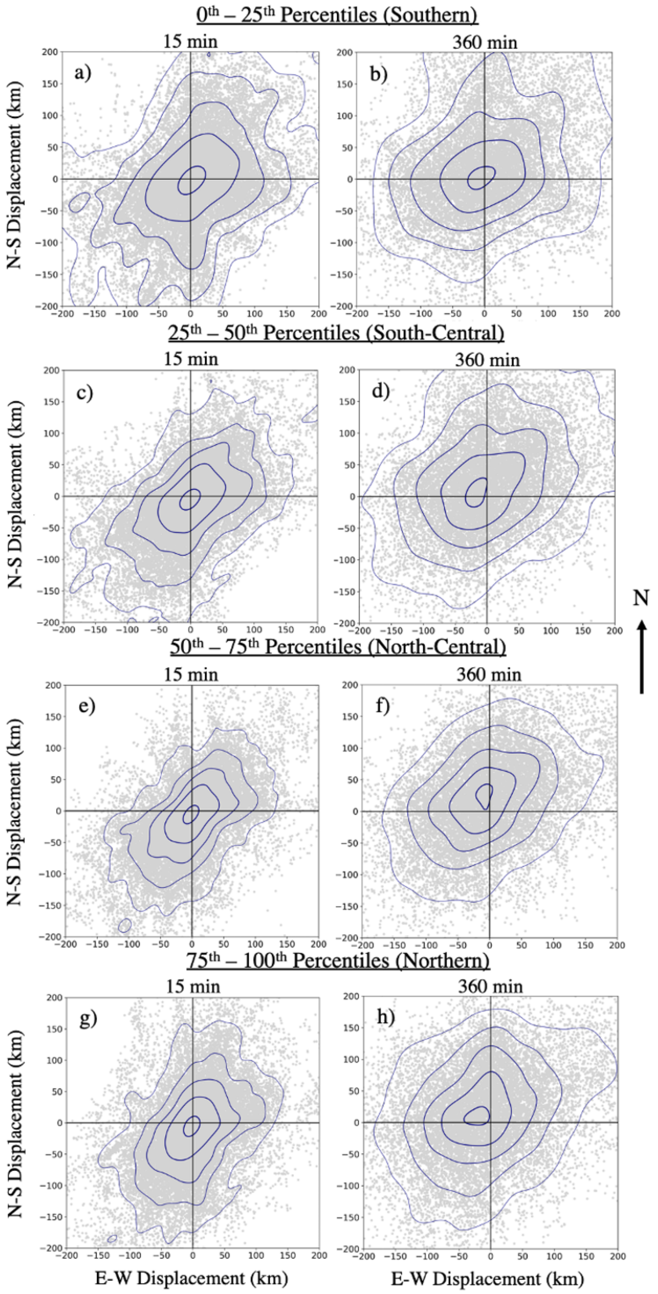

Figure 2.14: Same as Fig. 2.13 except the QLCSs are divided into four portions: a–b) the southern end (0–25th percentiles), c–d) south-central section (25–50th percentiles), e–f) north-central section (50–75th percentiles), and g–h) northern end (75–100th percentiles) for the 15-min (left column) and 360-min (right column) forecasts.

Separating the displacement by forecast time allows for the examination of potential biases that may exist at certain times in the forecast or that grow with time (Fig. 2.13). During the first 3 hrs of the forecast, the displacement is evenly centered around the origin (Fig. 2.13a,b). However, the displacement begins to shift towards the northwest following the 3-hr forecast (Fig. 2.13c,d), indicating WoFS centerlines are typically located to the northwest of MRMS centerlines. The full displacement distribution has the shape of a rectangle with a major axis oriented from roughly southwest to northeast (Fig. 2.13). When the displacement is in the northeast quadrant then the WoFS centerline is traveling ahead of MRMS, but if the displacement is located in the southwest quadrant then the MRMS centerline is leading WoFS. Therefore, more spread in the northeast and southwest directions suggests the storm propagation speed is most likely the main factor contributing to the displacement between centerlines given that the spread occurs along climatologically favorable QLCS propagation vectors. While WoFS QLCS propagation errors are often large, they are relatively unbiased overall.

Centerline displacement is dissected further by dividing the QLCS centerlines into four sections based on percentiles ranges: the southern end (0–25th percentiles; Fig. 2.14a,b), south-central portion (25–50th percentiles; Fig. 2.14c,d), north-central portion (50–75th percentiles; Fig. 2.14e,f), and the northern end (75–100th percentiles; Fig. 2.14g,h).

The displacement in the 15-min forecasts (Fig. 2.14a,c,e,g) is similar to Fig. 2.13a in that it is mostly centered around the origin. However, at the end of the 360-min forecasts there is an evident shift in the highest density of displacements away from the origin by approximately 25 km (Fig. 2.14b,d,f,h). The southernmost end has a mostly southern displacement bias, indicating the southern portions of WoFS QLCSs tend to be displaced to the north of those in MRMS (Fig. 2.14b). The south- and north-central portions of the QLCS show similar displacement biases to the north (Fig. 2.14d,f), with the south-central portion (Fig. 2.14d) having a larger western component to its bias than seen in the north-central portion (Fig. 2.14f). Lastly, the northern ends of WoFS QLCSs are located to the northwest of that observed with MRMS (Fig. 2.14h). The shift in WoFS centerlines to the northwest with increasing forecast time corroborates the cyclonic change in orientation angle that was observed in WoFS centerline properties (Fig. 2.11c).

2.3 Discussion

A QLCS event that occurred on 17 July 2020 is chosen as a representative example to synthesize and discuss the results presented within this study (Fig. 2.12). This QLCS developed in North Dakota and progressed southeast into Minnesota and parts of South Dakota. This convective system was associated with over 100 wind, 29 hail, and 7 tornado reports.

This QLCS was predicted accurately by WoFS, with a total POD, FAR, CSI, and frequency bias of 0.94, 0.05, 0.90, and 0.99, respectively. However, there remain many differences between the simulated WoFS QLCS and the one present in MRMS (Fig. 2.12). First, the maximum composite reflectivities for the WoFS QLCS objects are about 10–20 dBZ higher than those in MRMS (Fig. 2.12), which is consistent with the large positive bias in maximum reflectivity between WoFS and MRMS objects for all events (Fig. 2.9b). Additionally, the WoFS QLCS object is larger in size, which corroborates the positive area bias between WoFS and MRMS QLCSs (Fig. 2.9a).

One of the largest differences between the simulated QLCS in WoFS compared to MRMS is WoFS predicts a more intense northern bookend vortex[6] (Fig. 2.12). Bookend vortices are a pair of counterrotating vortices that typically form in the midlevels (3–7 km) on either end of the bow echo (Weisman 1993; Weisman and Davis 1998; Atkins et al. 2004; Meng et al. 2012). The northern, cyclonic bookend vortex is usually favored through the convergence of planetary vorticity and will grow stronger than the southern, anticyclonic vortex (Wheatley and Trapp 2008; Atkins and Laurent 2009b). Previous work (Weisman

---

[6] Subjective analysis found this overprediction occurs at least once in 40 out of the 50 QLCS events.

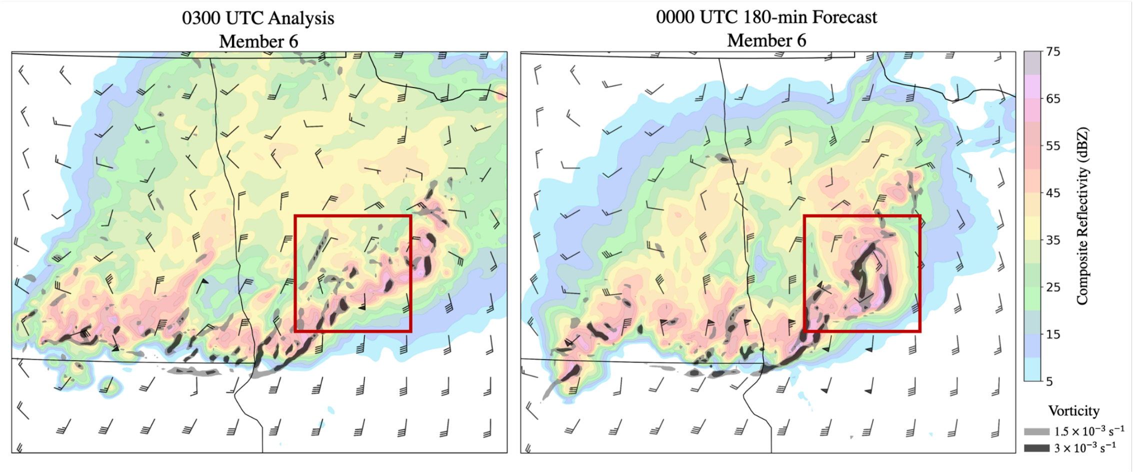

Figure 2.15: Composite reflectivity, 1-km wind barbs (kt), and 1-km vorticity for the 17 July 2020 QLCS event. The 0300 UTC analysis for ensemble member 6 (left) is compared to the 180-min forecast for member 6 initialized at 0000 UTC (right). The WoFS forecast shows an intense northern bookend vortex and rear inflow jet located within the red box that is not present in the analysis.

1992, 1993; Grim et al. 2009) has shown that the combined circulation between the bookend vortices can contribute to the development and intensification of the RIJ (Smull and Houze 1987b). Therefore, WoFS's intense northern bookend vortex may be indicative of a strong RIJ that is causing convective lines in WoFS QLCSs to bow out more than those in MRMS QLCSs (Fig. 2.12). These bowing segments may not be system-wide, but localized near the northern bookend vortex. Further evidence of this overprediction occurring in WoFS can be found in Fig. 2.15 where there is an intense northern bookend vortex and RIJ present in the 180-min forecast, but is absent in the analysis.

The overprediction of the northern bookend vortex and RIJ intensity in WoFS is also consistent with the results of the centerline analysis. Differences in centerline properties found WoFS centerlines tend to be more tortuous (Fig. 2.11a) and their orientations turn cyclonically with increasing forecast times (Fig. 2.11c). An intense RIJ may cause the WoFS centerlines to bow out more, thus increasing the line tortuosity with time (Fig. 2.12). Similarly, a stronger northern bookend vortex is consistent with the cyclonic rotation of the QLCS's orientation, and why WoFS QLCSs tend to be displaced to the northwest of MRMS QLCSs (Figs. 2.13 and 2.14). This cyclonic rotation in orientation is evident in the last centerline panel in Fig. 2.12.

2.4 Summary

WoFS has been shown to accurately forecast a variety of severe convective events. However, evaluating WoFS's capability to accurately forecast QLCSs using a large number of events has yet to be assessed. Therefore, this study examines 50 QLCS days between 2017–2020 to assess WoFS's capability to predict QLCS spatial extent, timing, and propagation. The WoFS QLCS forecast performance is evaluated using object-based verification techniques and a novel centerline analysis used to highlight potential biases in spatial displacement, tortuosity, length, and orientation that may exist when comparing the QLCSs from WoFS and MRMS.

Results show WoFS has skill in forecasting QLCSs out to 6 hrs of forecast time with POD, FAR, and CSI values of the 3-hr forecasts (0.57, 0.35, and 0.44) being similar to those at the end of the 6-hr forecasts (0.55, 0.39, and 0.42; Fig. 2.5). On the other hand, verification statistics for all storm types have lower POD and CSI values, and much higher FAR values (Fig. 2.6a,b,d), suggesting WoFS is able to more accurately predict QLCSs than other storm modes. This is expected as QLCSs are larger and longer-lived systems and, therefore, should have longer intrinsic predictability limits than cellular convection (Weyn and Durran 2017, 2019).

We found that WoFS QLCS objects are typically larger, more intense, and less eccentric than MRMS QLCS objects, especially at longer forecast times (Fig. 2.9). The larger size of WoFS objects is partly attributable to them including more of the QLCS stratiform region, which in turn may be due to them having little to no transition zone that would provide a boundary between the leading convective line and the trailing stratiform region (Figs. 2.10 and 2.12). Additionally, centerline property differences found WoFS QLCSs are more tortuous and rotate cyclonically in orientation with increasing forecast time (Fig. 2.11). These results are consistent with WoFS overforecasting the intensity of the QLCS's northern bookend vortex and RIJ, which is evident in a representative case study from 17 July 2020 (Figs. 2.12 and 2.15).

Chapter 3

Forecasting QLCS Mesovortex Tornado Potential

For simplicity and brevity, line-normal and line-parallel shear will hereafter be represented as LN and LP, respectively.

3.1 Data and Methods

3.1.1 Case Selection

The main objective of Part II of this study is to investigate the potential of using LN shear, LP shear, and local line geometry to predict areas favorable for mesovortex tornadogenesis. To address this objective, three high-impact QLCS case studies are analyzed: 12 May 2022, 30 March 2022, and 15 December 2021 (Fig. 3.1). These cases vary in time of day, season, location, environment, and QLCS structure to allow for the examination of how the prediction of mesovortex tornado potential changes with respect to these different factors. Overviews for the 12 May 2022, 30 March 2022, and 15 December 2021 are provided in Sections 3.2.1.1, 3.2.2.1, and 3.2.3.1, respectively.

3.1.2 QLCS Object Identification and Isolation

The object identification and classification for the three QLCS case studies applies the same methods as outlined in Section 2.1 using the automated algorithm from Potvin et al. (2022), with the exception of a couple minor changes. First, a smaller dataset allowed for the object identification thresholds to be tuned for each specific case study (Table 3.1). For each of the WoFS cases, two thresholds are used for the minimum and maximum reflectivities. The first threshold is for the analysis only, or the 0-min forecast, and the second threshold is for all subsequent forecast times (in 5-min increments; Table 3.1). The analysis typically has

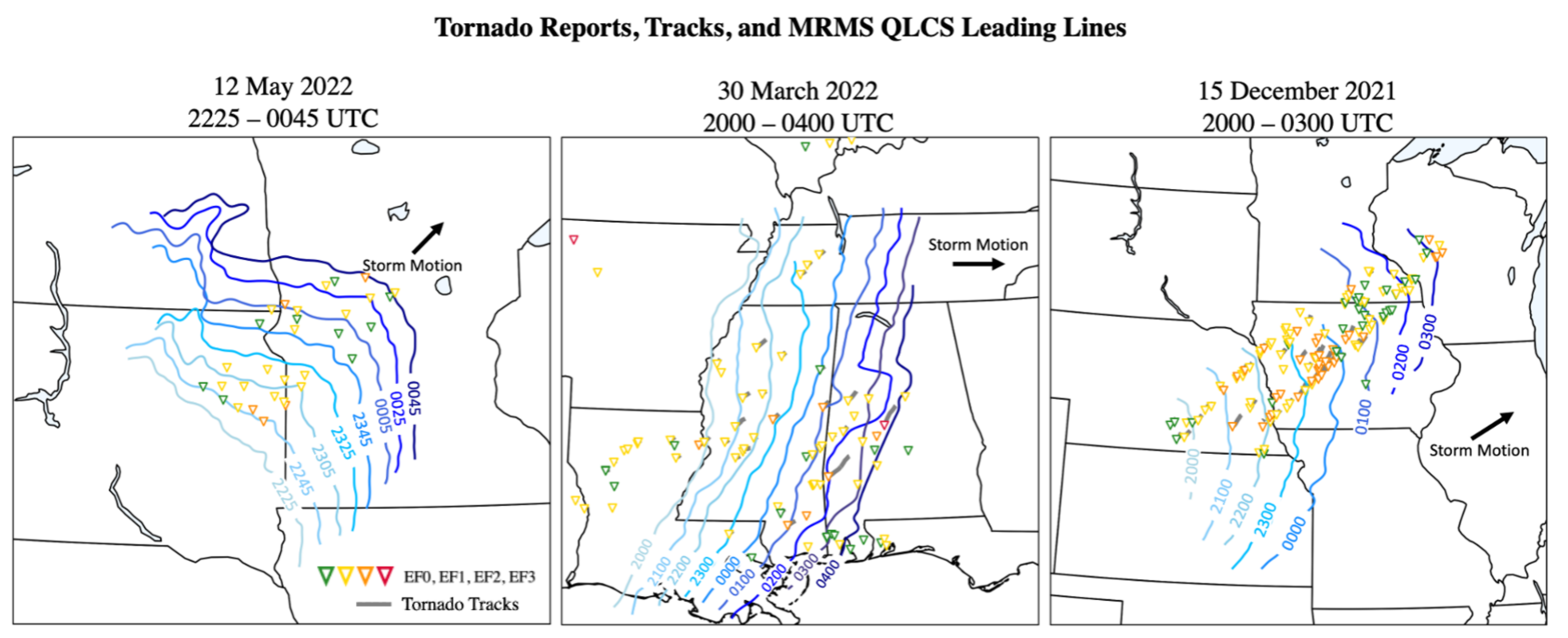

Figure 3.1: Overview of the 12 May 2022 (left), 30 March 2022 (middle), and 15 December 2021 (right) QLCS case studies showing the MRMS leading line with time and the tornado reports. Tornado icons represent the starting point for each tornado tracks (in gray) and are color-coded to represent the finalized EF-scale rating.

Table 3.1: Object identification and QLCS classification thresholds for the three case studies. The first number for each of the WoFS reflectivity thresholds corresponds to the threshold for the analysis (or 0-min forecast), and the second number is the threshold for all other subsequent forecast times (5–360-min, in 5-min increments).

Case	**Min. Reflectivity (dBZ)**	**Max Reflectivity (dBZ)**	**Min. Area (grid cells)**	**Merge Distance (grid cells)**
12 May 2022 WoFS	40/45	45/50	6	4
30 March 2022 WoFS	40/47	45/52	45	2
15 December 2021 WoFS	39/44	44/49	25	2
12 May 2022 MRMS	40	45	6	4
30 March 2022 MRMS	40	45	45	2
15 December 2021 MRMS	39	44	25	2

lower reflectivity values than the rest of the forecast, but as forecast time increases so do the reflectivity values (recall Fig. 2.9b). See Table 3.2 for the exact WoFS initialization times and forecast times analyzed for these cases. The initialization and forecast times are chosen based on the convection initiation and longevity of the QLCS. The second change concerns the merge orientation threshold in the second pass of the algorithm's two-pass process. For the 12 May 2022 case, the threshold was changed from 30° to 90° to account for the QLCS having segments that are vastly different in orientations (Fig. 3.1). The orientation threshold was decreased back to 30° for the two remaining cases.

Once all possible QLCS objects were identified in both MRMS and the WoFS forecasts, they then go through a process called object isolation. Object isolation is a semi-manual, subjective process where only the QLCS object(s) associated with the case study are kept and all other objects are removed. This is also the last step in which multiple objects belonging to the same QLCS can be merged together. The isolation process results in only one object per MRMS 5-min output or per WoFS ensemble member for every 5-min output.

Table 3.2: The initialization and forecast times that are analyzed for each of the QLCS case studies. Forecast times are in 5-min increments.

WoFS Case	**WoFS Initializations (UTC)**	**Forecast Times (min)**
12 May 2022	20, 21, 22, 23	20 UTC: 0–360 21 UTC: 0–340 22 UTC: 0–200 23 UTC: 0–150
30 March 2022	20, 21, 22, 23	20 UTC: 0–360 21 UTC: 0–360 22 UTC: 0–360 23 UTC: 0–360
15 December 2021	22, 23	22 UTC: 0–360 23 UTC: 0–260

3.1.3 QLCS Leading Line Identification

Similarly to the QLCS centerlines, QLCS leading lines are used to analyze the more specific errors associated with the leading edge of the QLCS. The process of isolating the QLCS's leading line starts with finding the direction of storm motion, as this will determine the direction that the leading line is facing. For the 12 May 2022 and 15 December 2021 cases, the storm motion was to the northeast, while the 30 March 2022 was to the east.

The 12 May QLCS has a more complex structure than the other two cases, with the QLCS being made up of two segments with different orientations (the northern segment is facing north, while the southern segment is facing east). Therefore, the methods for isolating the leading edge of this QLCS differs from that of the other two cases. First, the eastern-most points of this QLCS are identified by looping through each of the 1–300 indices along the y-direction (north-south) of the WoFS domain, and finding the points contained within the QLCS object for each index. Only the eastern-most point for each index is kept, as those points will make up the leading edge of the QLCS. Next, the northern-most points are identified by looping through the 1–300 indices of the WoFS domain, but this time along the x-direction (east-west). For each index, the northern-most point is kept.

The two arrays of points (one for the eastern points and the other for the northern points) are then quality controlled (QC'ed) to remove any points that do not lie on the leading edge of the QLCS. The QC is performed by first identifying the centerlines for each of the QLCS objects, using the same methods as outlined in Section 3.1. The centerline serves as a reference line for filtering out the points that do not exist on the leading edge of the QLCS. To filter the points, a KDTree nearest-neighbor approach finds the point on the centerline that is the closest to each of the leading line points. Using that closest centerline point as a reference point, a vector is created between the centerline point and the leading line point. For the eastern point array, the vector needed to be in either the first (0–90°) or fourth quadrant (270–360°) for the leading line point to be kept. If it was in the second (90–180°) or third quadrant (180–270°), the point would essentially be to the west of the centerline. Therefore, the point would not be on the leading edge, so that point would then be removed from the array. The same method is used for the array of northern points. In this case, if the vector between the closest centerline point and the leading line point was in the third or fourth quadrant, then it was removed. Only the northern points with vectors in the first or second quadrants are kept.

After the points are QC'ed, the two arrays are combined and re-sorted. A KDTree nearest-neighbor method is used to sort the points with a defined start and end point. The starting point is defined as the first point in the QC'ed northern array (northwestern-most point), and the end point is the first point in the eastern array (southeastern-most point). The KDTree begins with the start point and finds the closest leading line point in the array to it. The loop then finds the next closest point to the previous point until the loop reaches the defined end point. This method sorts the points from the northwest corner of the domain to the southeast corner. The sort is also reversed to mitigate some of the rare errors that can occur when defining the leading line, such as loops and the line crossing over itself. In that case, the KDTree sort starts with the first point in the eastern array and ends with the first point in the northern array. Thereby, sorting the points from the southeast corner of the WoFS domain to the northwest corner.

After sorting the combined array of northern and eastern points, the two lines (the original and reversed) are compared to find the optimal leading line. First, the lines are defined as simple (not crossing itself) or complex (crossing itself). If one of the lines is complex, then the simple one is kept as the resulting leading line. If both lines are simple, then the one with the longest length is kept. If both are complex, then the line with the shortest length is deemed the leading line. The resulting optimal leading line is smoothed with a 2D Gaussian filter (radius=2) and saved.

The leading line process for the March and December case studies is simplified as their lines gradually change in orientation, unlike the May case that has an almost 90° change between segments (Fig. 3.1). In these cases, only the eastern-most points are found by looping through the 1–300 indices in the y-direction. Those points are then QC'ed using their centerlines as a reference line just like in the May case. The points are re-sorted using the first point of the array as the starting point and the last point as the defined end point for the KDTree. The optimal line is identified, smoothed, and saved using the same processes outlined above for the May case.

3.1.3.1 Leading Line Shear Analysis

The goal of part II of this project is to investigate the potential of using upstream shear information and line geometry to forecast the tornado potential of mesovortices. To get an accurate representation of the LP and LN shear, they need to be calculated relative to the leading line's orientation. To calculate the line-relative LP and LN shear, we must first calculate the local orientation of the leading line at each point. The process of finding local orientation starts by looping through all the leading line points. For each point, we take two points before and after and use those endpoints to find the orientation, which is given in degrees counterclockwise from East (0°). The next step is to carve out the sector upstream of the QLCS that will be used to pull the WoFS shear data from. To the author's knowledge, there have yet to be any QLCS studies that identify the distance ahead of the QLCS that would capture the inflow environment. However, there have been many studies analyzing inflow environments of supercells that define the near-field environment as the first 0–40-km from the storm (Parker 2014; Coffer et al. 2017; Flournoy et al. 2020; Britt et al. 2020). Under the assumption that the near-field environment distance for supercells and QLCSs is similar, we decided to carve out a shear sector by projecting the leading line forward 40 km and normal to each point's local orientation. In other words, for each of the leading line points, we calculate a point that is 40 km away and perpendicular to the local orientation at that point. Once this is done for each of the leading line points, it will form a new line that will be referred to as the projection line (Fig. 3.2b). The equations to calculate each of the projection line points are as follows:

$$\theta_{\perp} = \theta_{local} \pm 90^{\circ} \tag{3.1}$$

$$x_{proj} = x_{LL} + dist * cos(\theta_{\perp}) \tag{3.2}$$

$$y_{proj} = y_{LL} + dist * sin(\theta_{\perp}), \tag{3.3}$$

where $\theta_{\perp}$ is the angle normal to the local orientation of the leading line point (θ_{local}), x_{proj} and y_{proj} are the x- and y-components of the new point on the projection line, x_{LL} and y_{LL} is the x- and y-component of the leading line point, and $dist$ is 40 km. Note that in Eq. 3.1 the angle normal to the local orientation is calculated either by adding or subtracting 90°.

To ensure the projection point is in front of the leading line and not behind, we have to QC each projection point. This is done by creating a QC polygon made up of the leading line and two other lines that trace each of the leading line's endpoints to the origin (southwest corner) of the domain (Fig. 3.2a). This creates a conic-like polygon that encases the space behind the leading line (Fig. 3.2a). The Shapely Python package is used to check if each projection point is contained within the QC polygon. If the projection point is in the QC polygon, then the x- and y-components of the projection point are recalculated using the complement angle to $\theta_{\perp}$. In other words, if the first projection point was calculated by subtracting 90° from the local orientation angle, then the next point will be calculated by adding 90° to the local orientation angle. If the new projection point is still contained within the QC polygon, then the x- and y-components of that point are set to np.nans, and are filtered out later. Once we find the projection point that is not contained within the QC polygon, we save it and move on to the next point.

Once the projection line is identified (Fig. 3.2b), both it and the leading line are converted to Shapely LineStrings, then converted to a Shapely Polygon (Fig. 3.2c). A buffer is added to the projection line to smooth out any kinks, holes, or overlaps (Fig. 3.2b). The resulting polygon represents the inflow environment of the QLCS (Fig. 3.2c), and is where the shear information will be pulled from. First, we identify each of the WoFS domain indices/gridboxes that are contained within the shear polygon. Once identified, each of the gridboxes is matched with the closest point on the leading line by using a KDTree nearest-neighbor approach. This allows for the calculation of the line-relative LP and LN shear using the local orientation angle at each leading line point. The 0–1-km and 0–3-km LP and LN shear are calculated as follows:

$$LL_{vector} = [cos(\theta_{rad}), sin(\theta_{rad}), 0], \tag{3.4}$$

where the LL_{vector} is the leading line vector, and θ_{rad} is the local orientation angle in radians at each leading line point. The shear magnitude is calculated by:

$$Shear_{mag} = \sqrt{u_{shear}^2 + v_{shear}^2}, \tag{3.5}$$

where u_{shear} and v_{shear} are the u- and v-components of the shear either for the 0–1-km or 0–3-km level. The shear magnitude is used to normalize the components of the shear vector (for simplicity):

$$Shear_{vector,normalized} = [\frac{u_{shear}}{Shear_{mag}}, \frac{v_{shear}}{Shear_{mag}}, 0]. \tag{3.6}$$

To find the percentage of the shear that is parallel to the local orientation of the leading line, we take the absolute value of the dot product between the leading line vector and the normalized shear vector:

$$LP_{\%} = |LL_{vector} \cdot Shear_{vector,normalized}| * 100\%, \tag{3.7}$$

where $LP_{\%}$ is the percentage of the total shear magnitude that is LP. The magnitude of the LP shear is then calculated by taking the total shear multiplied by the percentage of LP shear. The magnitude of LN shear is calculated by first subtracting the LP percentage by one to find the percentage of LN shear, then multiplying that by the shear magnitude.

The LN and LP shear is calculated for each of the gridboxes contained within the shear polygon. All gridboxes are matched to the closest point along the leading line using a KDTree nearest-neighbor approach. The LP and LN shear is calculated for each of the gridboxes, using the local orientation of the matched leading line point. Finally, the amount of LP and LN shear for each leading line point is calculated by averaging the shear over all matched boxes for that specific point.

3.1.3.2 Local Tortuosity

Local tortuosity (see Section 2.1.5) at every leading line point is also calculated to identify localized bowing structures. The local tortuosity at each leading line point is calculated similarly to the local orientation, except we take six points on either side of the point. The tortuosity equation (Eq. 2.6) becomes:

$$\text{Tortuosity}_{\text{local}} = \frac{L_{segment}}{L_e}, \tag{3.8}$$

where $L_{segment}$ is the length of the leading line segment calculated by summing the distance between the points that make up the segment. L_e is the length of the endpoint line, which is calculated by finding the distance between the first and last points of the segment.

3.1.4 QLCS Mesovortex Tornado Parameter (QTor)

A new parameter, known as QTor, is created to characterize the potential for mesovortex tornadoes in any given QLCS. This parameter takes into account the magnitudes of LP and LN shear, as well as the local geometry of the leading line to highlight locations that are the most favorable for mesovortex tornadoes. Values of QTor greater than one indicate areas that meet the base criteria for mesovortex tornadoes to occur. The higher the number, the more favorable the location for producing mesovortex tornadoes. QTor is calculated as follows:

$$\text{QTor} = \frac{LN_{0-3}}{15.0\text{m s}^{-1}} * \frac{LP_{0-1}}{7.0\text{m s}^{-1}} * \text{Tortuosity}_{\text{local}}, \tag{3.9}$$

where LN_{0-3} is the magnitude of the 0–3-km LN shear and LP_{0-1} is the magnitude of the 0–1-km LP shear relative to the leading line. The 15.0 m s^{-1} threshold for LN shear is from the 3IM (Schaumann and Przybylinksi 2012; Gibbs 2021), while the LP threshold of 7.0 m s^{-1} is from the recent work of Brown et al. (2024). The last term is the local tortuosity, which represents the curvature of the leading line segment. Local tortuosity is used to identify the presence of a surge or bow in the leading line, which is one of the ingredients of the 3IM (Schaumann and Przybylinksi 2012; Gibbs 2021). Typically, this ingredient is subjective, in which the forecaster must analyze the leading line for any kinks, bows, or local surges that would indicate a higher potential for mesovortex tornadogenesis.

However, local tortuosity allows for a more objective way of locating areas of the line that have increased curvature.

The goal of QTor is to bring the ingredients of the 3IM into a more objective framework and to account for more recent work suggesting LP shear magnitude also plays a role in the tornado potential of mesovortices (Brown et al. 2024). This parameter can also be incorporated into convective-scale models to locate the areas most favorable for mesovortex tornadoes, which the 3IM cannot.

3.1.5 Neighborhood Methods

Probabilistic guidance products are usually not presented at the grid scale, as small displacement errors may reduce the usefulness of the forecasts (Schwartz and Sobash 2017; Roberts et al. 2019; Skinner et al. 2023). Therefore, neighborhood approaches are used to spread and smooth the ensemble forecasts of shear and QTor for this study. A square neighborhood with a radius of 13.5 km (27-km diameter) surrounds the gridbox, and is then used to replace the value of each gridbox with the maximum value from the neighborhood. The resulting field is then smoothed using a convolution kernel (radius=4). The current real-time WoFS guidance employs neighborhoods of radii of 13.5, 7.5, and 4.5 km, as these provide probabilities of hazards of individual thunderstorms over an area that is roughly the size of a typical NWS warning (Skinner et al. 2023). The 13.5-km neighborhood is chosen for this study as the others were too small to visualize the shear and QTor data.

3.1.5.1 Percentiles and Ensemble Probability of Exceedance

Percentile products are typically used in WoFS to represent the severity of the forecasted event, with the 90th and maximum percentiles shown on the WoFS online viewer and the maximum representing the worst-case scenario (Skinner et al. 2023). However, for the purposes of this study, only the 75th percentile is used, as this represents a “middle-ground” between the 50th and 90th percentiles for describing the severity of each parameter. The 75th percentile is calculated after the neighborhood is applied and smoothed.

Ensemble probability of exceedance methods will also be used to describe the likelihood of QTor exceeding a specific threshold (2.50[1] is used in this study), by calculating the ensemble probability density function at each gridpoint within the ensemble domain (after the neighborhood and smoothing). Since the probability is based on how many ensemble members have forecasted the parameter above a specified threshold, these products can also be viewed as metrics for ensemble member agreement. The higher the probability, the more the ensemble members agree that the parameter will reach the specified threshold, and vice-versa.

3.1.6 Verification Dataset

Tornado tracks are used as a source of verification for the WoFS QTor forecasts. For each case study, the tornado tracks are extracted from the NOAA/NWS Damage Assessment Toolkit (DAT; NOAA 2024). The start and end points for each of the tornadoes are collected from the SPC's tornado database (SPC 2023). Due to many of the tornado tracks being quite small, only the start point of each tornado track is plotted for all figures.

Additionally, the upstream 0–1-km and 0–3-km shear vectors are estimated from the WoFS forecasts or soundings (when available) to add extra clarification when interpreting the magnitudes of LN and LP shear along the leading lines. If not available in WoFS, the vectors are estimated using the closest sounding taken the day of the event from the SPC's severe event database. Note that only the soundings upstream of the event are considered, as they are not contaminated by convection.

---

[1] This value was chosen as it best represents the areas that are most favorable for mesovortex tornadoes.

3.2 Results

3.2.1 12 May 2022

3.2.1.1 Case Overview

On 12 May 2022, the SPC forecasted a moderate risk for severe convection spanning from northern NE to southern ND and eastern MN, at 2000 UTC (Fig. 3.3). The main threats for this day included severe winds (45% hatched area from NE to MN; not shown), tornadoes (10% hatched area for the northeast corner of SD, extending into southeast ND and west-central MN; not shown), and hail (30% hatched area over northeast SD; not shown).

The 12 May 2022 QLCS initiated along a cold front around 1500 UTC in the southwestern corner of KS. The convection began as disorganized cells that rapidly grew upscale, becoming quasi-linear in southern NE around 1830 UTC. The QLCS moved northeast at speeds of approximately 50-70 mph (Aberdeen 2022). By 2200 UTC, the QLCS had taken on the structure of a classic leading-line, trailing-stratiform system. It did not dissipate until it reached east-central MN around 0200 UTC. This QLCS, also classified as a derecho (Johns and Hirt 1987), was categorized as a billion-dollar event due to significant damage from straight-line winds (measuring between 60–100 mph; Aberdeen 2022) and 34 confirmed tornadoes, which primarily occurred in northeast SD and west-central MN (Fig. 3.3). Most of the tornadoes were rated EF0–EF1 (Fig. 3.1), but there were five EF2 tornadoes in eastern SD and western/central MN that caused extensive damage (Aberdeen 2022; Fig. 3.1).

This case was chosen for this study because it was a high-impact derecho event that produced significant straight-line winds and tornadoes, indicative of embedded mesovortices. Additionally, it occurred during the warm season, which is relevant for understanding how seasonality may affect the QTor forecasts. The QLCS exhibited two distinct orientations of its leading line (Fig. 3.1): a northern segment with a primarily east-west orientation and a southern segment with a north-south orientation. The presence of these two different orientations within on QLCS allows for the comparative analysis of LN and LP shear relative to the leading line orientation and its potential effect on mesovortex development.

3.2.1.2 Shear Analysis and QTor Forecasts

The WoFS forecasts from 2000–2300 UTC are analyzed for the 12 May 2022 QLCS case study (Table 3.2) to examine the 0–3-km LN shear, the 0–1-km LP shear, and tortuosity fields, and how they influence the QTor forecasts.

Beginning with the 2000 UTC WoFS forecast, there is an increase in LP shear from approximately 13 m s^{-1} to 18–20 m s^{-1} in the location where this QLCS starts to produce tornadoes (Fig. 3.4a). 0–3-km LN shear also increases in this area, but is slightly delayed (Fig. 3.4b). This same location also contains a couple pockets of tortuosity greater than 1.15 (Fig. 3.4c), indicative of the leading lines increasing in curvature. This increase in curvature is attributable to the leading lines surging or bowing outward. Since the 0–1-km shear vector upstream of the QLCS points to the north with a very slight westward component (Fig. 3.4a), as the lines bow outward they become more aligned with the shear vector, consistent with the increase in LP shear (Fig. 3.4a). Similarly, around the time that the LN shear starts to increase just after the first few tornado reports (at approximately 2330 UTC), the leading lines take the shape of a boomerang. The two sides of the boomerang are oriented more perpendicular to the 0–3-km shear vector (pointing northeast; Fig 3.4b), thus increasing the LN shear in these areas. Both the LP and LN shear magnitudes exceed the thresholds set by the QTor equation (Eq. 3.9), which corresponds to the northern swath of QTor values between 1–2 that encompasses the region of tornado reports observed with this QLCS (Fig. 3.4d). While the northern QTor swath does miss a few of the first tornadoes (Fig. 3.11d), it does capture the area of interest for mesovortex tornadoes with a lead time of more than 3 hrs.

There is a secondary swath of high (approximately 3–4) QTor values to the south that is not collocated with any tornado reports for this QLCS (Fig. 3.4d). The main contributing factor of this southern swath can be diagnosed by examining the leading lines for WoFS and MRMS at 2330 UTC (Figs. 3.5a,c) and 0030 UTC (Figs. 3.5b,d). At 2330 and 0030 UTC, the WoFS leading lines have a much different orientation compared to the MRMS leading line, both for the southern and northern segments (Fig. 3.5). These differences in orientation are associated with a maximum of 0–1-km LP and 0–3-km LN shear on the southern side of the QLCS (Fig. 3.5a,c), corresponding with the southern QTor swath (Fig. 3.4d). However, the magnitudes for the LN shear are higher than those associated with LP shear in the area of the southern swath, meaning that LN shear is the main contributing factor to the southern swath in the QTor forecasts. Additionally, while only the 2000 UTC forecast is shown in Fig. 3.5, these differences in orientation persist for all forecasts.

Overall, when the orientation of the leading line changes, the magnitudes of the LN and LP shear will also change. This is unsurprising as the LP and LN shear are calculated relative to the orientation of the leading line. The orientation differences between the forecasted and observed QLCSs were also discovered in the centerlines from Part I of this study (Section 2.2.3), in which the orientation of the WoFS centerlines typically increased counter-clockwise with increasing forecast time. Therefore, the orientation differences can be viewed as a source of forecast error that impacts the magnitudes of LP and LN shear, as well as the QTor forecasts.

The 2100 UTC swaths for 0–1-km LP shear (Fig. 3.6a), 0–3-km LN shear (Fig. 3.6b), tortuosity (Fig. 3.6c), and QTor (Fig. 3.6d) are similar to those from the previous forecast (Fig. 3.4). Overall, the swaths maintain the same shape, but the magnitudes of the parameters have increased slightly, particularly in the northern swath that encompasses the tornado reports (Fig. 3.6). The magnitudes of LP shear are similar to those in the previous forecast, but the areas of LP shear greater than 20.5 m s^{-1} have increased ((Fig. 3.6a). On the other hand, the magnitudes of LN shear have increased compared to the previous forecast, especially in the area containing the tornado reports (Fig. 3.4b). Also, the area of LN shear magnitudes from 20–25 m s^{-1} is larger than that of the 2000 UTC forecast (Fig. 3.6b). The LN shear increases earlier and contains more of the tornado reports than the 2000 UTC forecast (Fig. 3.6). Tortuosity also increases in magnitude, albeit slightly compared to the 2000 UTC forecast and in a much smaller area near the first line of tornado reports (Fig. 3.6c). The increase in tortuosity near the first line of tornado reports occurs around 2235 UTC when the WoFS leading lines appear to surge outward and form local bowing segments (not shown). The increases in LP and LN shear magnitudes, and tortuosity (to a lesser degree) causes the QTor magnitudes to also increase (Fig. 3.6d), resulting in a larger area of QTor values over 3 compared to the previous forecast. While the increase in tortuosity does not affect the QTor swath as much as the increasing magnitudes of LP and LN shear do, it is still indicating that the lines are bowing outward, thereby increasing the potential for mesovortex tornadoes.

For the 2200 UTC forecast, the area covered by the swaths for all parameters have decreased because the event's lead time decreases with subsequent forecasts and a shorter period is used (Fig. 3.7). The main differences between the 2100 and 2200 UTC forecasts are the magnitudes of LP shear (Fig. 3.7a), LN shear (Fig. 3.7b), tortuosity (Fig. 3.7c), and QTor (Fig. 3.7d), particularly in the northern swath that envelopes the tornado reports. All parameters have increased in magnitude for this forecast and the areas with the highest magnitudes for each parameter have also increased in size compared to the previous forecast. Thus, the magnitudes of shear, tortuosity, and QTor all increase with subsequent forecasts to include more of the tornado reports (Fig. 3.7) compared to the previous forecasts.

Similarly to the 2200 UTC forecast, the 2300 UTC swaths maintain the same shape and size, but the magnitudes of the variables have again increased (Fig. 3.8). Plus, the areas of these increased values have also grown larger. For example, the swath of LP shear (Fig. 3.8a) contains more areas with shear values greater than 20.5 m s^{-1}. The same is true for the LN shear swath, in which the area of shear greater than 23 m s^{-1} is larger and includes more of the tornado reports than then 2000–2200 UTC forecasts (Fig. 3.8b), with the exception of the first line of tornado reports as they formed before the 2300 UTC forecast. The tortuosity swath also has more areas where it exceeds 1.15 (Fig. 3.8c), indicating an overall increase in curvature of the leading lines for this forecast. The magnitude increases for all parameters consequently creates an area of QTor values between 3–4, which is also more expansive than the other forecasts (Fig. 3.8d).

Overall, the mesovortex tornado potential for the 12 May 2022 QLCS was well forecasted. The first QTor forecast at 2000 UTC is essentially a 3-hr forecast that highlights the area most favorable for mesovortex tornadoes, consistent with the location of the tornado reports for this event (Fig. 3.4d). As forecast lead time for this event decreases with subsequent forecasts, the northern swath of QTor remains in the same general location but is refined and expanded to cover more of the tornado reports as the event approaches (Figs. 3.6d, 3.7d, and 3.8d). However, one issue with the forecasts from this day is the presence of the the southern swath of QTor that is not collocated with any tornado reports. The forecast error associated with the different orientations of the WoFS leading lines compared to the MRMS leading line observed in Fig. 3.5 is present for all forecasts. Therefore, the orientation differences in the southern portion of the QLCS may be responsible for the southern swath of QTor, especially the LN shear, which appears to affect the magnitudes in the southern swath the most. Consequently, the southern swath of QTor is considered a false alarm.

One way to identify areas of QTor that may be considered false alarms, is by examining the ensemble probability of exceedance swaths (Fig. 3.9). While the percentile swaths show the measure of severity for the event, the ensemble probabilities show the likelihood of the event and the agreement between ensemble members (Skinner et al. 2023). The ensemble probabilities that QTor will exceed 2.50 are highest in the northern QTor swath than the southern for all forecasts (Fig. 3.9). Higher probabilities in the northern QTor swath indicates more agreement between ensemble members and that this area will be favorable for mesovortex tornadogenesis (Fig. 3.9). On the other hand, the probabilities of exceedance are lower in the southern QTor swath, meaning there is more ensemble spread and uncertainty for this area. Examining the ensemble probability of exceedance in conjunction with percentile products helps to provide a fuller picture of what is happening in the QTor forecasts. For example, even though the southern swath of QTor had higher values[2] (sometimes greater than 4; Figs. 3.4d, 3.6d, 3.7d, and 3.8d) compared to the northern swath (maximum values slightly above 3), the northern swath has a consistently higher probability than the southern swath (Fig. 3.9). While this is not a perfect metric for QTor false alarms, these swaths can act to increase forecasters' confidence in the northern swath having a higher chance for mesovortex tornadoes compared to the southern swath (Fig. 3.9).

3.2.2 30 March 2022

3.2.2.1 Case Overview

On 30 March 2022, the SPC issued a moderate risk for severe weather for parts of eastern LA, all of MS, and western AL (Fig. 3.10). The main threats included severe winds and tornadoes, with a 45% and 15% hatched areas over all of MS and western AL, respectively (not shown). The QLCS initiated along a dryline in southwest OK and northern TX at approximately 0030 UTC on 30 March. The quasi-linear line of convection moved through central OK and TX, until it became disorganized around 0800 UTC. The convection continued eastward until the line reorganized in AR and LA around 1700 UTC. The orientation of this QLCS was almost purely meridional, with the convective line extending from southern LA to parts of central IL and IN. The QLCS continued eastward until it began to dissipate in GA at approximately 1700 UTC on 31 March 2022.

---

[2] The swaths shown herein are an ensemble 75th percentile product, so higher values may not necessarily correspond with actual higher values in the members. This may also reflect reduced ensemble spread.

As the QLCS tracked through LA, MS, and AL, it produced numerous severe wind and tornado reports (Figs. 3.10 and 3.1). In total, there were approximately 114 tornado reports and 318 wind reports (Fig. 3.10). Most of the tornadoes occurred in LA, MS, and western AL, predominately rated as EF0 or EF1, with a few stronger tornadoes rated as either EF2 or EF3 (Fig. 3.1).

The QLCS that occurred on 30 March 2022 was chosen for this study for several reasons: 1) it exhibited a leading-stratiform, trailing-leading line structure, 2) it developed in a low-CAPE, high-shear environment typical of the southeastern US, 3) it is considered as a cold-season case (as March is considered part of the cold season, even though this case is on the cusp of March and April), and 4) this case was part of the Propagation, Evolution, and Rotation of Linear Storms (PERiLS; Kosiba and Coauthors 2024) field experiment.

3.2.2.2 Shear Analysis and QTor Forecasts

The 2000 UTC forecast shows a large area of LP shear greater than 25 m s^{-1} (Fig. 3.11a), consistent with the 0–1-km shear vector being largely parallel to the QLCS's convective line. This QLCS occurs in the southeast US, therefore, it is unsurprising that the LP shear dominates this case. The southeast US is characterized as a high-shear, low-CAPE environment, and these environments are known for having more LP shear (Sherburn and Parker 2014; Sherburn et al. 2016; King et al. 2017; Chasteen and Koch 2022). Since the 0–1-km shear vector is parallel to the convective line for this case, the LN shear will be of the main importance to tornado potential as the QLCS segments reorient and bow outward with time (Lovell and Parker 2022). Consequently, many of the tornado reports for this storm are collocated with pockets of enhanced LN shear (Fig. 3.11b). Tortuosity also increases in these areas (Fig. 3.11c), consistent with bowing structures that would increase the LN shear where the sides of the bow are perpendicular to the shear vector. Since the LP shear field exceeds the threshold set by Brown et al. (2024) everywhere, it is unsurprising that the QTor swath (Fig. 3.11d) looks similar to the LN shear swath (Fig. 3.11b). While some of the tornado reports are collocated with a maximum in QTor, the swath still misses a lot of the tornadoes, especially the ones in TN, southern MS, far-eastern MS, and western AL (Fig. 3.11d). Note that the tornado reports in northern LA are included for sake of completeness, but will not be included in the analysis as they occurred before the 2000 UTC forecast.

The 2100 UTC forecast for all parameters (Fig. 3.12) is very similar to the 2000 UTC forecast. Again, the LP shear exceeds the 7.0 m s^{-1} threshold everywhere in the swath (Fig. 3.12a), so the focus is mainly on the LN shear field (Fig. 3.12b). Similarly to the LN shear swath at 2000 UTC, most of the tornado reports are associated with the swaths of LN shear greater than 8 m s^{-1} (Fig. 3.12b). Tortuosity continues to mimic the LN shear field, as more curvature tends to also increase LN shear (Fig. 3.12c). However, there are a few locations with higher tortuosity values (greater than 1.15) compared to the previous forecast, particularly in the location of the tornado reports along the central MS/AL border (Fig. 3.12c). Due to the swath of increased LN shear and tortuosity along the MS/AL border, a southern swath of QTor has developed to cover a lot of the tornado reports in that area (Fig. 3.12d). At the time of this forecast, the swath of QTor values along the MS/AL border is a 4-hr forecast. While the QTor forecast does miss some of the tornadoes in TN and southern MS and AL, it does highlight the areas in northern MS and along the MS/AL border that contained many tornado reports (Fig. 3.12d).

For the 2200 UTC forecast, the areas of LP shear greater than 30 m s^{-1} have increased in area (Fig. 3.13a), compared to the same areas in the 2100 and 2000 UTC forecasts. The majority of tornado reports at this time are located in or near areas of LP shear greater than 30 m s^{-1}(Fig. 3.13a). Similarly, the tornado reports in northern MS and TN, as well as along the MS/AL border are collocated with swaths of 0–3-km LN shear greater than 8 m s^{-1} (Fig. 3.13b). The southern swath of LN shear is also collocated with a swath of increased tortuosity, meaning the leading lines are bowing outward in that area (Fig. 3.13c), consistent with the increase in LN shear in the same area (Fig. 3.13b). For QTor, the northern swath has grown to include the tornadoes that occurred in TN (Fig. 3.13d), and still encompasses the reports in northern MS (with the exception of the central MS reports as these occurred before this forecast). The southern QTor swath for this forecast has become more cohesive and includes more of the tornadoes concentrated along the MS/AL border (Fig. 3.13d) than the previous forecasts. This area had several EF1 and EF2 tornadoes, which are collocated with two maximas in QTor (Fig. 3.13d). However, there is an area of QTor values between 5.5–7 in TN that would be considered a false alarm.

Similarly to the 2000–2200 UTC forecasts, the 2300 UTC forecast of 0–1-km LP shear has magnitudes greater than 30 m s^{-1} for much of the forecast area that are also collocated with tornado reports (Fig. 3.14a). The steady increase in LP shear greater than 30 m s^{-1} may be associated with the development of the low-level jet (LLJ), which acts to intensify the shear, especially at later forecast times. Most of the tornadoes that occurred during this forecast are associated with areas of LN shear greater than 8 m s^{-1}. However, the tornadoes in TN and along the MS/AL border are associated with LN shear greater than 18 m s^{-1} (Fig. 3.14b). Some amount of tortuosity is associated with almost all tornado reports, especially the EF1 tornadoes in TN and along the central MS/AL border (Fig. 3.14c). QTor has the highest values in the vicinity of the TN tornadoes and the tornadoes that occurred along the MS/AL border (Fig. 3.14d). However, due to low values of LN shear and tortuosity, QTor also has lower values in central AL, even though a few tornadoes did form in that area (Fig. 3.14d).

The 2300 UTC forecast also shows an important limitation of QTor: the values of QTor do not scale with the intensity of the mesovortices produced. For instance, two of the tornadoes in central AL were rated EF2 and EF3 and are collocated with small QTor values between 2.5–3 (Fig. 3.14d), while weaker tornadoes may be associated with higher QTor values. Therefore, QTor offers no information about the intensity of the mesovortices and/or tornadoes that can form with these systems. Some tornadoes may be weak but associated with higher QTor values than stronger tornadoes (Fig. 3.14d). QTor simply highlights the locations most favorable for the development of mesovortices, not the intensity of the rotation associated with them.

One notable aspect of the QTor forecasts, evident across the 2100–2300 UTC forecasts, is their ability to accurately forecast high values corresponding to the tornadoes that formed along the MS/AL border. With the exception of the 2000 UTC forecast, all subsequent forecasts depicted a QTor signature overlapping the tornadoes in that region (Figs. 3.12d, 3.13d, and 3.14d). The presence of high values of LN shear and tortuosity in this area suggests the leading lines were bowing outward, increasing in curvature and thereby enhancing the LN shear. Analysis of the WoFS and MRMS leading lines around the time these tornadoes developed aligns consistently with the LN and tortuosity values during this period (Fig. 3.15). At 0105 UTC, the WoFS leading lines begin to exhibit slight bowing, which corresponds to the increase in the LN shear and QTor for that QLCS segment (Fig. 3.15a,c). The bowing intensifies around 0115 UTC, concurrent with the increase in LN shear (Fig. 3.15b), tortuosity (not shown), and QTor (Fig. 3.15d) at the same time. While only the 2300 UTC forecast is depicted (Fig. 3.15), similar increases in tortuosity (not shown), LN shear, and QTor were observed in the 2100 and 2200 UTC forecasts (not shown) as well.

Similar to the 12 May case study, the ensemble probability of QTor exceeding 2.50 helps to understand the likelihood of the event (Fig. 3.16). The 2000 UTC forecast has the highest ensemble probabilities associated with the tornadoes that occurred in western/central MS and in TN (Fig. 3.16a). For the 2100 UTC ensemble probabilities (Fig. 3.16b), there is still a swath of probabilities greater than 0.8 in northern MS as in the 2000 UTC forecast. Additionally, the probabilities associated with the southern QTor swath have started to increase near the tornadoes that developed in east-central MS and west-central AL (Fig. 3.16b). The main swath of maximum probabilities for the 2200 UTC forecast still appears in the same place as the previous forecasts (Fig. 3.16c). However, a secondary swath of probabilities between 0.5–0.7 starts to cover the area of MS and AL that has a cluster of tornado reports (Fig. 3.16). This southerly swath remains in the 2300 UTC forecast, but has increased in probability (Fig. 3.16) and encompasses a majority of the tornado reports in MS and AL. Overall, the QTor probability swaths improve in location with subsequent forecast times. In other words, as the lead time for the event decreases, the QTor swaths tend to perform better. While the swaths do get better with time, QTor still misses some tornado reports consistently over all four forecasts, particularly the ones in southern MS and AL (Fig. 3.16). In fact, the tornadoes in southern MS and AL are never captured by any of the QTor forecasts (Figs. 3.11d, 3.12d, 3.13d, and 3.14d). One reason these tornadoes were missed is that they are most likely associated with supercells that formed on the southern end of this QLCS. In the future, any reports associated with supercells will be filtered out.

3.2.3 15 December 2021

3.2.3.1 Case Overview

On 15 December 2021, the SPC issued a moderate risk for severe weather across most of Iowa, and parts of NE, MN, and WI (Fig. 3.17). The primary hazards for this day included severe winds and tornadoes, with respective 10% hatched and 45% hatched probabilities over the moderate risk area (not shown). This marked the first time a moderate risk was issued for Iowa in December (Des Moines 2021). The 15 December 2021 QLCS initiated along a dryline in west-central KS around 1800 UTC and tracked northeast through parts of KS, NE, MN, MO, and eventually covering the entire state of IA. The QLCS dissipated in WI around 0430 UTC on 16 December 2021.

This event was historic for IA and the US, as the QLCS produced 63 confirmed tornadoes in IA alone, with 21 of those rated as EF2 (Fig. 3.1). This broke the IA state record for the most tornadoes in a single day (previously 35 tornadoes on 31 August 2014;

Des Moines 2021). Additionally, this QLCS set a new record for the most EF2-rated tornadoes in a single day for IA, surpassing the previous record of 16 tornadoes on 7 June 1984 (Des Moines 2021). This QLCS also produced over 440 wind reports and 57 high-wind reports with gusts exceeding 75 mph (Fig. 3.17). Classified as a serial derecho (Squitieri et al. 2023a), this QLCS was characterized by strong forcing and had several bowing segments along the main convective line. Remarkably, this QLCS was the first documented derecho to occur in December anywhere in the US (Des Moines 2021), causing over 1 billion dollars in damages (NCEI 2021).

The 15 December 2021 QLCS/derecho event was selected for this study for a couple reasons: 1) it is a cold-season QLCS case that developed in a different environment than 30 March 2022 case study, and 2) it was a serial derecho (Johns and Hirt 1987; Squitieri et al. 2023a,b that produced numerous tornado and straight-line winds, indicative of embedded mesovortices.

3.2.3.2 Shear Analysis and QTor Forecasts

Only the 2200–2300 UTC forecasts are examined for the 15 December 2021 QLCS case, as the 2000–2100 UTC represented the QLCS as more cellular convection instead of a linear line. Consequently, the tornado reports in eastern NE will not be considered when verifying the forecasts, as they occurred before the 2200 UTC forecast. However, for the sake of completeness, those tornado reports will still be included on all figures to reflect the full impact of this event.

From the 2200 UTC forecast, it is immediately evident that the LP shear is dominating this case (Fig. 3.18a), similar to the 30 March 2022 case study. For 0–3-km LN shear, there is a small region of shear greater than 25 m s^{-1} that is collocated with a majority of the tornadoes that occurred in IA (Fig. 3.18b). Even though this maximum in LN shear does not include the tornado reports in northern IA and into MN/WI, each of the tornado reports in this area is associated with a small pocket of enhanced LN shear greater than 23 m s^{-1} (Fig. 3.18b). In the same location where there is a maximum in LN shear, there is also a swath of tortuosity between 1.10–1.20, suggesting the leading lines may be surging outward in this location (Fig. 3.18). Since the values of LP and LN shear exceed their respective thresholds (7 and 15 m s^{-1}) almost everywhere in the swaths, there is also a large QTor swath for this forecast (Fig. 3.18d). While the QTor swath does encompass all of the tornado reports for this QLCS, it also includes areas (specifically in IL and WI) without tornado reports that would be considered as false alarms (Fig. 3.18d).

The swath of strong LP shear remains consistent between the 2200 and 2300 UTC forecasts, except the areas where shear exceeds 30 m s^{-1} shear covers a larger area in the 2300 UTC forecast than the previous. For LN shear, there's a maximum in the northern portion of the swath that aligns with the majority of the tornado reports (Fig. 3.19b). There also seems to be more separation in the LN swath between the northern portion that contains the tornado reports and the southern portion that does not. The southern portion has lower LN shear than the northern, but the magnitudes still exceed the 15 m s^{-1} threshold. Tortuosity remains about the same between the 2200 and 2300 UTC forecasts (Fig. 3.19c). Finally the QTor swath in the 2300 UTC forecast covers most of the same areas as the 2200 UTC forecast, with one small difference (Fig. 3.19d). For the 2300 UTC forecast, there is a slight area of separation (QTor values less than 2.5) between the northern and southern portions of the swath (Fig. 3.19d). While most of the tornadoes are associated with higher values of LN shear (Fig. 3.19b), there is nothing substantially different between the northern and southern portions of the QTor swath that would suggest the northern portion would produce more tornadoes than the southern (Fig. 3.19d). Therefore, the southern portion of the QTor swath may be considered a false alarm. In the future, the QTor equation will need to be modified/tuned to decrease areas of false alarms.

The false alarms in QTor may be easier to observe using ensemble probabilities that it will exceed 2.50 (Fig. 3.20). The probability swath for the 2200 UTC forecast highlights the main location that is favorable for mesovortex tornadoes, and is also consistent with the reports in that area (Fig. 3.20a). The false alarm areas in IL, WI and associated with the southern portion of the QTor swath (Fig. 3.19d) have lower probabilities than the areas that did have tornado reports (Fig. 3.20a). The lower probabilities in the false alarm regions indicate an increase in ensemble spread and, thus, a decrease in confidence. The probability swath for the 2300 UTC forecast is comparable to the one at 2200 UTC, except there is now a larger area of probabilities near 1 that include the majority of tornado reports (Fig. 3.20b).

Differences in the WoFS and MRMS leading lines are examined to further understand the forecasts for this event (Fig. 3.21). First of all, the WoFS leading lines have a faster storm motion than the MRMS line, as they are typically leading the MRMS leading line (Fig. 3.21). Also, the bow apex in the MRMS leading line is sharper than the bowing segment in the WoFS leading lines (Fig. 3.21b,d). Lastly, and much like the other case studies, the WoFS leading lines typically have a different orientation compared to the MRMS leading line, which will change the magnitudes of LN and LP shear relative to the line (Fig. 3.21).

3.3 Summary

The 3IM is the current paradigm used by NWS forecasters to assess the likelihood that a specific QLCS segment will produce mesovortices and tornadoes (Schaumann and Przybylinksi 2012; Gibbs 2021). Two out of the three ingredients of the 3IM are based on RKW theory (Rotunno et al. 1988), which often breaks down in real-world scenarios (Evans and Doswell 2001; Coniglio and Stensrud 2001; Weisman and Rotunno 2004; Coniglio et al. 2012). For instance, the 3IM does not consider the magnitude of LP shear. Recent work by Brown et al. (2024) found that having low-level hodograph curvature (hence, 0–1-km LP shear) supported stronger, wider, deeper, and more persistent mesovortices. They also defined a critical threshold of LP shear between 7–10 m s^{-1} where there is ample support for persistent and intense mesovortices (Brown et al. 2024). The 3IM is also a subjective framework that depends heavily on radar coverage. It can also be a time-consuming and complicated process owing to the various confidence builders/nudgers that have been added to the process to increase a forecaster's confidence in issuing a QLCS tornado warning (Table 1.1; Schaumann and Przybylinksi 2012; Gibbs 2021).

Motivated by recent work by Brown et al. (2024) and knowing the inherent issues with the 3IM (reviewed in Section 1.1.3.2), this study aimed to investigate the potential of using upstream LP and LN shear relative to the leading line to forecast the potential for mesovortex tornadoes. A novel leading line analysis technique was created to isolate the leading line in both WoFS and MRMS, and then calculate the LP and LN shear relative to the line (Fig. 3.2). Also, a new composite forecasting parameter for QLCS mesovortex tornado potential, QTor (Eq. 3.9), was created as a way to bring aspects of the 3IM into an objective framework that could be implemented into convection-allowing models. This study serves as a first step or a proof-of-concept study to determine if a composite parameter such as QTor would offer any additional forecasting guidance for QLCS mesovortex tornado potential. The forecasts for three QLCS case studies that varied in location, season, time of day, and environment (Fig. 3.1) were analyzed to assess the performance of QTor and how it may vary with different types of QLCS cases. Results from the three case studies show a lot of promise for the utility of QTor. For all case days, the QTor forecasts were able to correctly identify locations favorable for mesovortex tornadoes, which also corresponded with the locations of tornado reports for each day. However, each QTor forecast did contain areas that would be considered false alarms. Therefore, with additional tuning, there is still room to improve the QTor parameter in the future.

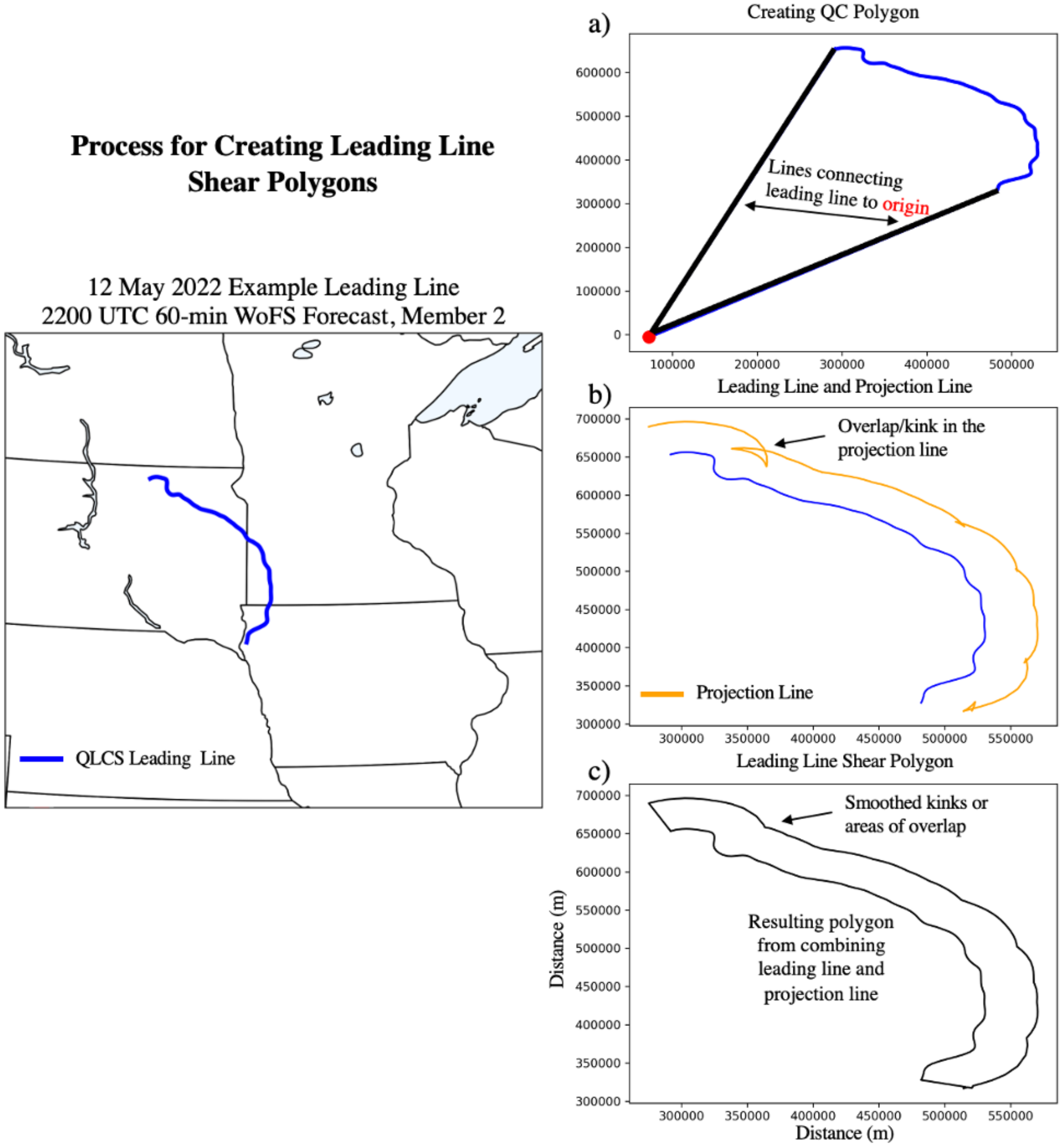

Figure 3.2: Process for creating the polygons used to calculate shear upstream of the leading lines. The example leading line (blue) is from the 2200 UTC 60-min WoFS forecast for ensemble member 2. The process is as follows: a) create a QC polygon by tracing each endpoint of the leading line to the origin (red dot), b) find the points for the projection line and QC them using the QC polygon to ensure they are not behind the line, and c) combining the leading line and projection line into one polygon results in the leading line shear polygon.

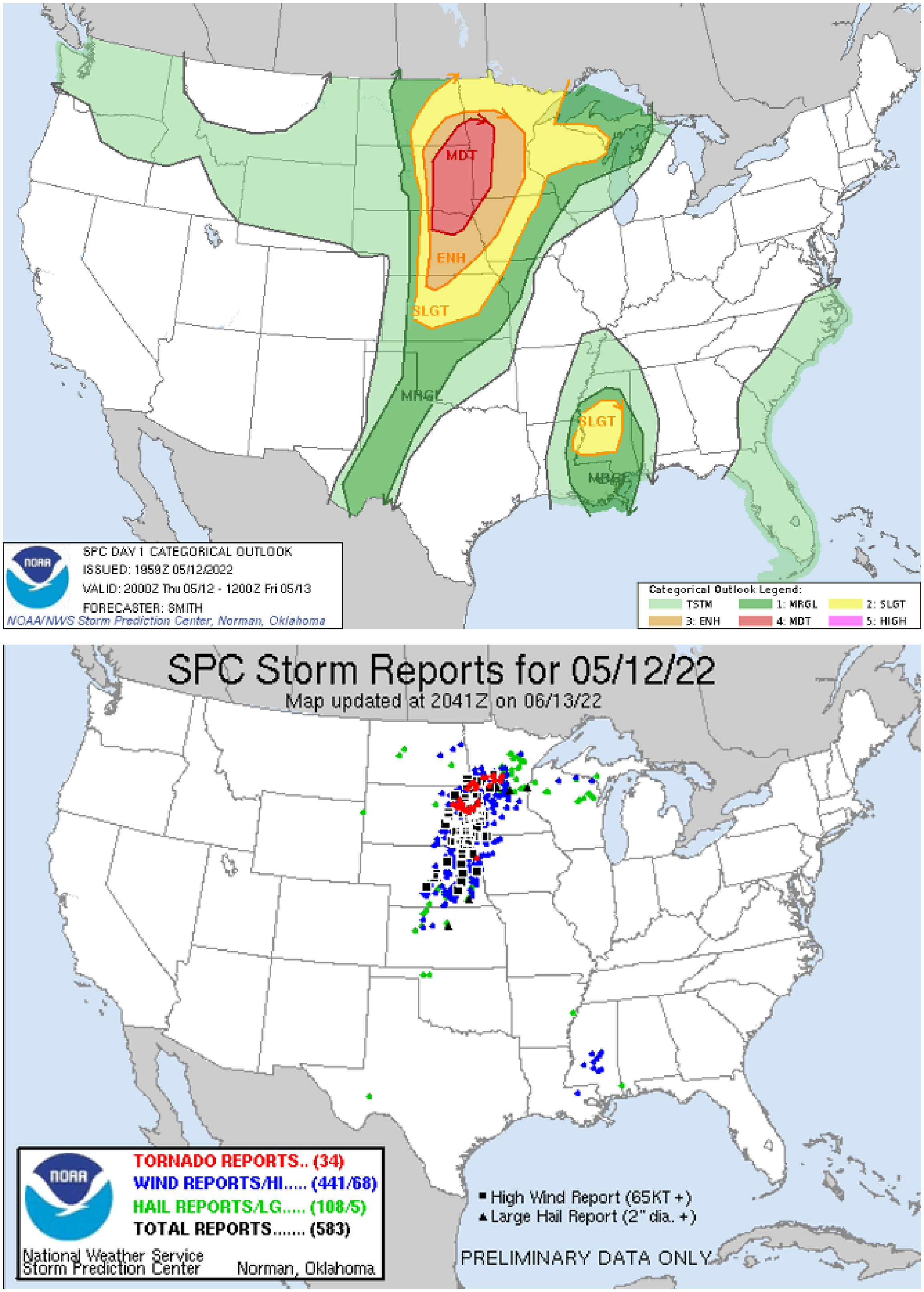

Figure 3.3: Day 1 convective outlook (top) and storm reports (bottom) for 12 May 2022, courtesy of the SPC.

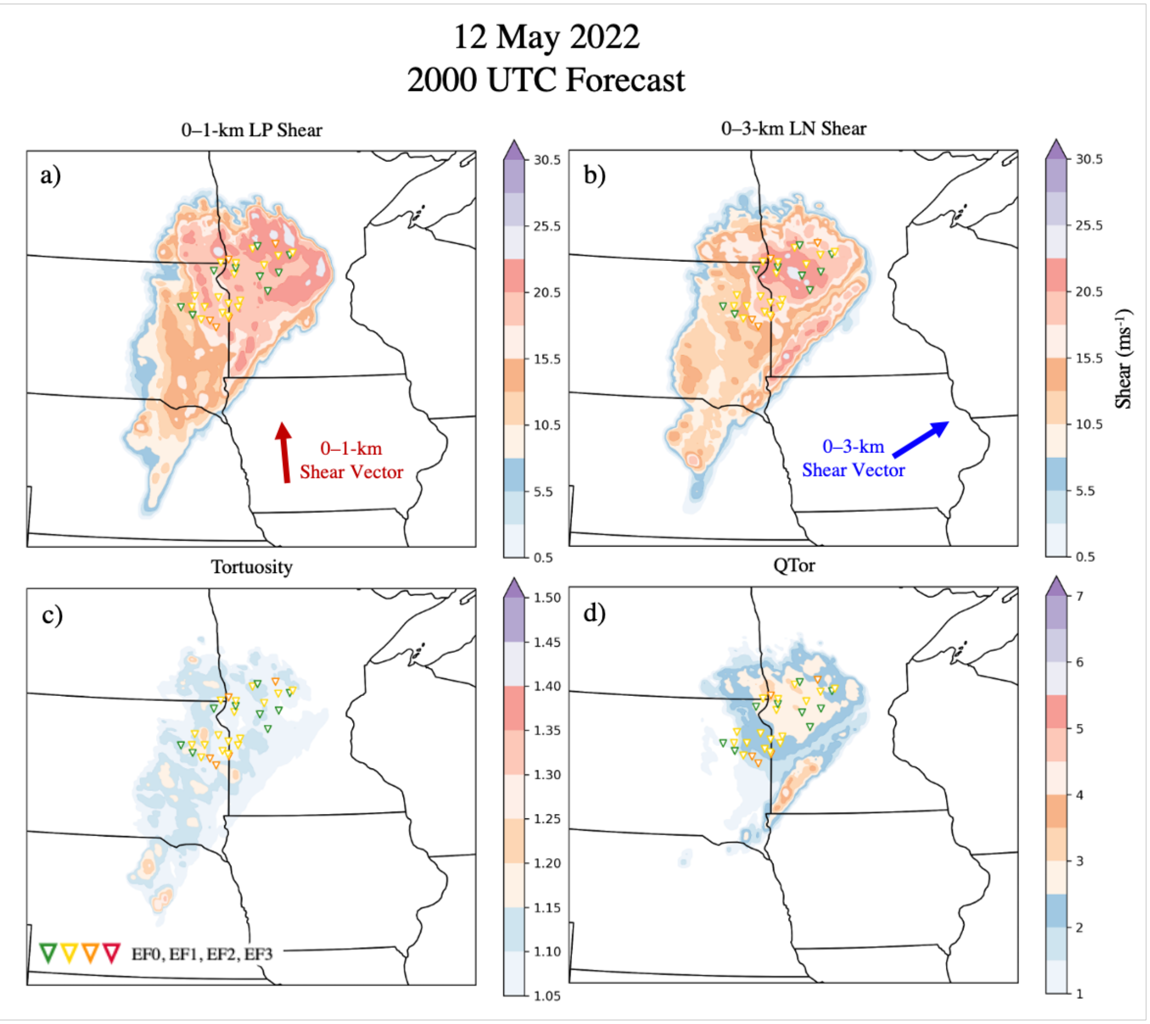

Figure 3.4: The 2000 UTC forecast for the 12 May 2022 QLCS event showing the 75th percentile swaths from 2000-0200 UTC for a) 0–1-km LP shear, b) 0–3-km LN shear, c) tortuosity, and d) QTor. All swaths are created using a 27-km neighborhood. The 0–1-km and 0–3-km shear vectors are estimated from WoFS soundings upstream of the QLCS. Swath valid from 2000–0200 UTC.

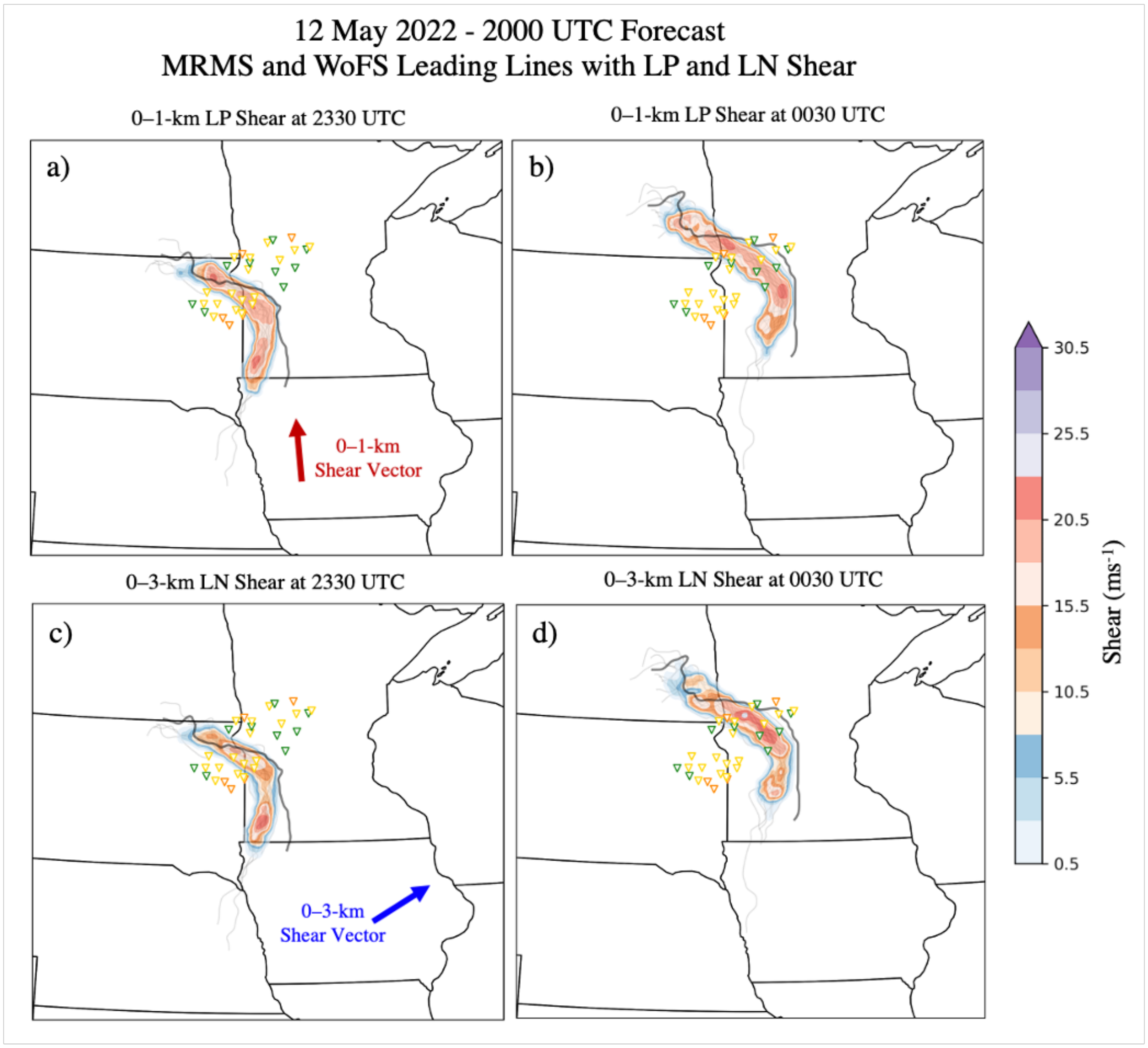

Figure 3.5: Panels showing differences in leading line orientation for MRMS (thick dark-gray lines) and WoFS (thin gray lines) leading lines for a) 0–1-km LP shear at 2330 UTC, b) 0–1-km LP shear at 0030 UTC, c) 0–3-km LN shear at 2330 UTC, and d) 0–3-km LN shear at 0030 UTC. Tornadoes are color-coded as in Fig. 3.4.

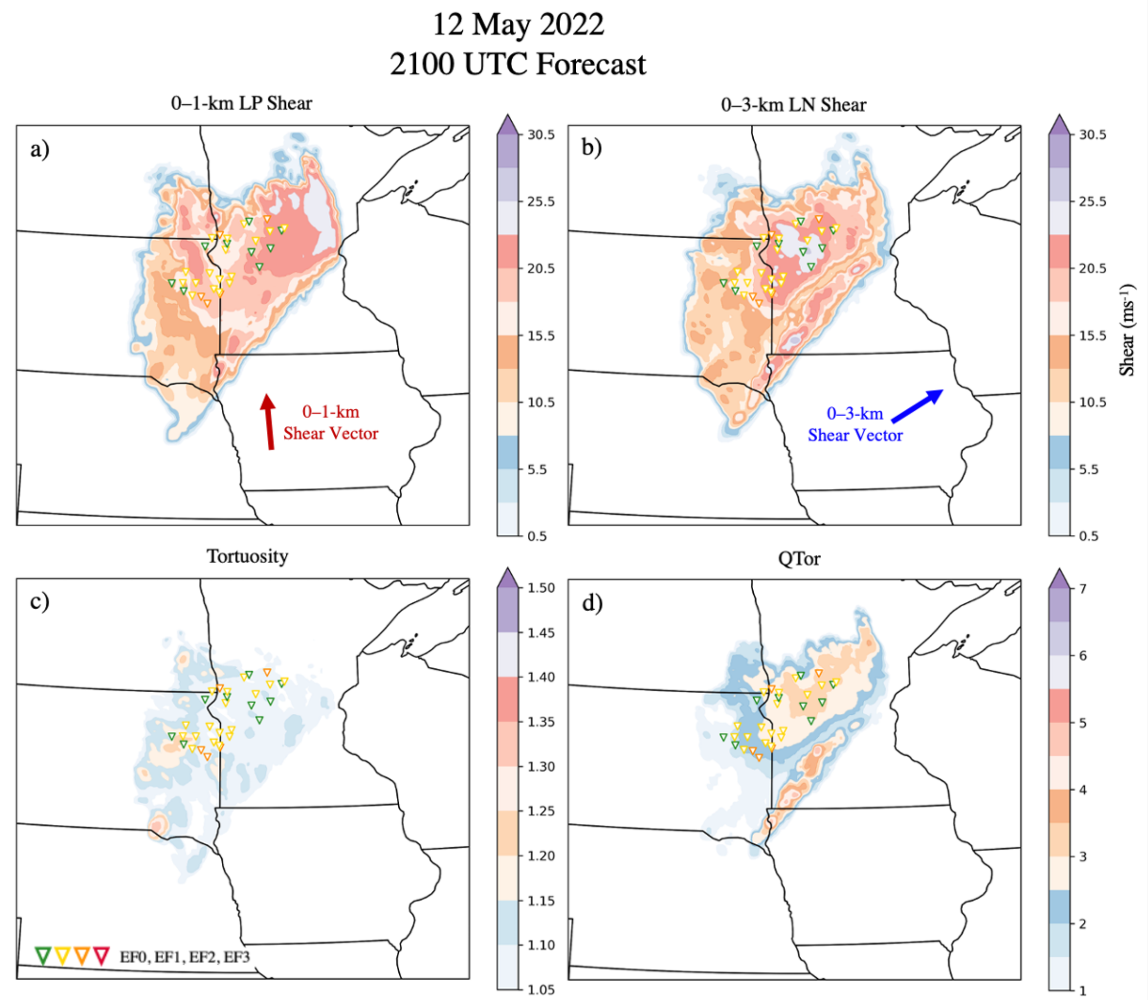

Figure 3.6: Same as in Fig. 3.4, but for the 2100 UTC WoFS forecast. Swath valid from 2100–0240 UTC.

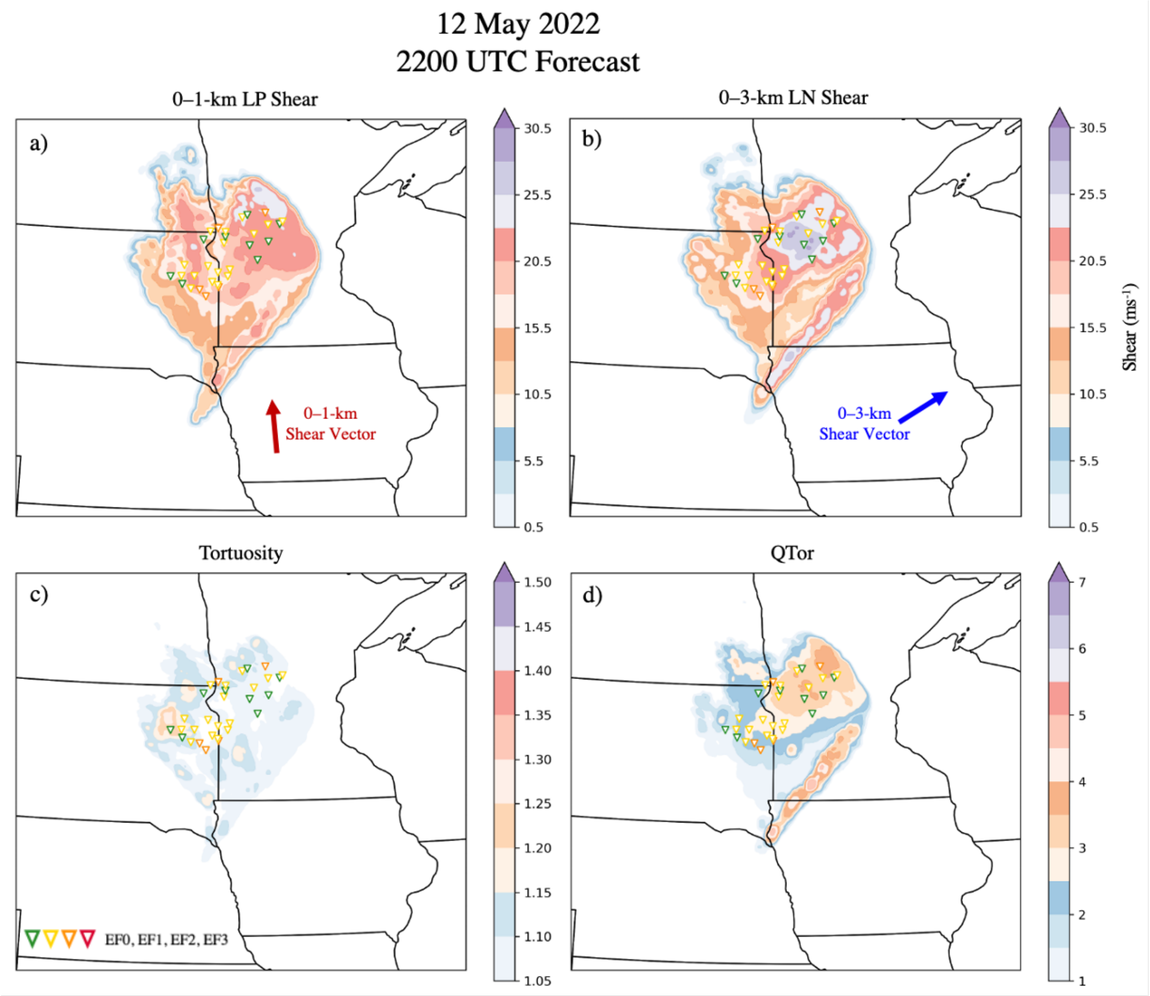

Figure 3.7: Same as in Fig. 3.4, but for the 2200 UTC WoFS forecast. Swath valid from 2200–0120 UTC.

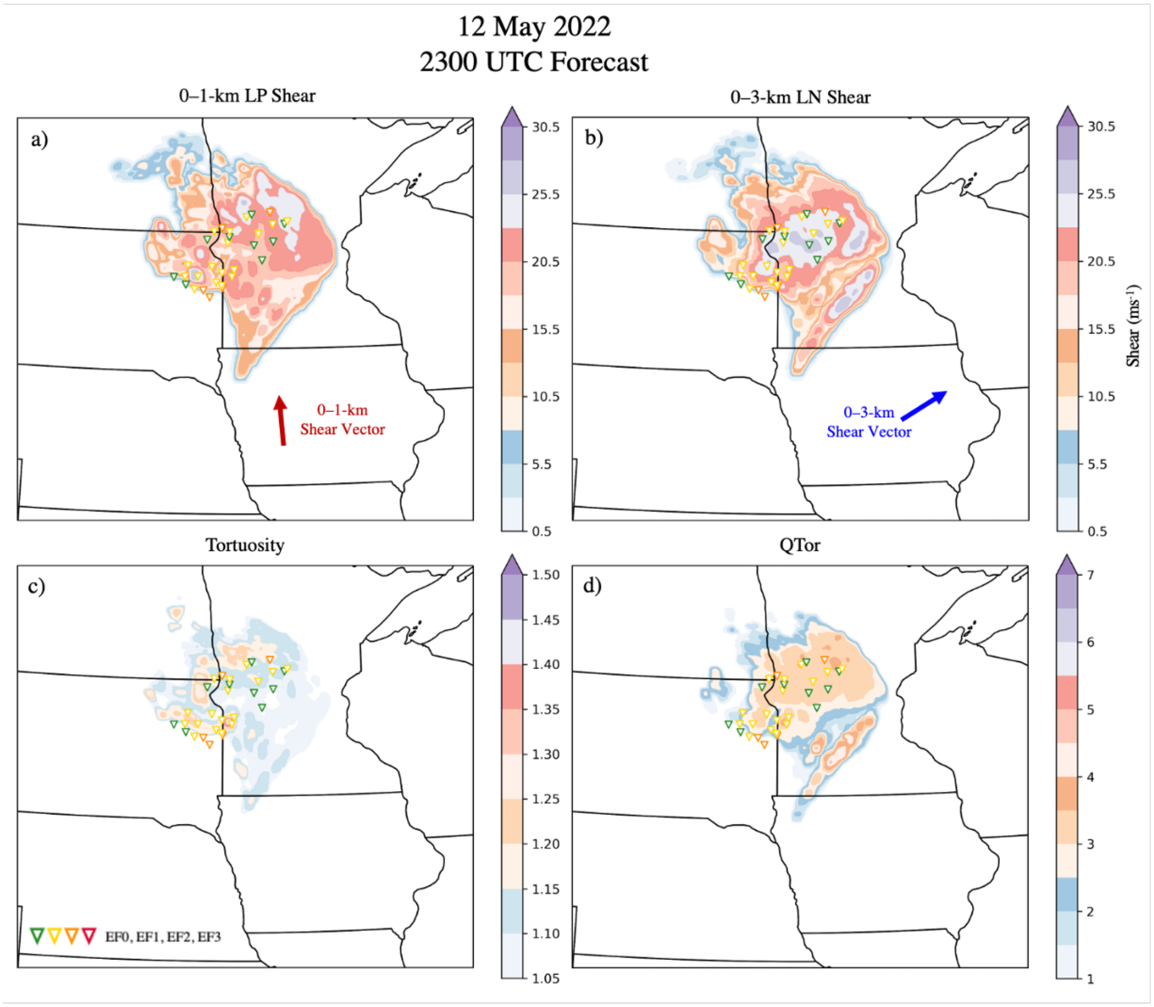

Figure 3.8: Same as in Fig. 3.4, but for the 2300 UTC WoFS forecast. Swath valid from 2300–0130 UTC.

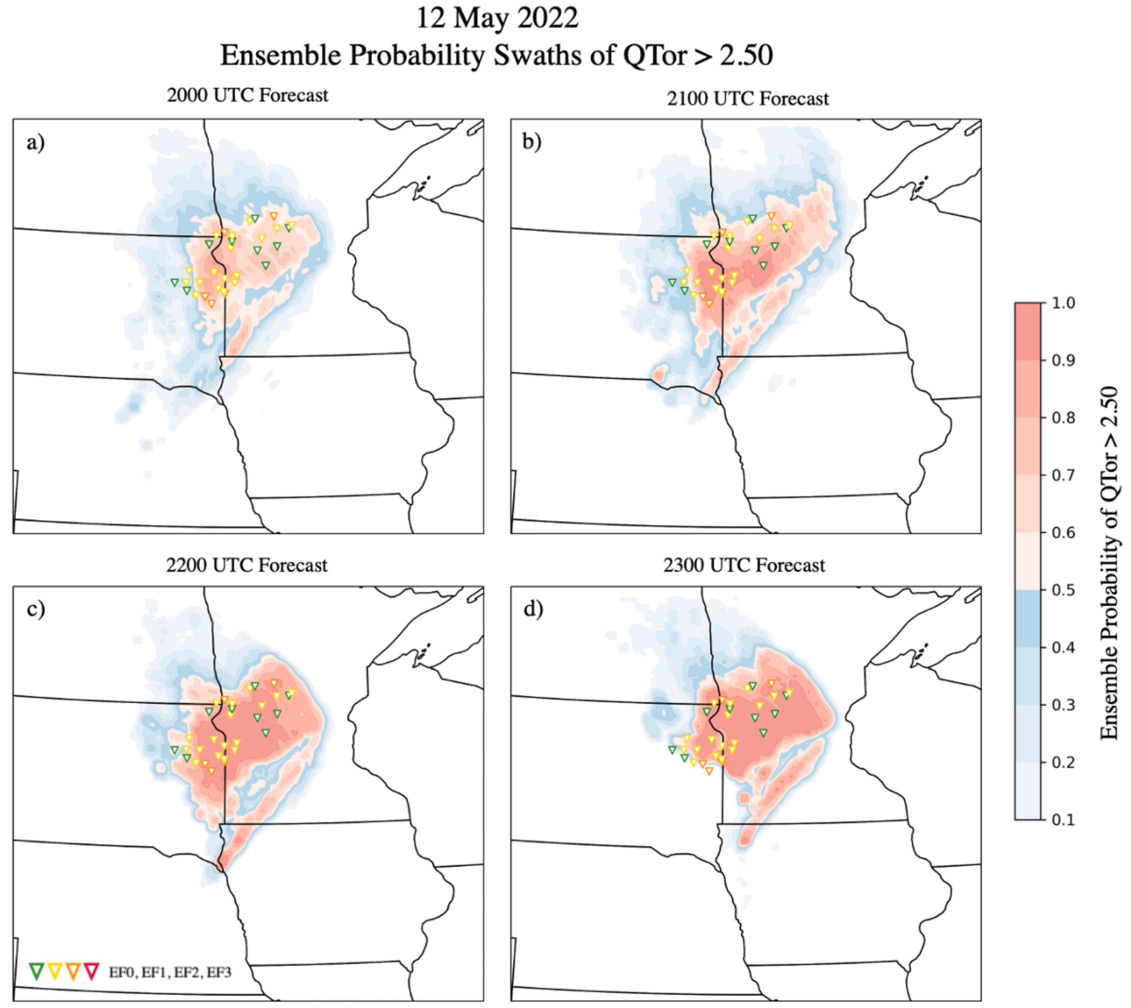

Figure 3.9: Ensemble probability swaths for QTor greater than 2.50 for the WoFS a) 2000, b) 2100, c) 2200, and d) 2300 UTC forecasts.

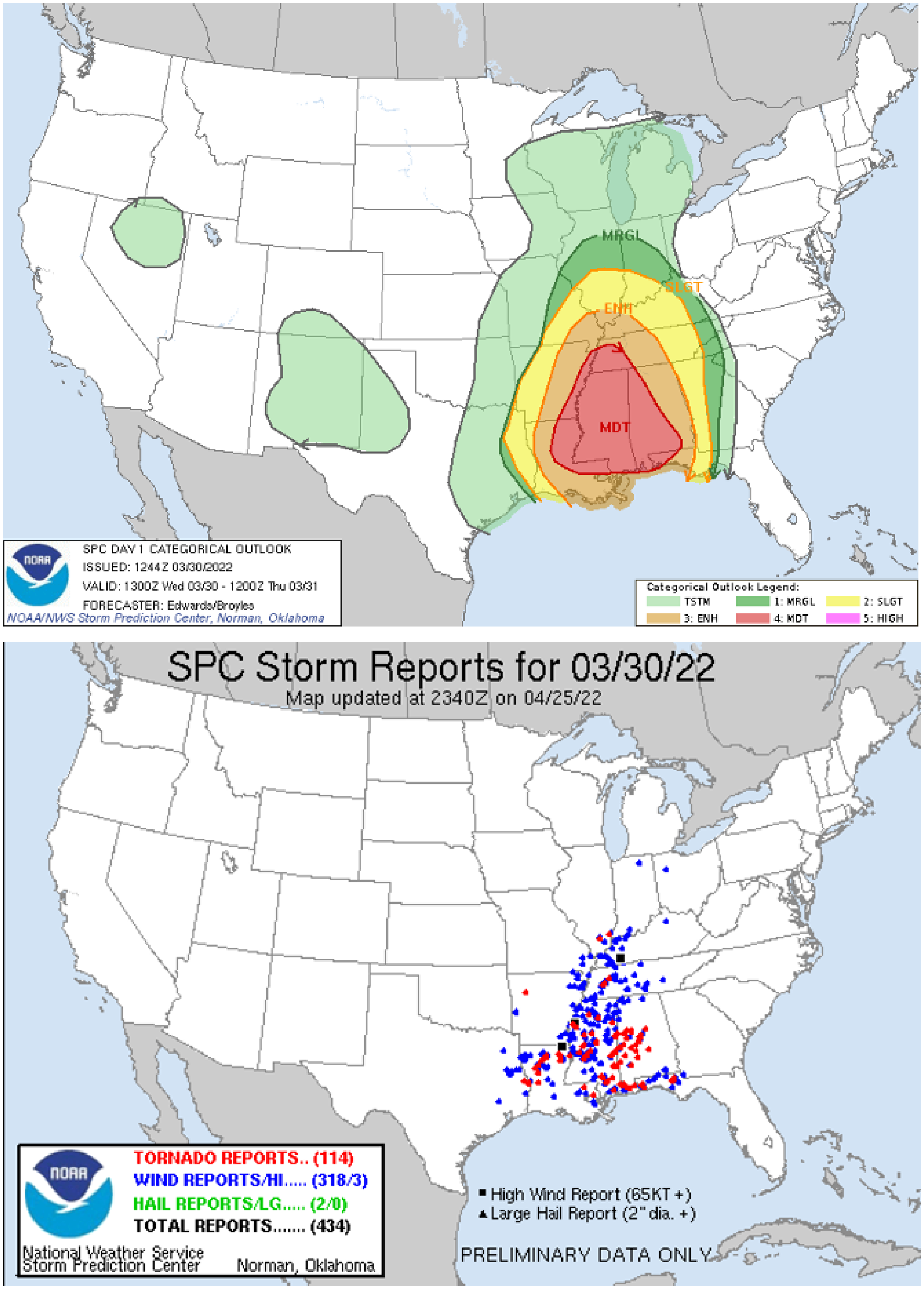

Figure 3.10: Day 1 convective outlook (top) and storm reports (bottom) for 30 March 2022, courtesy of the SPC.

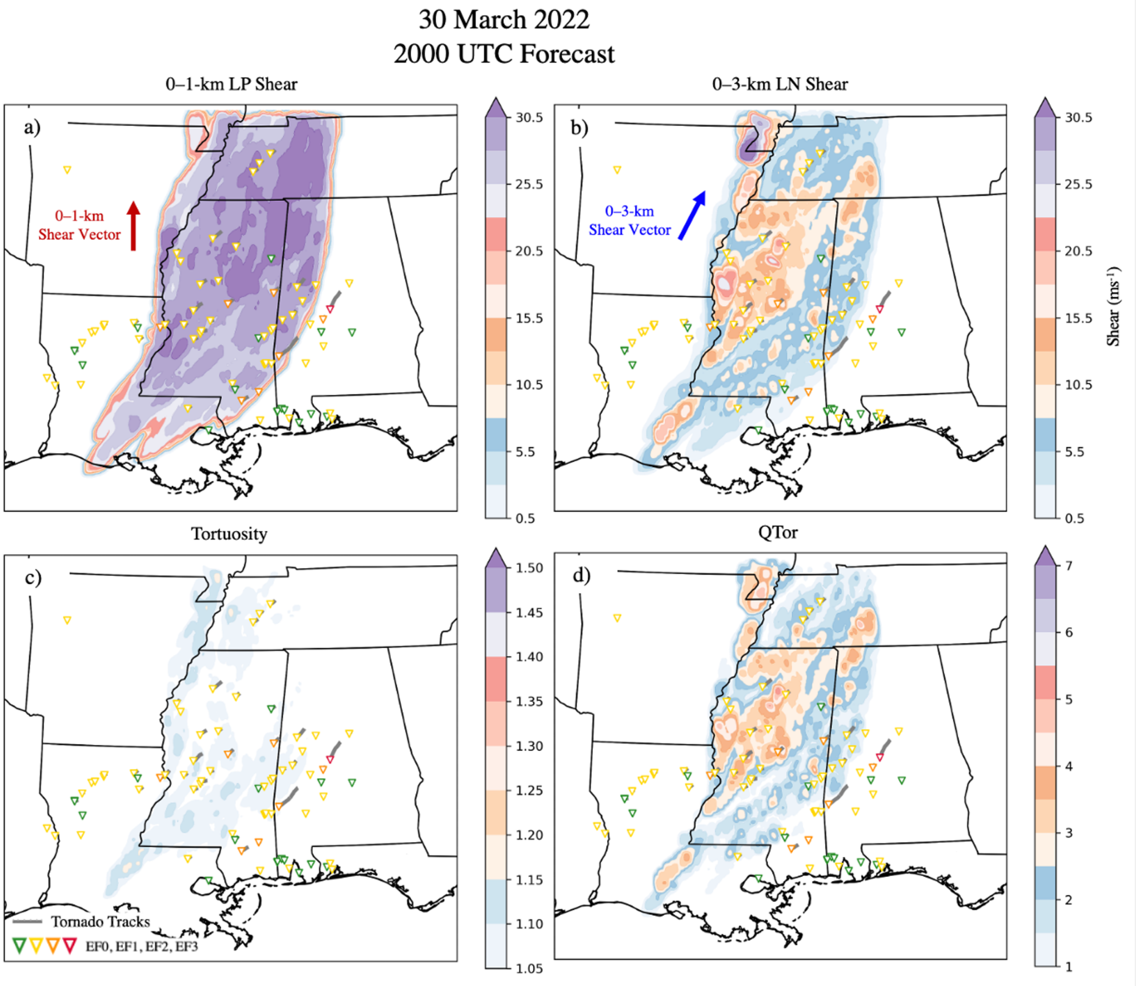

Figure 3.11: Same as in Fig. 3.4, but for the 2000 UTC WoFS forecast for the 30 March 2022 QLCS case. Swath valid from 2000–0200 UTC.

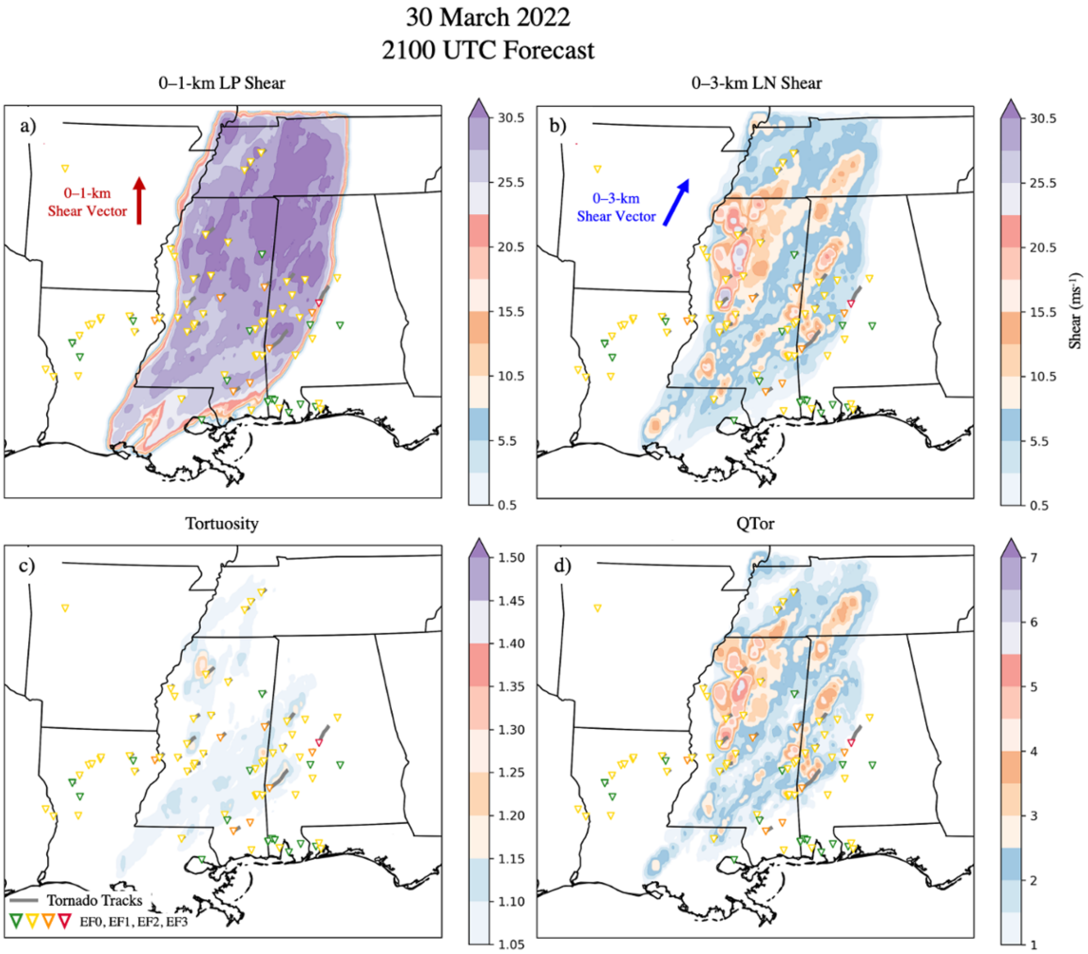

Figure 3.12: Same as in Fig. 3.11, but for the 2100 UTC WoFS forecast. Swath valid from 2100–0300 UTC.

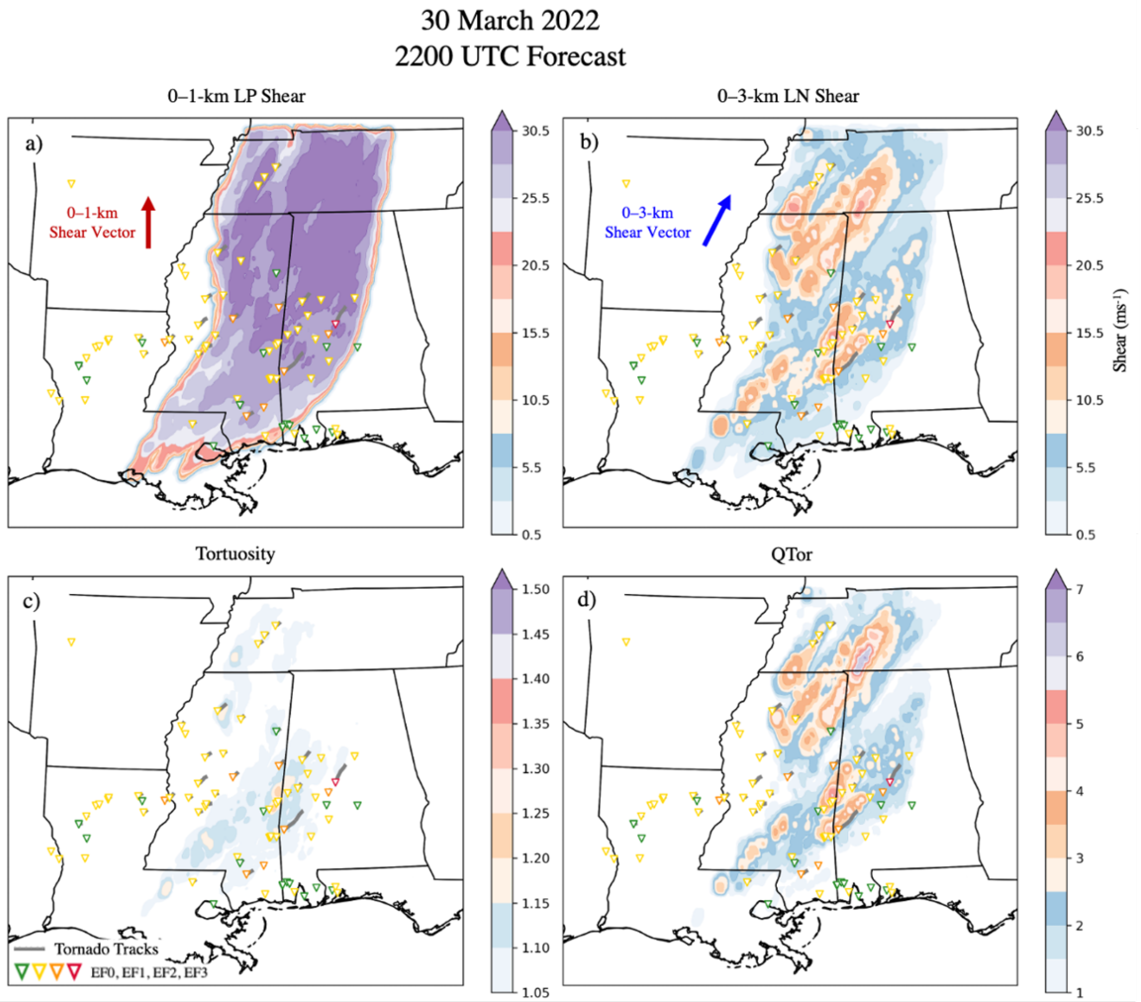

Figure 3.13: Same as in Fig. 3.11, but for the 2200 UTC WoFS forecast. Swath valid from 2200–0400 UTC.

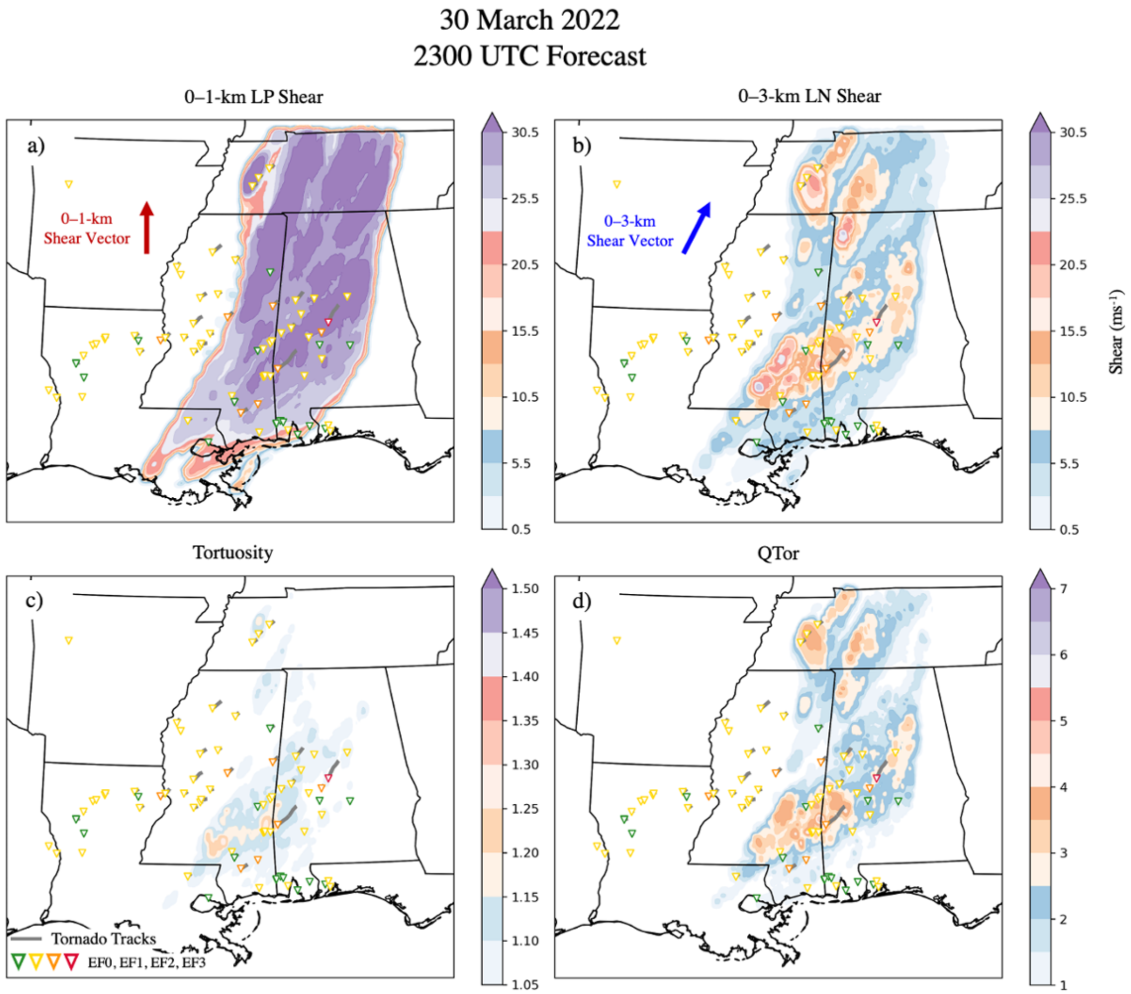

Figure 3.14: Same as in Fig. 3.11, but for the 2300 UTC WoFS forecast. Swath valid from 2300–0500 UTC.

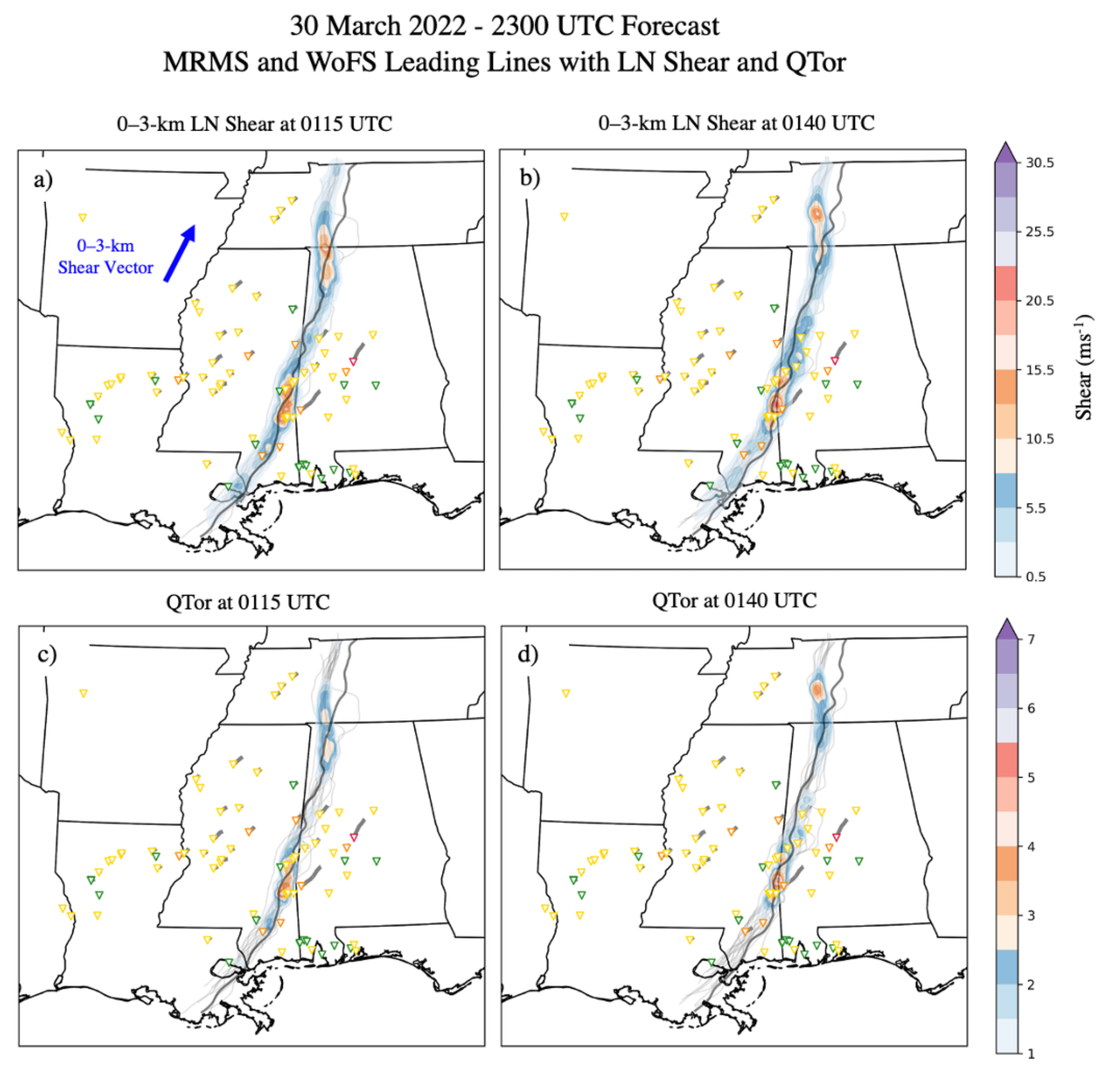

Figure 3.15: 2300 UTC WoFS forecast showing the MRMS (thick gray line) and WoFS (thin gray lines) leading lines with 0–3-km LN shear at a) 0105 UTC, b) 0115 UTC, and c) 0140 UTC. The 2300 UTC forecast was chosen as a representative example showing the differences between the WoFS and MRMS leading lines. However, these differences also occur in the 2100–2200 UTC forecasts.

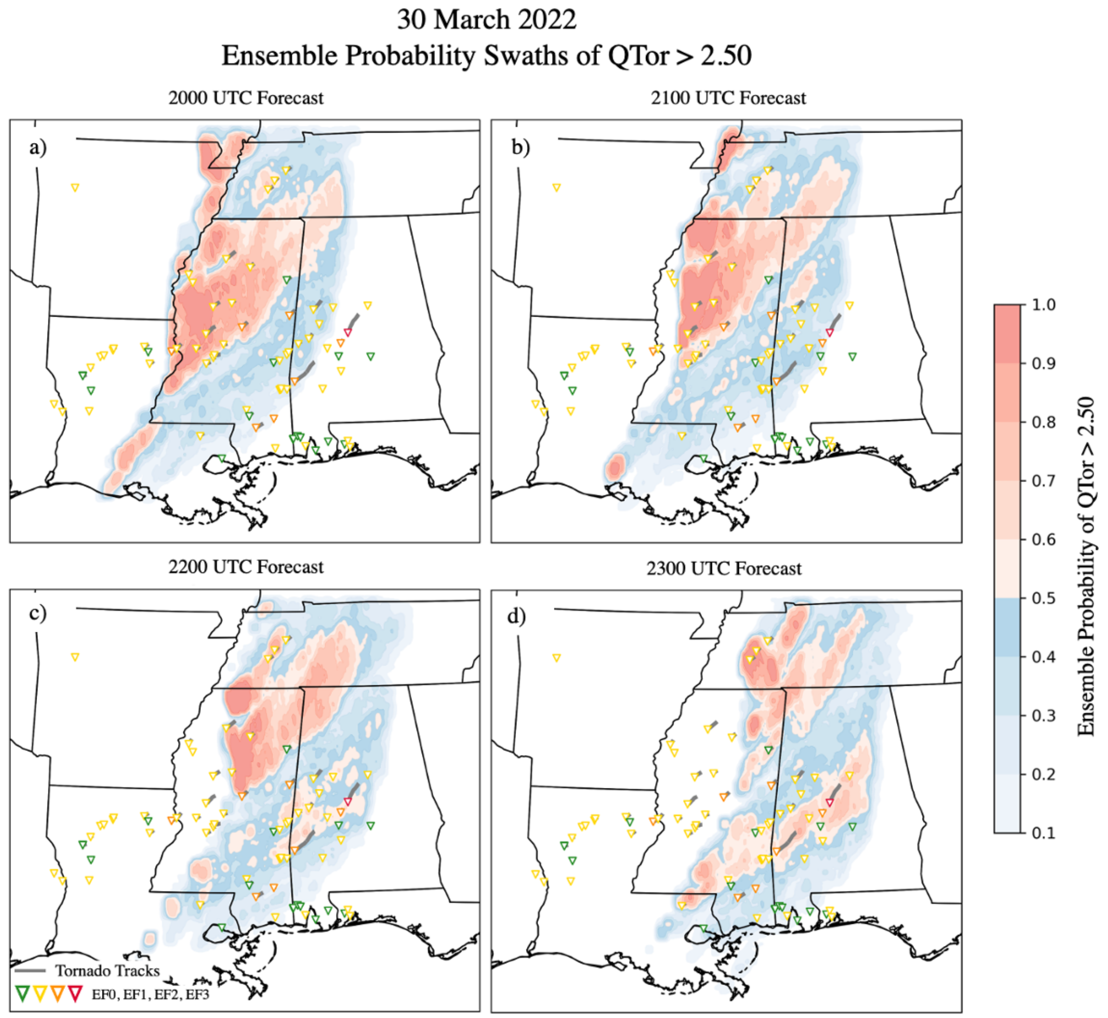

Figure 3.16: Same as in Fig. 3.9 except for the the 30 March 2022 QLCS.

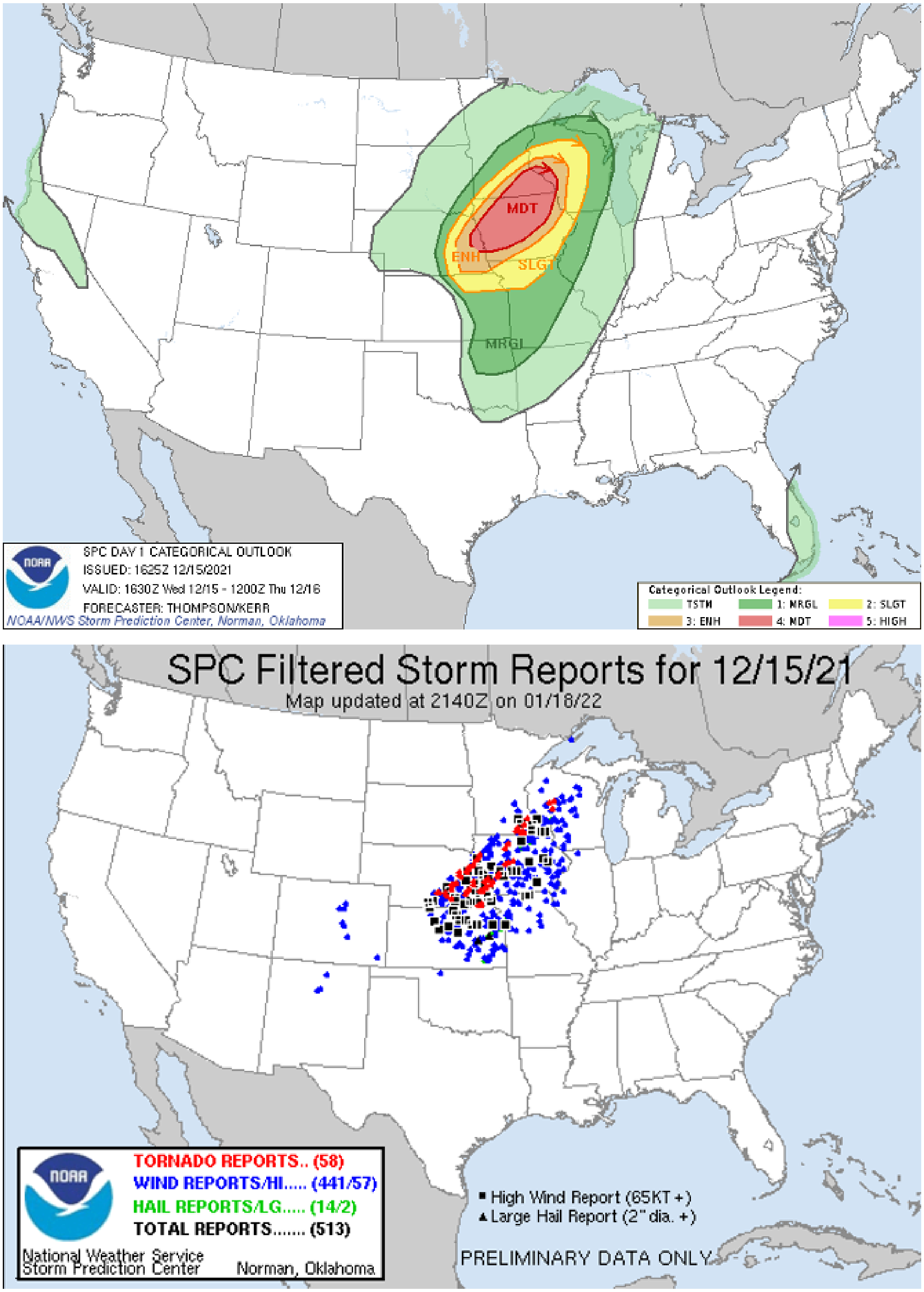

Figure 3.17: Day 1 convective outlook (top) and storm reports (bottom) for 15 December 2021, courtesy of the SPC.

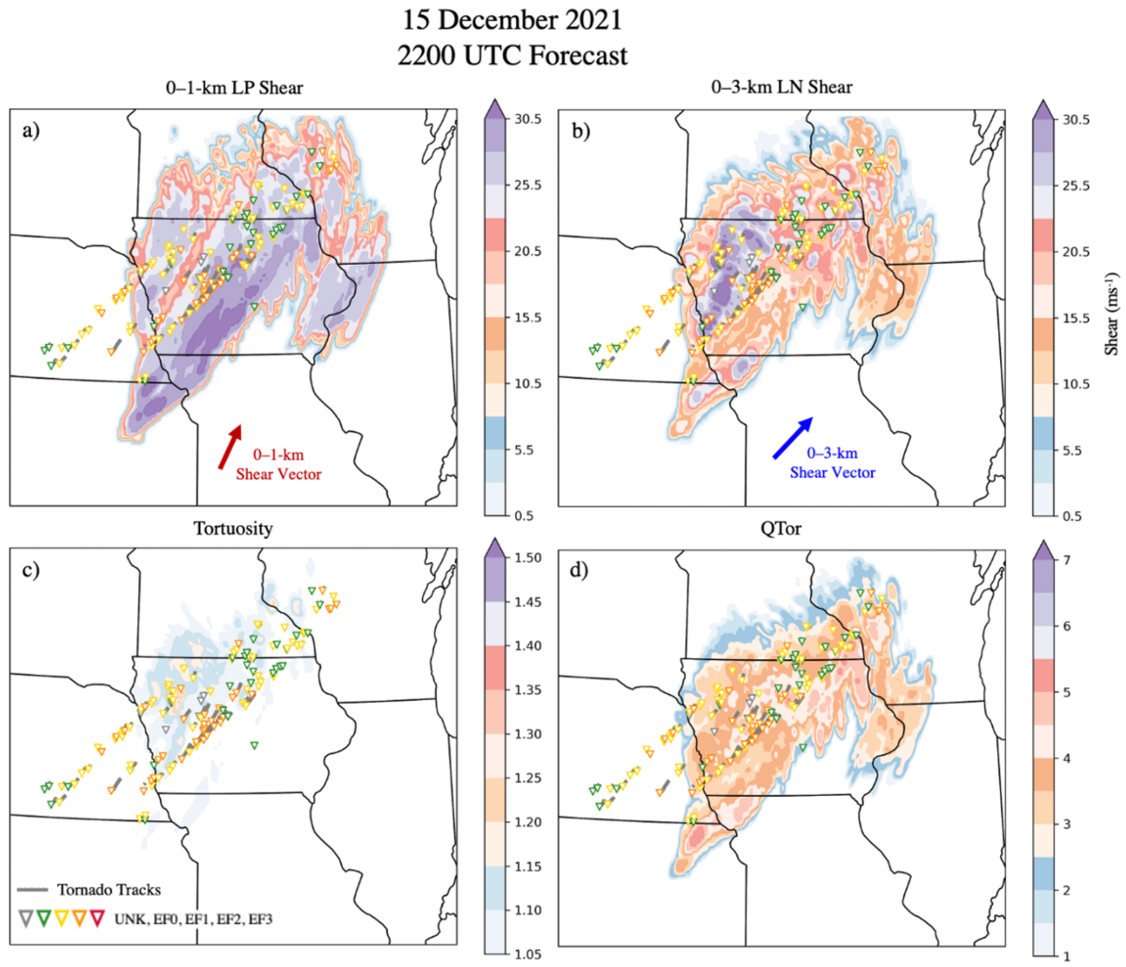

Figure 3.18: Same as in Fig. 3.4, but for the 2200 UTC WoFS forecast for the 15 December 2021 QLCS case. Gray tornado icons represent unknown EF-scale ratings. Swath valid from 2200–0400 UTC.

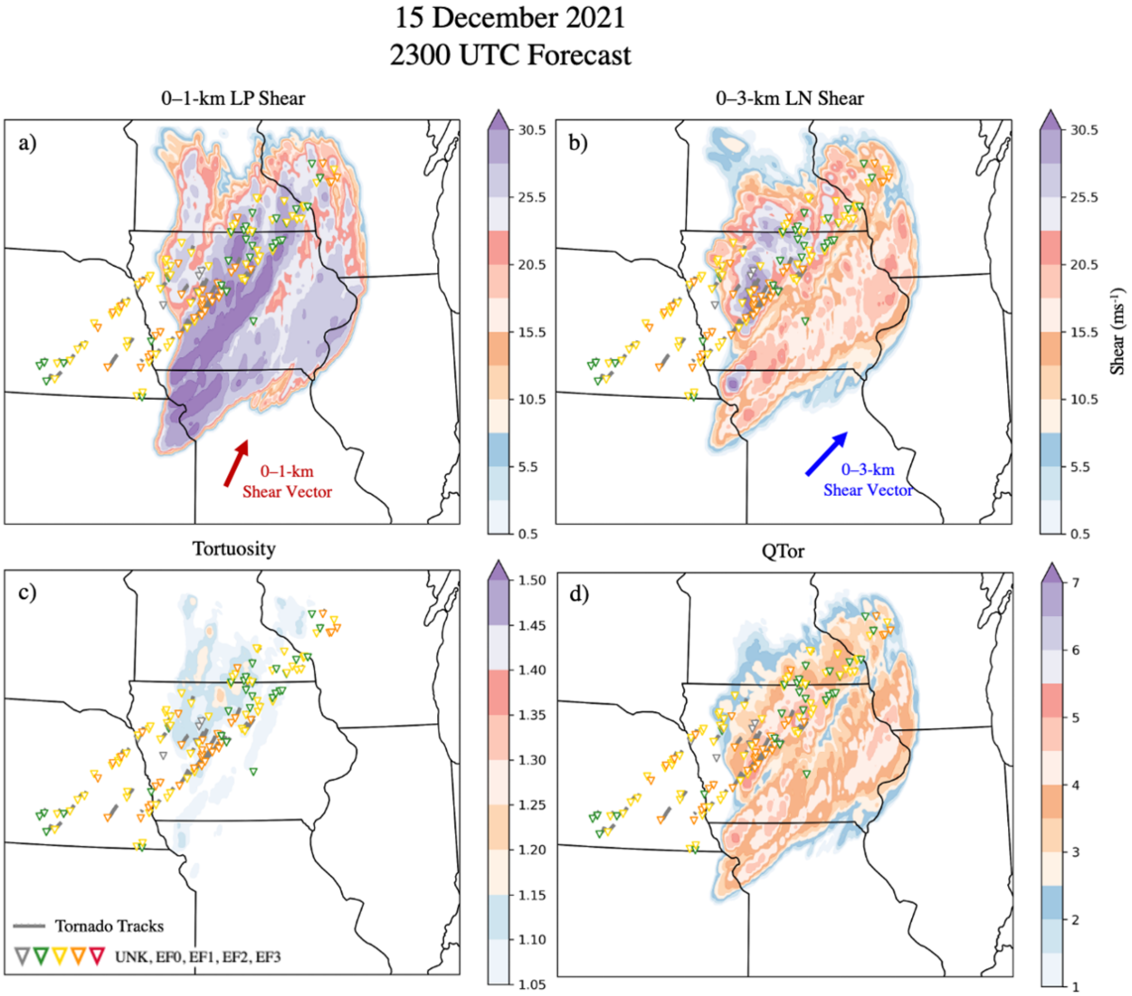

Figure 3.19: Same as in Fig. 3.18, but for the 2300 UTC WoFS forecast. Swath valid from 2300–0320 UTC.

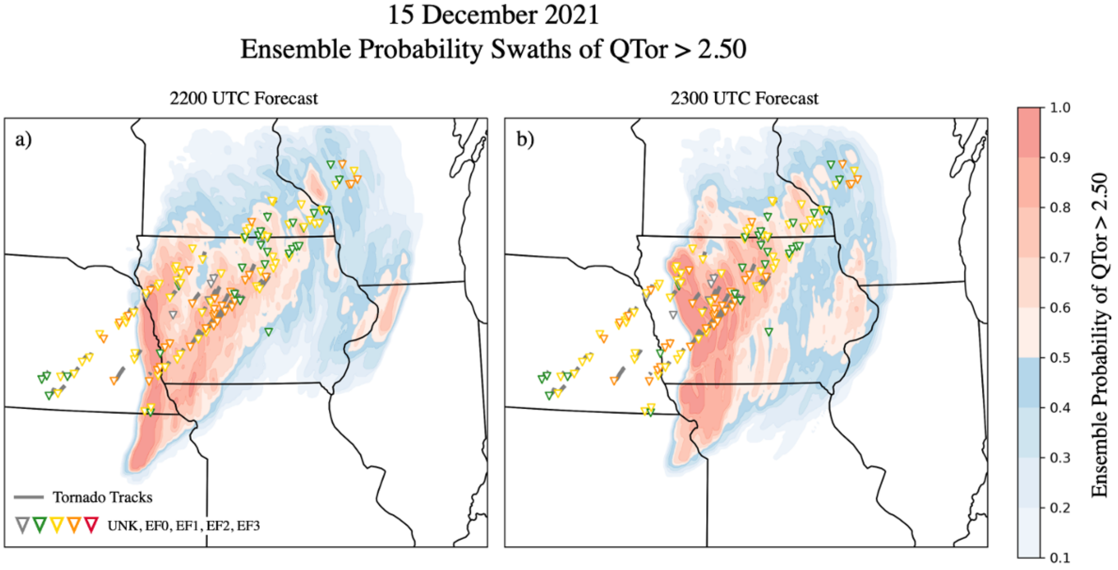

Figure 3.20: Same as in Fig. 3.9 except for the the 15 December 2021 QLCS case for the WoFS a) 2200 and b) 2300 UTC forecasts.

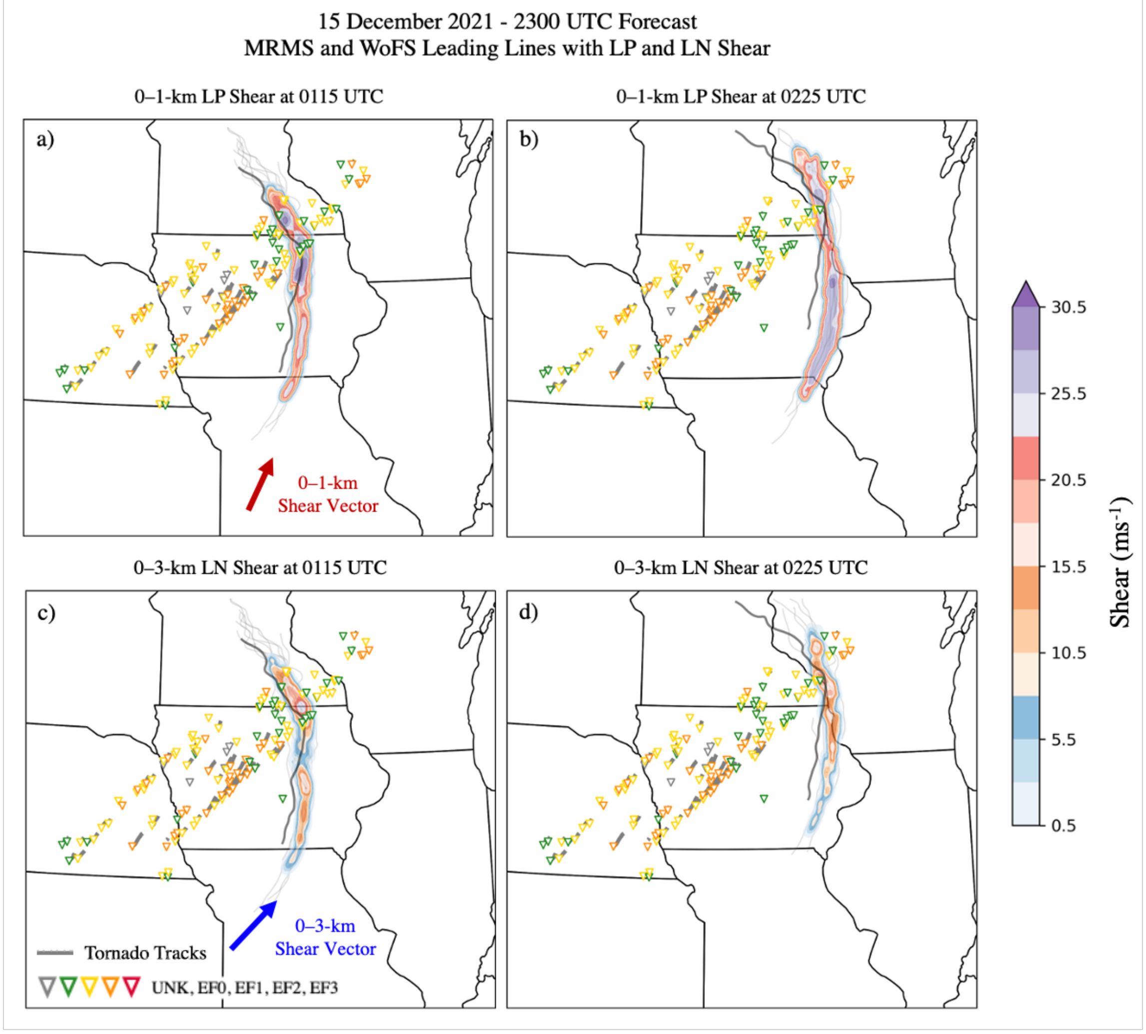

Figure 3.21: 2300 UTC forecast showing the MRMS (dark gray lines) and WoFS (thin gray lines) leading lines with 0–1-km LP shear at a) 0115 and b) 0225 UTC, and with 0–3-km LN shear at c) 0115 and d) 0225 UTC.

Chapter 4

Conclusions, Discussion, and Future Work

4.1 Conclusions

4.1.1 Part I: Verification of QLCSs in WoFS

The main objective of Part I of this research was to systematically evaluate WoFS's capability to predict QLCS spatial extent, timing, and location at 0–6-hr lead times. The research questions posed for this study are as follows:

1. How well do the 0–6-hr WoFS QLCS forecasts perform?
2. What are some of the differences in characteristics (e.g., size, shape, intensity) between forecasted and observed QLCSs?
3. Since typical object-based methods measure more large-scale differences, how can we measure more specific differences between forecasted and observed QLCS convective lines (e.g., line curvature, orientation, and location/displacement)?

The main findings from Part I of this study in the context of the above research questions are as follows:

1. Comparing the POD, FAR, bias, and CSI of QLCS forecasts (Fig. 2.5) with the forecasts for all storm modes (Fig. 2.6) shows QLCS forecasts have higher POD and CSI, and lower FAR than the forecasts for all storms. While the POD and CSI for the all-storm forecasts decreases with increasing forecast time, the POD and CSI for the QLCS forecasts stays rather constant, with only a slight decrease in each statistic with increasing forecast time. The FAR for the QLCS forecasts does increase slightly with forecast time, but stays consistently around 0.3–0.4 for the entire forecast period, whereas the FAR for all storms is above 0.6 by the end of the 6-hr forecast. Therefore,

the QLCS forecasts remain skillful throughout the entire 6-hr forecast compared to the forecasts for all storm modes.

2. WoFS QLCS objects are typically larger, more intense, and less eccentric than MRMS QLCS objects, and these differences increase with increasing forecast time. These differences may be attributable to the WoFS QLCSs including more of the stratiform region with increasing forecast time, which in turn may be due to the lack of a transition zone between the QLCS's stratiform and convective regions. As the intensity/reflectivity of the QLCS increases with time, the object identification algorithm may be including more of the stratiform region as part of the convective line object. Including more of the stratiform region would in turn create larger and more circular (hence, less eccentric) QLCS objects in WoFS.

3. A novel centerline analysis technique was created to measure the more specific differences between forecasted and observed QLCSs. This technique identifies the centerline of the QLCS convective line objects to measure the more small-scale differences in location, curvature/tortuosity, and orientation. Without the centerline method, these properties would be washed out by using the full object. Results showed that compared to MRMS centerlines, the WoFS QLCS centerlines tended to be more tortuous and they rotate cyclonically in orientation with increasing forecast time. Displacement between the WoFS and MRMS centerlines was found to be mainly influenced by the storm propagation speed as most of the displacement was in the NE (meaning WoFS centerlines are traveling faster than MRMS) and SW (MRMS centerlines lead WoFS) quadrants. We found these results to be consistent with WoFS overforecasting the intensity of the QLCS's northern bookend vortex and, subsequently, the RIJ.

4.1.2 Part II: Forecasting Mesovortex Tornado Potential

Part II of this study serves as a “proof-of-concept” that explores the potential for using upstream shear relative to the leading line to forecast mesovortex tornado potential. This project is a first-step to creating a more objective and effective method for predicting mesovortex tornadoes than the 3IM (Schaumann and Przybylinksi 2012; Gibbs 2021). The research questions that were posed for this project are as follows:

1. Can line-parallel and line-normal shear upstream of a QLCS’s leading line be used to provide forecast guidance for mesovortex tornado potential?
2. What other leading line characteristics can be used to forecast mesovortex tornado potential?
3. How can the subjective framework of the 3IM be transformed into an objective framework that can be integrated into convection-allowing modeling systems?

The main conclusions relative to the above research questions are summarized as follows:

1. Using a system-relative framework to calculate the LP and LN shear relative to the local orientation of the leading line did locate areas favorable for QLCS mesovortex tornadoes that aligned with tornado reports for each case study. However, the magnitudes of LP and LN shear depend on the local orientation of the leading line. Part I of this study found the orientation of WoFS centerlines typically rotated cyclonically with forecast time, which creates a source of forecast error and a limitation when calculating the magnitudes of LP and LN shear.
2. The local tortuosity defines the curvature along the leading lines and does indicate areas of increased curvature corresponding with areas along the leading lines that are surging or bowing outward. Local tortuosity can take the place of the third 3IM ingredient which states that the presence of a RIJ, local surge, or bow in the leading

line has an increased chance of producing mesovortex tornadoes. Local tortuosity brings this 3IM ingredient into a objective framework that can be implemented in NWP models. While local tortuosity does highlight areas where the leading lines are bowing or increasing with curvature, the values are still quite small and won't have a huge impact on the QTor equation. Therefore, local tortuosity may need to have a multiplier applied to better highlight areas of increased curvature.

3. By creating a new composite parameter, QTor, we are able to transform the current, subjective framework of the 3IM into an objective framework that can be implemented into WoFS to provide guidance to forecasters for mesovortex tornado potential. QTor has three main parts (Eq. 3.9): 1) the magnitude of 0–1-km LP shear normalized by the threshold found in Brown et al. (2024), 2) 0–3-km LN shear normalized by the threshold set by 3IM, and 3) the local tortuosity that takes into account the line curvature (more curvature is a sign that the leading lines may be bowing outward, another ingredient of the 3IM).

4.2 Discussion and Future Work

One of the main takeaways from Part I (Chapter 2) of this study is that WoFS has skill in forecasting QLCSs, and that skill remains fairly constant throughout the 6-hr forecast. While this is promising, there are still some limitations and caveats inherent to these forecasts. First of all, the overprediction of the reflectivity and northern bookend vortex associated with the QLCS may influence the veracity of the hazard forecasts. For example, having more intense reflectivity values throughout the QLCS may cause an overprediction in the precipitation forecasts. Additionally, WoFS overpredicting the intensity of the northern bookend vortex may impact the wind forecasts and the forecasts for tornado potential. Results presented in Chapter 3 suggest the mesovortex tornado potential relies heavily on the orientation of the leading line, and Part I of this study found orientation differences between MRMS and WoFS tended to increase with increasing forecast time. Consequently, errors in line orientation will affect the calculations for LN and LP shear, leading to more false alarms and incorrect forecasts for tornado potential.

Future work should also investigate the reason for WoFS's overprediction of the northern bookend vortex and, subsequently, the RIJ. One method for diagnosing this overprediction is by analyzing potential vorticity (PV) anomalies in forecasted and observed QLCSs (Galarneau et al. 2023). Galarneau et al. (2023) started this analysis and found that WoFS was generating a large warm anomaly in potential temperature around 700 mb, which in turn is associated with a positive PV anomaly. One hypothesis for why this warm anomaly exists is from enhanced diabatic heating (Galarneau et al. 2023). However, there is still some uncertainty for how this anomaly can be dampened, or if it can be fixed at all. Therefore, future work should also explore this in more depth as it does have implications for QLCS forecasts as a whole, and especially for the forecasts of mesovortex tornado potential.

Other avenues for future work in the context of Part I include analyzing and comparing the surrounding environments around forecasted and observed QLCSs to understand how these differences may impact the system's physical structure and internal dynamics. This study was unable to examine cold pool structure and depth given our dataset, but this would be worth pursuing in the future. This examination should also include in-depth case studies using radar and specialized observations from field experiments (e.g., TORUS, Houston et al. 2022; PERiLS, Kosiba et al. 2022) that may also aid in determining or further understanding the overprediction of the bookend vortex and RIJ in WoFS.

Part II of this research showed the utility of creating a new composite parameter to forecast QLCS mesovortex tornado potential. The creation of QTor was just the first step, but it does show promise in forecasting areas favorable for mesovortex tornadoes, which also matched with documented tornado reports. As this is the first step, there are a few aspects of QTor that will need to be revised in the future to potentially create an even stronger and more effective parameter to forecast QLCS tornadoes.

First of all, the forecast errors associated with WoFS QLCS prediction will impact the forecasts for mesovortex tornado potential. All three of the QLCS cases analyzed in Part II of this study showed differences in orientation and speed of the WoFS leading lines compared to the MRMS leading lines (Figs. 3.15, 3.15, and 3.21). Even small differences in the orientation can vastly change the magnitudes of LP and LN shear along the line, resulting in possible false alarms or missing areas of increased tornado potential. To get a better understanding of how these orientation differences affect the magnitudes of LP and LN shear, they need to be verified against another source. For this current study, only the tornado reports and tracks were used as a way of verifying the QTor forecasts. In the future, however, the shear relative to the MRMS leading line will also need to be calculated so that it can be compared to the WoFS forecasts. MRMS does not contain 0–1-km or 0–3-km shear fields, thus, the WoFS analyses will need to be utilized. Every 15-min WoFS analysis can be used to calculate the LP and LN shear relative to the MRMS leading line. This is a similar process to that shown in Fig. 2.15, in which the WoFS 0300 UTC analysis was compared to the 0000 UTC 180-min WoFS forecast (also valid at 0300 UTC) for the 17 July 2020 QLCS event. One other verification source that will be included in the future is archived tornado warnings. Not every mesovortex will develop a tornado, or may even have a tornado report associated with it. Therefore, overlaying tornado warnings in addition to the tornado reports/tracks, will provide an additional source of verification that can then be used to assess the skill of the QTor forecasts.

Secondly, the QTor thresholds for LP and LN shear may also need to be tuned to better fit the environments in which the QLCS develops. For example, high magnitudes of LP shear were observed for both the 30 March 2022 and 15 December 2021 case studies. In these cases, the LP shear typically exceeded the 7 m s^{-1} threshold set by the QTor equation almost everywhere, causing large swaths of QTor that included areas where tornadoes were not reported. Consequently, this can increase the amount of QTor false alarms. One way to potentially mitigate false alarms is to apply seasonal or location-based thresholds for

LP and LN shear. For example, cold-season QLCSs or those that form in high-shear, low-CAPE environments (as in the 30 March and 15 December case studies) often have more LP shear associated with them than warm-season QLCSs (Sherburn and Parker 2014; Sherburn et al. 2016; King et al. 2017; Chasteen and Koch 2022). Therefore, the threshold for LP shear may need to be increased and the LN threshold may need to be decreased for those types of QLCSs. Alternatively, weights could be applied to the QTor equation that may change depending on the environment and season the QLCS is expected to develop in.

Another aspect of the QTor equation that will need to be revised is the local tortuosity term. The LP and LN shear components of the QTor equation are normalized based on the thresholds from the 3IM and Brown et al. (2024). However, the local tortuosity is currently not normalized. Consequently, the value of local tortuosity does not penalize QTor for having very low values around 1.0–1.05, which would suggest little to no curvature in the lines. Areas of QTor false alarms typically had little to no tortuosity values. Therefore, normalizing the local tortuosity by the value that is most consistently observed with bowing segments (around 1.10–1.15) in the WoFS forecast may mitigate areas of false alarms by punishing (i.e., decreasing QTor values) the areas that have little to no curvature and rewarding (i.e., increasing QTor values) the areas that do. Tortuosity may also need to be multiplied by some factor so that it has a greater impact on the QTor forecasts.

Additional terms may also need to be included as part of the QTor equation. Parameters such as CAPE and CIN can provide more information about the stability and buoyancy in the environment upstream of the QLCS. Including these parameters may also improve the false alarms in QTor by lowering the potential in areas that are capped. In cases where CAPE is low (high-shear, low-CAPE QLCSs and cold-season QLCSs) it might be better to use 0–3-km lapse rates, as those improved the discrimination between severe and non-severe convective events in studies like Sherburn and Parker (2014) and Sherburn et al. (2016). Different iterations of QTor can be tested using more QLCS case studies that differ in seasonality, time of day, and environment to understand which perform the best.

Finally, the end goal of Part II of this project is to create a composite parameter for QLCS tornado potential that will eventually be included in WoFS, but will have the versatility to be implemented into any convection-allowing model. To reach this goal, however, there are still many challenges to overcome. First, processes for generating centerlines and leading lines will need to be fully automated for use in a real-time forecasting system like WoFS. Another challenge is calculating the storm motion and propagation of QLCSs in real-time, as the storm motion was only estimated in the current study. Moreover, the finalized composite parameter will have to go through multiple rounds of testing using a larger sample of QLCS cases. A portion of the testing phase should take place in the HWT (Clark et al. 2020, 2021), to assess the parameter's performance and collect feedback from operational forecasters that can then be used to adjust and improve the parameter as needed.

Bibliography

Aberdeen, S. W. F. O., 2022: May 12th, 2022 derecho summary. https://www.weather.gov/abr/StormsummaryMay122022 [Accessed: 24 June 2024].

Anderson, J., T. Hoar, K. Raeder, H. Liu, N. Collins, R. Torn, and A. Avellano, 2009: The Data Assimilation Research Testbed: A community facility. *Bull. Amer. Meteor. Soc.*, **90**, 1283–1296.

Anderson, J. L., and N. Collins, 2007: Scalable implementations of ensemble filter algorithms for data assimilation. *J. Atmos. Oceanic Technol.*, **24**, 1452–1463, doi:10.1175/JTECH2049.1.

Ashley, W. S., A. M. Haberlie, and J. Strohm, 2019: A climatology of quasi-linear convective systems and their hazards in the United States. *Wea. Forecasting*, **34**, 1605–1631, doi:10.1175/WAF-D-19-0014.1.

Ashley, W. S., A. J. Krmenec, and R. Schwantes, 2008: Vulnerability due to nocturnal tornadoes. *Wea. Forecasting*, **23**, 795–807.

Atkins, N. T., J. M. Arnott, R. W. Przybylinski, R. A. Wolf, and B. D. Ketcham, 2004: Vortex structure and evolution within bow echoes. Part I: Single-doppler and damage analysis of the 29 june 1998 derecho. *Mon. Wea. Rev.*, **132**, 2224–2242, doi:10.1175/1520-0493(2004)132⟨2224:VSAEWB⟩2.0.CO;2.

Atkins, N. T., C. S. Bouchard, R. W. Przybylinski, R. J. Trapp, and G. Schmocker, 2005: Damaging surface wind mechanisms within the 10 June 2003 Saint Louis bow echo during BAMEX. *Mon. Wea. Rev.*, **133**, 2275–2296, doi:10.1175/MWR2973.1.

Atkins, N. T., and M. S. Laurent, 2009a: Bow echo mesovortices. Part I: Processes that influence their damaging potential. *Mon. Wea. Rev.*, **137**, 1497–1513, doi:10.1175/2008MWR2649.1.

Atkins, N. T., and M. S. Laurent, 2009b: Bow echo mesovortices. Part II: Their genesis. *Mon. Wea. Rev.*, **137**, 1514–1532, doi:10.1175/2008MWR2650.1.

Atkins, N. T., and M. S. Laurent, 2009b: Bow echo mesovortices. part ii: Their genesis. *Mon. Wea. Rev.*, **137**, 1514–1532, doi:10.1175/2008MWR2650.1.

Aurenhammer, F., 1991: Voronoi diagrams—a survey of a fundamental geometric data structure. *ACM Comput. Surv.*, **23**, 345–405, doi:10.1145/116873.116880.

Biggerstaff, M. I., and R. A. Houze, 1991: Kinematic and precipitation structure of the 10–11 june 1985 squall line. *Mon. Wea. Rev.*, **119**, 3034–3065, doi:10.1175/1520-0493(1991)119⟨3034:KAPSOT⟩2.0.CO;2.

Biggerstaff, M. I., and R. A. Houze, 1993: Kinematics and microphysics of the transition zone of the 10–11 June 1985 squall line. *J. Atmos. Sci.*, **50**, 3091–3110, doi:10.1175/15200469(1993)050⟨3091:KAMOTT⟩2.0.CO;2.

Braun, S. A., and R. A. Houze, 1995: Melting and freezing in a mesoscale convective system. *Quart. J. Roy. Meteor. Soc.*, **121**, 55–77, doi:10.1002/qj.49712152104.

Britt, K. C., P. S. Skinner, P. L. Heinselman, and K. H. Knopfmeier, 2020: Effects of horizontal grid spacing and inflow environment on forecasts of cyclic mesocyclogenesis in NSSL's Warn-on-Forecast System (WoFS). *Wea. Forecasting*, **35**, 2423–2444, doi:10.1175/WAF-D-20-0094.1.

Britt, K. C., P. S. Skinner, P. L. Heinselman, C. K. Potvin, M. L. Flora, B. Matilla, K. H. Knopfmeier, and A. E. Reinhart, 2024: Verification of quasi-linear convective systems predicted by the Warn-on-Forecast System (WoFS). **39**, 155–176, doi:10.1175/WAF-D-23-0106.1.

Brooks, H. E., 2004: Torando-warning performance in the past and future: A perspective from signal detection theory. *Bull. Amer. Meteor. Soc.*, **85**, 837–844, doi:10.1175/BAMS-85-6-837.

Brooks, H. E., and J. Correia, 2018: Long-term performance metrics for national weather service tornado warnings. *Weather and Forecasting*, **33**, 1501–1511, doi:10.1175/WAF-D-18-0120.1.

Brotzge, J. A., S. E. Nelson, R. L. Thompson, and B. T. Smith, 2013: Tornado probability of detection and lead time as a function of convective mode and environmental parameters. *Wea. Forecasting*, **28**, 1261–1276, doi:10.1175/WAF-D-12-00119.1.

Brown, M. C., G. R. Marion, and M. C. Coniglio, 2024: Influence of low-level shear orientation and magnitude on the evolution and rotation of idealized squall lines. Part I: Storm morphology and bulk updraft/mesovortex attributes. *Mon. Wea. Rev.*, doi:10.1175/MWR-D-23-0262.1.

Bryan, G. H., and M. D. Parker, 2010: Observations of a squall line and its near environment using high-frequency rawinsonde launches during VORTEX2. *Mon. Wea. Rev.*, **138**, 4076–4097, doi:10.1175/2010MWR3359.1.

Chasteen, M. B., and S. E. Koch, 2022: Multiscale aspects of the 26–27 April 2011 tornado outbreak. Part I: Outbreak chronology and environmental evolution. *Mon. Wea. Rev.*, **150**, 309–335, doi:10.1175/MWR-D-21-0013.1.

Ciuricä, S., and Coauthors, 2019: Arterial tortuosity. *Hypertension*, **73**, 951–960, doi:10.1161/HYPERTENSIONAHA.118.11647, URL https://www.ahajournals.org/doi/abs/10.1161/HYPERTENSIONAHA.118.11647.

Clark, A. J., and Coauthors, 2020: A real-time simulated forecasting experiment for advancing the prediction of hazardous convective weather. *Bull. Amer. Meteor. Soc.*, **101**, E2022–E2024, doi:10.1175/BAMS-D-20-0268.1.

Clark, A. J., and Coauthors, 2021: A real-time, virtual spring forecasting experiment to advance severe weather prediction. *Bull. Amer. Meteor. Soc.*, **102**, E814–E816, doi:10.1175/BAMS-D-21-0239.1.

Coffer, B. E., M. D. Parker, J. M. L. Dahl, L. J. Wicker, and A. J. Clark, 2017: Volatility of tornadogenesis: An ensemble of simulated nontornadic and tornadic supercells in VORTEX2 environments. *Mon. Wea. Rev.*, **145**, 4605–4625, doi:10.1175/MWR-D-17-0152.1.

Coniglio, M. C., S. F. Corfidi, and J. S. Kain, 2012: Views on applying RKW theory: An illustration using the 8 May 2009 derecho-producing convective system. *Mon. Wea. Rev.*, **140**, 1023–1043, doi:10.1175/MWR-D-11-00026.1.

Coniglio, M. C., and D. J. Stensrud, 2001: Simulation of a progressive derecho using composite initial conditions. *Mon. Wea. Rev.*, **129**, 1593–1616, doi:10.1175/1520-0493(2001)129⟨1593:SOAPDU⟩2.0.CO;2.

Conrad, D. M., and K. R. Knupp, 2019: Doppler radar observations of horizontal shearing instability in quasi-linear convective systems. *Mon. Wea. Rev.*, **147**, 1297–1318, doi:10.1175/MWR-D-18-0257.1.

Davies-Jones, R., 2015: A review of supercell and tornado dynamics. *Atmospheric Research*, **158-159**, 274–291, doi:https://doi.org/10.1016/j.atmosres.2014.04.007.

Davis, C., B. Brown, and R. Bullock, 2006a: Object-based verification of precipitation forecasts. Part I: Methodology and application to mesoscale rain areas. *Mon. Wea. Rev.*, **134**, 1772–1784, doi:10.1175/MWR3145.1.

Davis, C., B. Brown, and R. Bullock, 2006b: Object-based verification of precipitation forecasts. Part II: Application to convective rain systems. *Mon. Wea. Rev.*, **134**, 1785–1795, doi:10.1175/MWR3146.1.

Des Moines, I. W. F. O., 2021: Severe storms and extreme winds - december 15, 2021. https://www.weather.gov/dmx/StormyandWindyWednesdayDecember152021 [Accessed: 24 June 2024].

Dowell, D., and Coauthors, 2016: Development of a high-resolution rapid refresh ensemble (HRRRE) for severe weather forecasting. *28th Conf. on Servere Local Storms*, Portland, OR, Amer. Meteor. Soc., 8B.2, URL https://ams.confex.com/ams/28SLS/webprogram/Paper301555.html.

Dowell, D. C., and Coauthors, 2022: The high-resolution rapid refresh (HRRR): An hourly updating convection-allowing forecast model. Part I: Motivation and system description. *Wea. Forecasting*, **37**, 1371–1395, doi:10.1175/WAF-D-21-0151.1.

Evans, J. S., and C. A. Doswell, 2001: Examination of derecho environments using proximity soundings. **16**, 329–342, doi:10.1175/1520-0434(2001)016⟨0329:EODEUP⟩2.0.CO;2.

Flora, M. L., P. S. Skinner, C. K. Potvin, A. E. Reinhart, T. A. Jones, N. Yussouf, and K. H. Knopfmeier, 2019: Object-based verification of short-term, storm-scale probabilistic mesocyclone guidance from an experimental warn-on-forecast system. *Wea. Forecasting*, **34**, 1721–1739, doi:10.1175/WAF-D-19-0094.1.

Flournoy, M. D., and M. C. Coniglio, 2019: Origins of vorticity in a simulated tornadic mesovortex observed during PECAN on 6 July 2015. *Mon. Wea. Rev.*, **147**, 107–134, doi:10.1175/MWR-D-18-0221.1.

Flournoy, M. D., M. C. Coniglio, E. N. Rasmussen, J. C. Furtado, and B. E. Coffer, 2020: Modes of storm-scale variability and tornado potential in VORTEX2 near- and far-field tornadic environments. *Mon. Wea. Rev.*, **148**, 4185–4207, doi:10.1175/MWR-D-20-0147.1.

Forbes, G. S., and R. M. Wakimoto, 1983: A concentrated outbreak of tornadoes, downbursts, and microbursts, and implications regarding vortex classification. *Mon. Wea. Rev.*, **111**, 220–236, doi:10.1175/1520-0493(1983)111⟨0220:ACOOTD⟩2.0.CO;2.

Fu, J., H. R. Thomas, and C. Li, 2021: Tortuosity of porous media: Image analysis and physical simulation. *Earth-Science Reviews*, **212**, 103 439, doi:10.1016/j.earscirev.2020.103439, URL https://www.sciencedirect.com/science/article/pii/S0012825220304852.

Fujita, T. T., 1981: Tornadoes and downbursts in the context of generalized platetary scales. *J. Atmos. Sci.*, **38**, 1511–1534, doi:10.1175/1520-0469(1981)038⟨1511:TADITC⟩2.0.CO;2.

Fujita, T. T., and R. M. Wakimoto, 1981: Five scales of airflow associated with a series of downbursts on 16 July 1980. *Mon. Wea. Rev.*, **109**, 1438–1456, doi:10.1175/1520-0493(1981)109⟨1438:FSOAAW⟩2.0.CO;2.

Funk, T. W., K. E. Darmofal, J. D. Kirkpatrick, V. DeWald, R. W. Przybylinski, G. K. Schmocker, and Y. J. Lin, 1999: Storm reflectivity and mesocyclone evoluation associated with the 15 april 1994 squall line over Kentucky and southern Indiana. **14**, 976–993, doi:10.1175/1520-0434(1990)014⟨0976:SRAMEA⟩2.0.C0;2.

Galarneau, T. J., P. S. Skinner, M. L. Flora, and K. C. Britt, 2023: Potential vorticity diagnosis of mesoscale convective systems in the Warn-on-Forecast System. *28th Conference on Numerical Weather Prediction*, Madison, WI, Amer. Meteor. Soc., Presentation 5.5, URL https://ams.confex.com/ams/WAFNWPMS/meetingapp.cgi/Paper/425560.

Gibbs, J. G., 2021: Evaluating precursor signals for qlcs tornado and higher impact straight-line wind events. *J. Operational Meteor.*, **9**, 62–75, doi:10.15191/nwajom.2021.0905.

Gillies, S., C. van der Wel, J. V. den Bossche, M. W. Taves, J. Arnott, B. C. Ward, and Coauthors, 2023: Shapely: manipulation and analysis of geometric objects in the cartesian plane. doi:10.5281/zenodo.5597138, URL https://github.com/shapely/shapely.

Grim, J. A., R. M. Rauber, G. M. McFarquhar, B. F. Jewett, and D. P. Jorgensen, 2009: Development and forcing of the rear inflow jet in a rapidly developing and decaying squall line during BAMEX. *Mon. Wea. Rev.*, **137**, 1206–1229, doi:10.1175/2008MWR2503.1.

Guerra, J. E., P. S. Skinner, A. Clark, M. Flora, B. Matilla, K. Knopfmeier, and A. E. Reinhart, 2022: Quantification of NSSL Warn-on-Forecast System accuracy by storm age using object-based verification. *Wea. Forecasting*, **37**, 1973–1983, doi:10.1175/WAF-D-22-0043.1.

Heinselman, P. L., and Coauthors, 2024: Warn-on-Forecast: From vision to reality. **39**, 75–95, doi:10.1175/WAF-D-23-0147.1.

Houston, A. L., C. C. Weiss, E. Rasmussen, M. C. Coniglio, C. L. Ziegler, B. Argrow, and E. W. Frew, 2022: Targeted observation by radars and UAS of supercells (TORUS): Summary of the 2019 and 2022 field campaigns. *30th Conference on Severe Local Storms*, Santa Fe, NM, Amer. Meteor. Soc., 7.1B, URL https://ams.confex.com/ams/30SLS/meetingapp.cgi/Paper/407665.

Houtekamer, P. L., and F. Zhang, 2016: Review of the ensemble kalman filter for atmospheric data assimilation. *Mon. Wea. Rev.*, **144**, 4489–4532, doi:10.1175/MWR-D-15-0440.1.

Houze, R. A., 2018: 100 years of research on mesoscale convective systems. *Meteorological Monographs*, **59**, 17.1–17.54, doi:10.1175/AMSMONOGRAPHS-D-18-0001.1.

Hu, M., H. Shao, D. Stark, K. Newman, C. Zhou, and X. Zhang, 2016: Gridpoint Statistical Interpolation GSI user's guide version 3.5. *Developmental Testbed Center Rep.*, 141 pp, URL https://dtcenter.org/com-GSI/users/docs/users_guide/GSIUserGuide_v3.5.pdf.

Johns, R. H., and W. D. Hirt, 1987: Derechos: Widespread convectively induced windstorms. **2**, 32–49, doi:10.1175/1520-0434(1987)002⟨0032:DWCIW⟩2.0.C0;2.

Jones, T., P. Skinner, N. Yussouf, K. Knopfmeier, A. Reinhart, and D. Dowell, 2019: Forecasting high-impact weather in landfalling tropical cyclones using a warn-on-forecast system. *Bull. Amer. Meteor. Soc.*, **100**, doi:10.1175/BAMS-D-18-0203.1.

Jones, T. A., K. Knopfmeier, D. Wheatley, G. Creager, P. Minnis, and R. Palikonda, 2016: Storm-scale data assimilation and ensemble forecasting with the NSSL Experimental Warn-on-Forecast system. Part II: Combined radar and satellite data experiments. *Wea. Forecasting*, **31**, 297–327, doi:10.1175/WAF-D-15-0107.1.

Jones, T. A., D. Stensrud, L. Wicker, P. Minnis, and R. Palikonda, 2015: Simultaneous radar and satellite data storm-scale assimilation using an ensemble kalman filter approach for 24 May 2011. *Mon. Wea. Rev.*, **143**, 165–194, doi:10.1175/MWR-D-14-00180.1.

Jones, T. A., X. Wang, P. Skinner, A. Johnson, and Y. Wang, 2018: Assimilation of GOES-13 imager clear-sky water vapor (6.5 μm) radiances into a warn-on-forecast system. *Mon. Wea. Rev.*, **146**, 1077–1107, doi:10.1175/MWR-D-17-0280.1.

Jones, T. A., and Coauthors, 2020: Assimilation of GOES-16 radiances and retrievals into the Warn-on-Forecast system. *Mon. Wea. Rev.*, **148**, 1829–1859, doi:10.1175/MWR-D-19-0379.1.

Kerr, C. A., and F. Alsheimer, 2022: Storm-scale predictability and analysis of the 13 April 2020 central Savannah River area tornado outbreak. *Wea. Forecasting*, **37**, 901–913, doi:10.1175/WAF-D-21-0185.1.

King, J. R., M. D. Parker, K. D. Sherburn, and G. M. Lackmann, 2017: Rapid evolution of cool season, low-CAPE severe thunderstorm environments. **32**, 763–779, doi:10.1175/WAF-D-16-0141.1.

Kleist, D. T., D. F. Parrish, J. C. Derber, R. Treadon, W.-S. Wu, and S. Lord, 2009: Introduction of the gsi into the ncep global data assimilation system. *Wea. Forecasting*, **24**, 1691–1705, doi:10.1175/2009WAF2222201.1.

Kosiba, K. A., and Coauthors, 2024: The propagation, evolution, and rotation of linear storms (PERiLS) project. *Bull. Amer. Meteor. Soc.*, doi:10.1175/BAMS-D-22-0064.1, in press.

Kosiba, K. A., J. Wurman, R. J. Trapp, M. D. Parker, and S. W. Nesbitt, 2022: The PERiLS (propagation, evolution and rotation in linear storms) southeastern tornado study. *30th Conference on Severe Local Storms*, Santa Fe, NM, Amer. Meteor. Soc., Poster 153, URL https://ams.confex.com/ams/30SLS/meetingapp.cgi/Paper/407690.

Krocak, M. J., M. D. Flournoy, and H. E. Brooks, 2021: Examining subdaily tornado warning performance and associated environmental characteristics. *Weather and Forecasting*, **36**, 1779–1784, doi:10.1175/WAF-D-21-0097.1.

Laser, J. J., M. C. Coniglio, P. S. Skinner, and E. N. Smith, 2022: Doppler lidar and mobile radiosonde observation-based evaluation of Warn-on-Forecast System predicted near-supercell environments during TORUS 2019. *Wea. Forecasting*, **37**, 1783–1804, doi:10.1175/WAF-D-21-0190.1.

Lawson, J. R., J. S. Kain, N. Yussouf, D. C. Dowell, D. M. Wheatley, K. H. Knopfmeier, and T. A. Jones, 2018: Advancing from convection-allowing nwp to warn-on-forecast: Evidence of progress. *Wea. Forecasting*, **33**, 599–607, doi:10.1175/WAF-D-17-0145.1.

Lee, B. D., and R. B. Wilhelmson, 1997a: The numerical simulation of non-supercell tornadogenesis. part i: Initiation and evolution of pretornadic misocyclone circulations along a dry outflow boundary. *J. Atmos. Sci.*, **54**, 32–60.

Lee, B. D., and R. B. Wilhelmson, 1997b: The numerical simulation of non-supercell tornadogenesis. part ii: Evolution of a family of tornadoes along a weak outflow boundary. *J. Atmos. Sci.*, **54**, 2387–2415.

Lovell, L. T., and M. D. Parker, 2022: Simulated QLCS vortices in a high-shear, low-CAPE environment. **37**, 989–1012, doi:10.1175/WAF-D-21-0133.1.

Lyza, A. W., A. W. Clayton, K. R. Knupp, E. Lenning, M. T. Friedlein, R. L. Castro, and E. S. Bentley, 2017: Analysis of mesovortex characteristics, behavior, and interactions during the second 30 June–1 July 2014 Midwestern derecho event. *EJSSM*, **12**, 1–33, doi:10.1175/1520-0434(1990)014⟨0976:SRAMEA⟩2.0.C0;2.

Mahale, V. N., J. A. Brotzge, and H. B. Bluestein, 2012: An analysis of vortices embedded within a quasi-linear convective system using x-band polarimetric radar. *Wea. Forecasting*, **27**, 1520–1537, doi:10.1175/WAF-D-11-00135.1.

Mansell, E. R., C. L. Ziegler, and E. C. Bruning, 2010: Simulated electrification of a small thunderstorm with two-moment bulk microphysics. *J. Atmos. Sci.*, **67**, 171–194, doi:10.1175/2009JAS2965.1.

Marion, G. R., and R. J. Trapp, 2021: Controls of quasi-linear convective system tornado intensity. *J. Atmos. Sci.*, **78**, 1189–1205, doi:10.1175/JAS-D-20-0164.1.

Markowski, P. M., and Y. Richardson, 2010: *Mesoscale Meteorology in Midlatitudes.* Wiley-Blackwell, 432 pp.

Markowski, P. M., and Y. P. Richardson, 2009: Tornadogenesis: Our current understanding, forecasting considerations, and questions to guide future research. *Atmos. Res.*, **93**, 3–10, doi:10.1016/j.atmosres.2008.09.015.

McDonald, J. M., and C. C. Weiss, 2021: Cold pool characteristics of tornadic quasi-linear convective systems and other convective modes observed during VORTEX-SE. *Mon. Wea. Rev.*, **149**, 821–840, doi:10.1175/MWR-D-20-0226.1.

Meng, Z., F. Zhang, P. Markowski, D. Wu, and K. Zhao, 2012: A modeling study on the development of a bowing structure and associated rear inflow within a squall line over south China. *J. Atmos. Sci.*, **69**, 1182–1207, doi:10.1175/JAS-D-11-0121.1.

Miller, W. J. S., and Coauthors, 2022: Exploring the usefulness of downscaling free forecasts from the warn-on-forecast system. *Wea. Forecasting*, **37**, 181–203, doi:10.1175/WAF-D-21-0079.1.

NCEI, 2021: December 2021 national climate report. https://www.ncei.noaa.gov/access/monitoring/monthly-report/national/202112 [Accessed: 24 June 2024].

Newman, J. F., and P. L. Heinselman, 2012: Evolution of a quasi-linear convective system sampled by phased array radar. *Mon. Wea. Rev.*, **140**, 3467–3486, doi:10.1175/MWR-D-12-00003.1.

NOAA, 2024: Damage assessment toolkit. https://apps.dat.noaa.gov/stormdamage/damageviewer/ [Accessed: 20 June 2024].

Parker, M. D., 2014: Composite vortex2 supercell environments from near-storm soundings. *Mon. Wea. Rev.*, **142**, 508–529, doi:10.1175/MWR-D-13-00167.1.

Parker, M. D., B. S. Borchardt, R. L. Miller, and C. L. Ziegler, 2020: Simulated evolution and severe wind production by the 25–26 June 2015 nocturnal MCS from PECAN. *Mon. Wea. Rev.*, **148**, 183–209, doi:10.1175/MWR-D-19-0072.1.

Parker, M. D., and R. H. Johnson, 2000: Organizational modes of midlatitude mesoscale convective systems. *Mon. Wea. Rev.*, **128**, 3413–3436, doi:10.1175/1520-0493(2001)129,3413:OMOMMC.2.0.CO;2.

Potvin, C. K., and Coauthors, 2020: Assessing systematic impacts of PBL schemes on storm evolution in the NOAA warn-on-forecast system. *Mon. Wea. Rev.*, **148**, 2567–2590, doi:10.1175/MWR-D-19-0389.1.

Potvin, C. K., and Coauthors, 2022: An iterative storm segmentation and classification algorithm for convection-allowing models and gridded radar analyses. *J. Atmos. Oceanic Technol.*, **39**, 999–1013, doi:10.1175/JTECH-D-21-0141.1.

Przybylinski, R. W., 1995: The bow echo: Observations, numerical simulations, and severe weather detection methods. **10**, 203–218, doi:10.1175/1520-0434(1995)010⟨0203:TBEONS⟩2.0.CO;2.

Roberts, B., I. L. Jirak, A. J. Clark, S. J. Weiss, and J. S. Kain, 2019: Postprocessing and visualization techniques for convection-allowing ensembles. *Bull. Amer. Meteor. Soc.*, **100**, 1245–1258, doi:10.1175/BAMS-D-18-0041.1.

Rotunno, R., J. B. Klemp, and M. L. Weisman, 1988: A theory for strong, long-lived squall lines. *J. Atmos. Sci.*, **45**, 463–485, doi:10.1175/1520-0469(1988)045⟨0463:ATFSLL⟩2.0.CO;2.

Schaumann, J. S., and R. W. Przybylinksi, 2012: Operational application of 0–3-km bulk shear vectors in assessing qlcs mesovortex and tornado potential. *26th Conf on Severe Local Storms*, Nashville, TN, Amer. Meteor. Soc., P.9.10, URL https://ams.confex.com/ams/26SLS/webprogram/Paper212008.html.

Schenkman, A. D., M. Xue, and A. Shapiro, 2012: Tornadogenesis in a simulated mesovortex within a mesoscale convective system. *J. Atmos. Sci.*, **69**, 3372–3390, doi:10.1175/JAS-D-12-038.1.

Schwartz, C. S., and R. A. Sobash, 2017: Generating probabilistic forecasts from convection-allowing ensembles using neighborhood approaches: A review and recommendations. *Mon. Wea. Rev.*, **145**, 3397–3418, doi:10.1175/MWR-D-16-0400.1.

Sherburn, K. D., and M. D. Parker, 2014: Climatology and ingredients of significant severe convection in high-shear, low-CAPE environments. **29**, 854–877, doi:10.1175/WAF-D-13-00041.1.

Sherburn, K. D., M. D. Parker, J. R. King, and G. M. Lackmann, 2016: Composite environments of severe and nonsevere high-shear, low-CAPE convective events. **31**, 1899–1927, doi:10.1175/WAF-D-16-0086.1.

Skinner, P. S., and Coauthors, 2018: Object-based verification of a prototype Warn-on-Forecast system. *Wea. Forecasting*, **33**, doi:10.1175/WAF-D-18-0020.1.

Skinner, P. S., and Coauthors, 2023: Interpreting Warn-on-Forecast System guidance, Part I: review of probabilistic guidance concepts, product design, and best practices. **11**, 110–131, doi:10.15191/nwajom.2023.1109.

Smirnova, T. G., J. M. Brown, S. G. Benjamin, and J. S. Kenyon, 2016: Modifications to the rapid update cycle land surface model (ruc lsm) available in the weather research and forecasting (WRF) model. *Mon. Wea. Rev.*, **144**, 1851–1865, doi:10.1175/MWR-D-15-0198.1.

Smith, B. T., R. L. Thompson, J. S. Grams, C. Broyles, and H. E. Brooks, 2012: Convective modes for significant severe thunderstorms in the Contiguous United States. Part I: Storm classification and climatology. *Wea. Forecasting*, **27**, 1114–1135, doi:10.1175/WAF-D-11-00115.1.

Smith, T. M., and Coauthors, 2016: Multi-radar multi-sensor (MRMS) severe weather and aviation products: Initial operating capabilities. *Bull. Amer. Meteor. Soc.*, **97**, 1617–1630, doi:10.1175/BAMS-D-14-00173.1.

Smull, B. F., and R. A. Houze, 1987a: Rear inflow in squall lines with trailing stratiform precipitation. *Mon. Wea. Rev.*, **115**, 2869–2889, doi:10.1175/1520-0493(1987)115⟨2869:RIISLW⟩2.0.CO;2.

Smull, B. F., and R. A. Houze, 1987b: Rear inflow in squall lines with trailing stratiform precipitation. *Mon. Wea. Rev.*, **115**, 2869–2889, doi:10.1175/1520-0493(1987)115⟨2869:RIISLW⟩2.0.CO;2.

SPC, 2023: Severe weather database. https://www.spc.noaa.gov/wcm/#data [Accessed: 20 June 2024].

Squitieri, B. J., A. R. Wade, and I. L. Jirak, 2023a: A historical overview on the science of derechos: Part I: identification, climatology, and societal impacts. *Bull. Amer. Meteor. Soc.*, **104**, E1709–E1733, doi:10.1175/BAMS-D-22-0217.1.

Squitieri, B. J., A. R. Wade, and I. L. Jirak, 2023b: A historical overview on the science of derechos: Part II: Parent storm structure, environmental conditions, and history of numerical forecasts. *Bull. Amer. Meteor. Soc.*, **104**, E1734–E1763, doi:10.1175/BAMS-D-22-0278.1.

Stensrud, D. J., and Coauthors, 2009: Convective-scale Warn-on-Forecast System: A Vision for 2020. *Bull. Amer. Meteor. Soc.*, **90**, 1487–1500, doi:10.1175/2009BAMS2795.1.

Stensrud, D. J., and Coauthors, 2013: Progress and challenges with Warn-on-Forecast. *Atmos. Res.*, **123**, 2–16, doi:10.1016/j.atmosres.2012.04.004.

Thompson, R. L., R. Edwards, J. A. Hart, K. L. Elmore, and P. Markowski, 2003: Close proximity soundings within supercell environments obtained from the rapid update cycle. *Wea. Forecasting*, **18**, 1243–1261.

Thompson, R. L., C. M. Mead, and R. Edwards, 2007: Effective storm-relative helicity and bulk shear in supercell thunderstorm environments. *Wea. Forecasting*, **22**, 102–115, doi:10.1175/WAF969.1.

Thompson, R. L., B. T. Smith, J. S. Grams, A. R. Dean, and C. Broyles, 2012: Convective modes for significant severe thunderstorms in the Contiguous United States. Part II: Supercell and QLCS tornado environments. *Wea. Forecasting*, **27**, 1136–1154, doi:10.1175/WAF-D-11-00116.1.

Tochimoto, E., and H. Niino, 2022: Tornadogenesis in a quasi-linear convective system over Kanto Plain in Japan: A numerical case study. *Mon. Wea. Rev.*, **150**, 259–282, doi:10.1175/MWR-D-20-0402.1.

Trapp, R. J., S. A. Tessendorf, E. S. Godfrey, and H. E. Brooks, 2005: Tornadoes from squall lines and bow echoes. Part I: Climatological distribution. *Wea. Forecasting*, **20**, 23–34, doi:10.1175/WAF-835.1.

Trapp, R. J., and M. L. Weisman, 2003: Low-level mesovortices within squall lines and bow echoes. Part II: Their genesis and implications. *Mon. Wea. Rev.*, **131**, 2804–2823, doi:10.1175/1520-0493(2003)131⟨2804:LMWSLA⟩2.0.CO;2.

Ungar, J., 2022: Label centerlines. URL https://github.com/ungarj/label_centerlines.

Ungar, M. D., and M. C. Coniglio, 2023: Using radiosonde observations to assess the "Three Ingredients Method" to forecast QLCS mesovortices. **38**, 2441–2460, doi:10.1175/WAF-D-22-0176.1.

Van der Walt, S., J. L. Schonberger, J. Nunez-Iglesias, F. Boulogne, J. D. Warner, N. Yager, E. Gouillart, and T. Yu, 2014: Scikit-image: Image processesing in python. *PeerJ*, **2**, e453, doi:10.7717/peerj.453.

Wakimoto, R. M., H. V. Murphey, C. A. Davis, and N. T. Atkins, 2006: High winds generated by bow echoes. Part II: The relationship between the mesovortices and damaging straight-line winds. *Mon. Wea. Rev.*, **134**, 2813–2829, doi:10.1175/MWR3216.1.

Weisman, M. L., 1992: The role of convectively generated rear-inflow jets in the evolution of long-lived mesoconvective systems. *J. Atmos. Sci.*, **49**, 1826–1847, doi:10.1175/1520-0469(1992)049⟨1826:TROCGR⟩2.0.CO;2.

Weisman, M. L., 1993: The genesis of severe, long-lived bow echoes. *J. Atmos. Sci.*, **50**, 645–670, doi:10.1175/1520-0469(1993)050⟨0645:TGOSLL⟩2.0.CO;2.

Weisman, M. L., 2001: Bow echoes: A tribute to t. t. fujita. *Bull. Amer. Meteor. Soc.*, **82**, 97–116, doi:10.1175/1520-0477(2001)082⟨0097:BEATTT⟩2.3.CO;2.

Weisman, M. L., and C. A. Davis, 1998: Mechanisms for the generation of mesoscale vortices within quasi-linear convective systems. *J. Atmos. Sci.*, **55**, 2603–2622, doi:10.1175/1520-0469(1998)055⟨2603:MFTGOM⟩2.0.CO;2.

Weisman, M. L., and R. Rotunno, 2004: "a theory for strong long-lived squall lines" revisited. *J. Atmos. Sci.*, **61**, 361–382, doi:10.1175/1520-0469(2004)061⟨0361:ATFSLS⟩2.0.CO;2.

Weisman, M. L., and R. J. Trapp, 2003a: Low-level meso-vortices within squall lines and bow echoes. Part I: Overview and dependence on environmental shear. *Mon. Wea. Rev.*, **131**, 2779–2803.

Weisman, M. L., and R. J. Trapp, 2003b: Low-level mesovortices within squall lines and bow echoes. Part I: Overview and dependence on environmental shear. *Mon. Wea. Rev.*, **131**, 2779–2803, doi:10.1175/1520-0493(2003)131⟨2779:LMWSLA⟩2.0.CO;2.

Weyn, J. A., and D. R. Durran, 2017: The dependence of the predictability of mesoscale convective systems on the horizontal scale and amplitude of initial errors in idealized simulations. *J. Atmos. Sci.*, **74**, 2191–2210, doi:https://doi.org/10.1175/JAS-D-17-0006.1.

Weyn, J. A., and D. R. Durran, 2019: The scale dependence of initial-condition sensitivities in simulations of convective systems over the southeastern United States. *Quart. J. Roy. Meteor. Soc.*, **145**, 57–74, doi:10.1002/qj.3367.

Wheatley, D. M., K. H. Knopfmeier, T. A. Jones, and G. J. Creager, 2015: Storm-scale data assimilation and ensemble forecasting with the NSSL Experimental Warn-on-Forecast System. Part I: Radar data experiments. *Wea. Forecasting*, **30**, 1795–1817, doi:10.1175/WAF-D-15-0043.1.

Wheatley, D. M., and R. J. Trapp, 2008: The effect of mesoscale heterogeneity on the genesis and structure of mesovortices within quasi-linear convective systems. *Mon. Wea. Rev.*, **136**, 4220–4241, doi:10.1175/2008MWR2294.1.

Wheatley, D. M., R. J. Trapp, and N. T. Atkins, 2006: Radar and damage analysis of severe bow echoes observed during BAMEX. *Mon. Wea. Rev.*, **134**, 791–806, doi:10.1175/MWR3100.1.

Xu, X., M. Xue, and Y. Wang, 2015: The genesis of mesovortices within a real-data simulation of a bow echo system. *J. Atmos. Sci.*, **72**, 1963–1986, doi:10.1175/JAS-D-14-0209.1.

Yussouf, N., D. C. Dowell, L. J. Wicker, K. H. Knopfmeier, and D. M. Wheatley, 2015: Storm-scale data assimilation and ensemble forecasts for the 27 April 2011 severe weather outbreak in Alabama. *Mon. Wea. Rev.*, **143**, 3044–3066, doi:10.1175/MWR-D-14-00268.1.

Yussouf, N., T. A. Jones, and P. S. Skinner, 2020a: Probabilistic high-impact rainfall forecasts from landfalling tropical cyclones using warn-on-forecast system. *Quart. J. Roy. Meteor. Soc.*, **146**, 2050–2065, doi:10.1002/qj.3779.

Yussouf, N., J. S. Kain, and A. J. Clark, 2016: Short-term probabilistic forecasts of the 31 may 2013 oklahoma tornado and flash flood event using a continuous-update-cycle storm-scale ensemble system. *Wea. Forecasting*, **31**, 957–983, doi:10.1175/WAF-D-15-0160.1.

Yussouf, N., and K. H. Knopfmeier, 2019: Application of the warn-on-forecast system for flash-flood-producing heavy convective rainfall events. *Quart. J. Roy. Meteor. Soc.*, **145**, 2385–2403, doi:10.1002/qj.3568.

Yussouf, N., E. R. Mansell, L. J. Wicker, D. M. Wheatley, and D. J. Stensrud, 2013: The Ensemble Kalman Filter analyses and forecasts of the 8 May 2003 Oklahoma City tornadic supercell storm using single- and double-moment microphysics scheme. *Mon. Wea. Rev.*, **141**, 3388–3412, doi:10.1175/MWR-D-12-00237.1.

Yussouf, N., K. A. Wilson, S. M. Martinaitis, H. Vergara, P. L. Heinselman, and J. J. Gourley, 2020b: The coupling of nssl warn-on-forecast and FLASH systems for probabilistic flash flood prediction. *J. Hydrometeor.*, **21**, 123–141, doi:10.1175/JHM-D-19-0131.1.

Zhou, X., and Coauthors, 2022: The development of the NCEP global ensemble forecast system version 12. **37**, 1069–1084.